Polarization Measurement and Manipulation for Electric Dipole Moment Measurements in Storage Rings

Von der Fakultät für Mathematik, Informatik und Naturwissenschaften der RWTH Aachen University zur Erlangung des akademischen Grades eines Doktors der Naturwissenschaften genehmigte Dissertation

vorgelegt von
Nils Hempelmann, M.Sc. Physik
aus Bielefeld

Berichter: Univ.-Prof. Dr. rer. nat. Jörg Pretz
Dr. rer. nat. Ralf Gebel
Univ.-Prof. Dr. rer. nat. Achim Stahl

Tag der mündliche Prüfung: 14.02.2018

Diese Dissertation ist auf den Internetseiten der Universitätsbibliothek online verfügbar.

Electric dipole moments (EDM) in elementary particles violate CP-symmetry. A discovery of EDMs above the extremely small Standard Model predictions would indicate new physics, possibly related to the unexplained dominance of matter over antimatter in the universe. Most research on EDMs has focused on neutral particles such as neutrons or atoms. The EDM of charged particles, like protons or deuterons, could be measured in storage rings using the precession of the spin vector in the electric field in the rest frame of the particles.

Storage ring EDM measurements are one of the main research goals for the Cooler Synchrotron (COSY) at Forschungszentrum Jülich. This thesis makes two contributions to this goal: the complete replacement of the read-out electronics of the Low Energy Polarimeter at COSY and the analysis of data taken using the new spin feedback system.

The Low Energy Polarimeter (LEP) is a polarimeter in the injection beam line of COSY. The polarization is measured at an injection energy of 75 MeV for deuterons and 45 MeV for protons using elastic scattering off a carbon target. Outgoing particles are measured using twelve plastic scintillator detectors mounted in groups of three above, below, left and right of the target.

The old, analog electronics was replaced with a new system based on field programmable gate arrays (FPGA). The new system can measure amplitude and time of flight spectra as well as the pulse shape of the detector signals. All data is saved for offline analysis, which was not previously possible. The rate of spectrum measurements could be improved from about 10 kHz for the old electronics to values from 30 kHz to over 150 kHz, depending on the scattering angle.

The spin feedback system is able to adjust the rapid ($\approx$ 121 kHz) in-plane spin precession to the frequency of a radio frequency (rf) solenoid. The feedback system uses a bunched polarized beam. The revolution frequency is adjusted constantly to keep a fixed phase between the horizontal polarization and the external rf signal.

The feedback system was tested using direct measurements of the relative phase. Additionally, the polarization was rotated out of the horizontal plane using the rf solenoid while the feedback was running. The effect of the solenoid shows a sinusoidal dependency on the relative phase set by the feedback, further proving that the system works. The feedback system meets the requirements for use in an EDM experiment.

Driven oscillations of the polarization induced by the rf solenoid were also examined, using the feedback system to set the initial conditions. The observed oscillations in the vertical and horizontal polarizations could be described using an analytical model.

Elektrische Dipolmomente (EDM) bei Elementarteilchen verletzen die CP-Symmetrie. Eine Entdeckung von EDMs oberhalb der extrem kleinen Standarmodellvorhersage wäre ein Zeichen für neue Physik, die möglicherweise mit der noch nicht erklärten Dominanz der Materie über Antimaterie im Universum zusammenhängt. Die meiste Forschung über EDMs konzentriert sich auf neutrale Teilchen, wie Neutronen oder Atome. Das EDM geladener Teilchen, wie Protonen oder Deuteronen, könnte in einem Speicherring gemessen werden. Dazu wird die Präzession des Spinvektors im elektrischen Feld im Ruhesystem der Teilchen betrachtet.

EDM-Messungen in Speicherringen sind einer der Forschungsschwerpunkte des Cooler Synchrotron (COSY) am Forschungszentrum Jülich. In dieser Arbeit werden zwei Beiträge dazu behandelt: die vollständige Ersetzung der Ausleseelektronik des Niederenergiepolarimeters bei COSY und die Analyse von Daten, die mit dem neuen Spinfeedbacksystem aufgenommen wurden.

Das Niederenergiepolarimeter (Low Energy Polarimeter, LEP) is ein Polarimeter in der Injektionsbeamline von COSY. Die Polarisation wird mittels elastischer Streuung an einem Kohlenstofftarget bei einer Energie von 75 MeV bei Deuteronen bzw. 45 MeV bei Protonen gemessen. Die auslaufenden Teilchen werden mit zwölf Plastikszintillatoren nachgewiesen, die in Dreiergruppen oberhalb, unterhalb, links und rechts vom Target angebracht sind.

Die alte, analoge Elektronik wurde durch ein neues System auf Grundlage von FPGAs ersetzt. Das neue System kann die Amplitude, die Flugzeit sowie die Pulsform der Detektorsignale messen. Alle Daten werden für Offlineanalysen gespeichert, was vorher nicht möglich war. Die Rate bei Spektrummessungen konnte, abhängig vom Struewinkel, von etwa 10 kHz bei der alten Elektronik auf Werte von 30 kHz bis über 150 kHz verbessert werden.

Das Spinfeedbacksystem kann die schnelle ($\approx$ 121 kHz) Präzession der horizontalen Polarisation an ein externes rf Signal anpassen. Es wird ein gebunchter Strahl verwendet. Die Umlauffrequenz wird laufend angepasst, um den Phasenunterschied zwischen der horizontal Polarisation und dem externen rf Signal konstant zu halten.

Das Feedbacksystem wurde durch direkte Messungen der relativen Phase getestet. Zusätzlich wurde die Polarisation mit einem rf Solenoiden aus der horizontalen Ebene herausgedreht, während das Feedbacksystem lief. Der Effekt des Solenoiden zeigt eine sinusförmige Abhängigkeit von der fürs Feedback eingestellten relativen Phase, was ein weiterer Beleg dafür ist, dass das System funktioniert. Das Feedbacksystem erfüllt die Anforderungen eines EDM-Experiments.

Zusätzlich wurden durch den Solenoiden erzeugte getriebene Oszillationen der Polarisation untersucht, bei denen das Feedbacksystem verwendet wurde, um die Anfangsbedingungen einzustellen. Die beobachteten Oszillationen der vertikalen und horizontalen Polarisation konnten mit einem analytischen Modell beschrieben werden.

Contents

1. Introduction

Fundamental symmetries play an essential role in particle physics. The Standard Model describes the fundamental interactions of matter using field theories which are invariant under gauge transformations. The strong interaction and the electromagnetic interaction are invariant under parity transformations, which change the sign of spatial vectors. In the weak interaction, parity is violated.

One particularly interesting symmetry is CP-symmetry, which is also conserved in the strong and electromagnetic interaction, but violated in weak processes. CP-violation is one of the preconditions for the observed dominance of matter over antimatter in the universe. The Standard Model of particle physics has only small CP-violating terms, which are insufficient by several orders of magnitude to explain the matter-antimatter asymmetry.

Electric dipole moments in fundamental particles violate CP-symmetry, making them an ideal probe for the search for new physics. Electric dipole moments (EDMs) also provide constraints for theories beyond the Standard Model, such as Supersymmetry. At this point, all existing EDM measurements are consistent with zero.

The search for EDMs has mostly focused on neutral systems like atoms and neutrons. For charged particles, such measurements are more complicated as the electric field, which is necessary to interact with the EDM, will accelerate the particle.

Storage rings provide a promising method to measure the EDM of charged hadrons such as protons and deuterons. In the rest frame of a particle in a storage ring, there is always a radial electric field that interacts with the EDM. Data from a storage ring experiment was used to find the most stringent limit for the muon EDM.

In practice, a precise control of the spin in the storage ring is necessary to obtain useful data. EDM measurements for deuterons at the Cooler Synchrotron (COSY) in Jülich would have systematic uncertainties in the order of $5 \cdot 10^{-21}\, e\,\mathrm{cm}$ to $5 \cdot 10^{-20}\, e\,\mathrm{cm}$, due to imperfections in the ring [1]. The goal for later experiments is a sensitivity in the order of $10^{-29}\, e\,\mathrm{cm}$ [2]. Despite this discrepancy, the experimental techniques needed for EDM measurements can be investigated and demonstrated at COSY.

Charged hadrons have magnetic dipole moments, which are much stronger than electric ones and lead to a rapid precession of the polarization in the ring plane. This can be dealt with by either using a dedicated EDM-ring, in which the polarization is kept parallel to the beam momentum using electrostatic elements or using a so-called Wien filter in a classical magnetic storage ring like COSY.

The two main topics of this thesis are the upgrade of the read-out electronics of the Low Energy Polarimeter (LEP) and the analysis of data taken during the commissioning of the spin feedback system at COSY. LEP, which is described in chapter 4, is the main tool for calibrating the polarized particle source at the beginning of each beam time with polarized particles and monitoring it during the experiments. The old analog read-out was replaced with a new system using field programmable gate arrays (FPGA). The new system can continuously monitor the energy spectra of the detectors at LEP and determine the time of each event with respect to the phase of the cyclotron voltage, which is linked to the time of flight.

The spin feedback system, which is described in chapter 5, can fix the phase of the rapid in-plane precession of spins in COSY with respect to an external rf signal. The phase of the spin precession is constantly measured and adjusted by changing the beam revolution frequency. This is a key requirement for planned precursor experiments for EDM measurements at COSY, for which the spin precession has to be in phase with an rf Wien filter in the ring. The analysis of the data shows that the feedback system works as expected. The feedback system was also used to investigate polarization rotations using a resonant rf solenoid by measuring the relative phase between the solenoid signal and the spin precession.

2. Theory

2.1. Electric Dipole Moments and Fundamental Symmetries

2.1.1. Fundamental Symmetries

A model is said to be symmetric under a transformation if it behaves the same way after the transformation. Symmetries are an essential feature in the Standard Model of particle physics, which describes the fundamental forces using gauge-invariant field theories.

Symmetries with respect to parity (P), charge conjugation (C) and time reversal (T) are particularly important. A parity transformation changes the sign of every spatial vector ($\boldsymbol{x} \rightarrow -\boldsymbol{x}$), acting like a mirror. Charge conjugation replaces all particles with their respective antiparticles and time reversal reverses time similar to parity ($t \rightarrow -t$). The eigenvalues of all three transformations are ± 1. An observable that changes its sign under a transformation is said to be odd under the transformation, an observable that remains unchanged is even.

It was long believed that all laws of physics are symmetric under parity. In 1956, parity violation in the weak interaction was discovered in the β-decay of ^{60}Co [3]. The weak interaction violates parity completely as all electrons in this decay were preferentially emitted in the direction of the spin of the decaying nucleus.

The weak interaction violates C-symmetry as well. The combination of both symmetries, CP-symmetry, is conserved in electromagnetic and strong processes and almost conserved in the weak interaction. CP-violation in the Standard Model is discussed in section 2.1.3.

The CPT theorem [4, CPT Invariance Tests in Neutral Kaon Decay] states that all laws of physics are symmetric under a combined charge, parity and time reversal transformation. No violations have been found empirically. The CPT theorem can be proven mathematically under very general conditions: Lorentz invariance, quantum field theory and locality. The conservation of CPT implies that all CP-violating processes also violate T and vice versa.

2.1.2. Matter-Antimatter-Asymmetry

The visible universe is dominated by matter rather than antimatter. The ratio of matter and antimatter created in the Big Bang can be estimated using the ratio of baryons to photons in the universe, as all antimatter has annihilated with matter forming photons.

Using data from the Planck satellite on the angular distribution of the cosmic microwave background, this ratio was determined to be [5]

$$\eta = \frac{n_B - n_{\bar{B}}}{n_\gamma} = (6.047 \pm 0.074.) \cdot 10^{-10}. \tag{2.1}$$

n_B is the number density of baryons, $n_{\bar{B}}$ is the number density of antibaryons, which is zero, and n_γ is the number density of photons in the cosmic microwave background.

This measurement indicates that the overwhelming part of matter in the early universe annihilated with antimatter forming the cosmic microwave background. The present dominance of matter is the result of this small asymmetry.

In 1967, Andrei Sakharov postulated three criteria for baryogenesis, the creation of baryons in the early universe [6]:

1. Baryon number violation
2. C and CP-violation
3. Thermal non-equilibrium

C and CP-violation are necessary for matter and antimatter to differ in ways other than a trivial reversal of spatial directions in all interactions.

Known sources of CP-violation (see section 2.1.4) are nine orders of magnitude too small to explain the observed abundance of matter in the universe [7]. New sources of CP-violation, which can be investigated using EDMs, are therefore needed.

2.1.3. CP-Violation in the Standard Model

CP-violation was first discovered in the decay of neutral kaons in 1964 [8]. This experiment observed the decay of neutral kaons into two pions in the process $K_l^0 \to \pi^+\pi^-$. The kaon has a CP eigenvalue of -1 while the pions have an eigenvalue of $+1$.

There are several different possible sources for CP-violation in the Standard Model: quark mixing, neutrino mixing and, with a small extension, the strong interaction [9]. All CP-violation that has been observed experimentally is due to the CKM (Cabibbo–Kobayashi–Maskawa) matrix V, which connects the mass and flavor eigenstates of quarks.

$$\begin{pmatrix} d' \\ s' \\ b' \end{pmatrix} = V \begin{pmatrix} d \\ s \\ b \end{pmatrix} \tag{2.2}$$

d', s' and b' are the eigenstates of the weak interaction and d, s and b are the mass eigenstates. The CKM matrix can be parametrized using three angles and a phase [10].

$$V = \begin{pmatrix} c_1 & -s_1 c_3 & -s_1 s_3 \\ s_1 c_2 & c_1 c_2 c_3 - s_2 s_3 e^{i\delta} & c_1 c_2 s_3 + s_2 c_3 e^{i\delta} \\ s_1 s_2 & c_1 s_2 c_3 + c_2 s_3 e^{i\delta} & c_1 s_2 s_3 - c_2 s_3 e^{i\delta} \end{pmatrix} \tag{2.3}$$

s_i and c_i are shorthands for the sine and cosine of the free parameters θ_i with $i \in \{1, 2, 3\}$. CP-violation can occur by interference between the different components in (2.3).

CP-violation could also be possible in the lepton sector, although it has not been observed [4, Neutrino Mass, Mixing, and Oscillations]. The PMNS (Pontecorvo–Maki–Nakagawa–Sak matrix describes the mixing between neutrino mass and flavor eigenstates in a similar way to (2.3). It also contains a CP-violating phase.

Finally, the Lagrangian for the strong interaction can be extended naturally to include CP-violation [9, 11].

$$\mathcal{L}_{s,\not{CP}} = -\theta \frac{g^2}{64\pi^2} \epsilon^{\mu\nu\alpha\beta} G^a_{\mu\nu} G^a_{\alpha\beta}, \tag{2.4}$$

where θ is a parameter that describes the magnitude of CP-violation, $G^a_{\mu\nu}$ is the strong field tensor and g is a coupling constant.

θ is constrained to less than 10^{-10} by measurements of the neutron EDM [11, 12]. As θ could, in principle, have any value, such small number seems unnatural. This problem, the strong CP problem, remains unresolved [9].

2.1.4. CP-Violation and Electric Dipole Moments

An EDM in an elementary particle violates CP-symmetry [13]. In classical physics, an EDM can be defined in terms of the electric charge density ρ.

$$\boldsymbol{d} = \int \rho(\boldsymbol{r}) d\boldsymbol{r} \tag{2.5}$$

This vector is even under time reversal and parity odd, because it is proportional to the spatial separation of charges. Magnetic dipole moments, which are known to exist in elementary particles, are even under parity transformation and odd under time reversal.

An EDM must be either parallel or antiparallel to the spin of the particle, which is the only distinguishable direction. Any other orientation would imply an additional degree of freedom in the orientation of the particle, which would make states possible that are normally forbidden by the Pauli principle. Applying a P or T transformation to the particle would change the relative orientation of the electric and magnetic dipole moment (fig. 2.1). The result would be a different kind of particle, which violates symmetry.

EDMs are possible in systems like molecules without violating CP by mixing multiple degenerate ground states of different parity. [13]

Table 2.1.: EDMs for different particles

Particle	EDM [$e \cdot \mathrm{cm}$]	Reference
e	$< 8.7 \cdot 10^{-29}$ (90% CL)	from ThO [4, 15]
μ	$(-0.1 \pm 0.9) \cdot 10^{-19}$	[4]
n	$< 3 \cdot 10^{-26}$ (90% CL)	[16]
p	$< 7.9 \cdot 10^{-25}$ (95% CL)	From ^{199}Hg [17, 2]

Table 2.1 shows an overview of EDMs measurements for different particles. All of the results are compatible with zero. The EDM of protons is an indirect result obtained

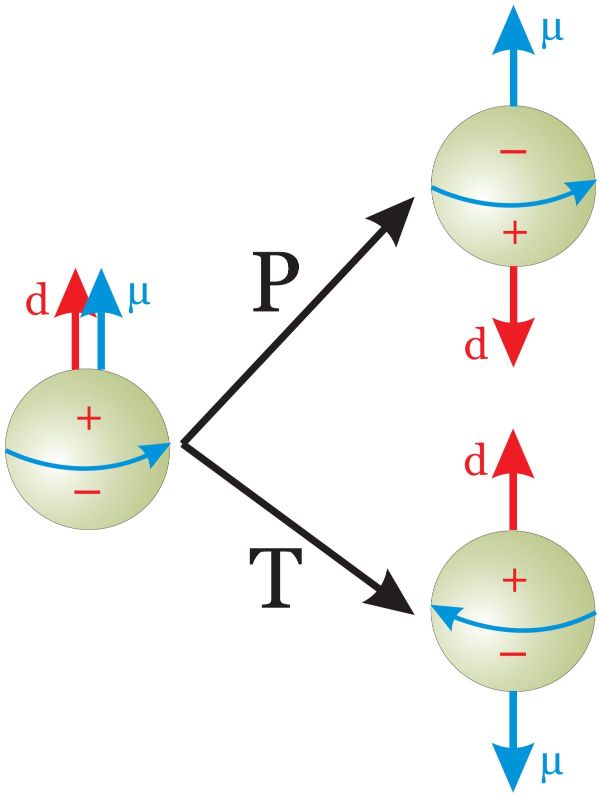

Figure 2.1.: Behavior of an EDM under P and T transformation [14, 13]

from a measurement of a mercury atom. There is no direct measurement of the EDM of charged hadrons yet, but a measurement for protons and deuterons could be taken using storage rings [2] (see also section 2.3).

The Standard Model predicts EDMs in the order of 10^{-32} to $10^{-31}\,e\,\mathrm{cm}$ for charged hadrons, which come from the CKM matrix [18]. These predictions are too small to be found in proposed storage ring experiments [2].

Various theories beyond the Standard Model, such as supersymmetry, predict substantially higher values [11, 19], which could exceed $10^{-29}\,e\,\mathrm{cm}$, the expected reach of storage ring experiments.

2.2. Polarized Particles and Nuclear Reactions

2.2.1. Spin and Polarization

The following section gives an overview of the mathematical description of spins and polarization. It is based on [20, chapter 1] and [21, chapter 5]. The experiments described in this thesis mainly deal with deuterons, which have a spin of 1. Spin $1/2$ particles such as protons are also considered for storage ring EDM measurements and will be discussed as well.

A single spin-$1/2$ particle can be described by a spinor ψ. The spin measurement corresponds to the operator

$$\boldsymbol{S} = \frac{\hbar}{2}\boldsymbol{\sigma}, \tag{2.6}$$

where $\boldsymbol{\sigma} = (\sigma_1, \sigma_2, \sigma_3)$ is the vector of the Pauli matrices

$$\sigma_1 = \begin{pmatrix} 0 & 1 \\ 1 & 0 \end{pmatrix}, \sigma_2 = \begin{pmatrix} 0 & -i \\ i & 0 \end{pmatrix}, \sigma_3 = \begin{pmatrix} 1 & 0 \\ 0 & -1 \end{pmatrix}. \tag{2.7}$$

The state of a system of multiple particles, such as a particle beam, can be described using the density operator

$$\rho = \sum_i p_i \left|\psi_i\right\rangle \left\langle\psi_i\right|, \tag{2.8}$$

for a state space spanned by a finite number of base vectors $|\psi_i\rangle$. The factors p_i describe the proportion of particles that are in the corresponding state $|\psi_i\rangle$. This is conceptually distinct from a pure quantum state that is a superposition of eigenstates such as $\frac{1}{\sqrt{2}}(|\psi_1\rangle + |\psi_2\rangle)$.

The beam polarization is defined as

$$\boldsymbol{P} = \langle\boldsymbol{\sigma}\rangle, \tag{2.9}$$

where $\langle\boldsymbol{\sigma}\rangle = \mathrm{Tr}(\rho\boldsymbol{\sigma})$ stands for the statistical average. In the special case of spin-$1/2$, the density matrix is given by the polarization as

$$\rho = \frac{1}{2}(1 + \boldsymbol{P}\cdot\boldsymbol{\sigma}). \tag{2.10}$$

Polarization can also be expressed in terms of the relative numbers of particles N_+ and N_- that have a positive or negative spin projection with respect to the magnetic field direction. N_+ and N_- are normalized to $N_+ + N_- = 1$ and identical to p_i in (2.8).

$$\begin{aligned} P_z &= N_+ - N_- \\ P_x &= P_y = 0 \end{aligned} \tag{2.11}$$

With

$$-1 \leq P_z \leq 1. \tag{2.12}$$

Spin-1 particles can be treated in a similar way. The spin-1 operator has three eigenvalues rather than two, which makes the density operator (2.8) a 3×3 matrix. This means that there are now eight degrees of freedom for the polarization, corresponding to 3×3 minus one for normalization. Therefore, the polarization cannot be described by a single vector as in (2.9). Instead, the density matrix can be parametrized as

$$\rho_{ij} = \frac{1}{3}\delta_{ij} + \sum_k \varepsilon_{ijk} P_k + P_{ij}, \tag{2.13}$$

where P_k is the polarization vector, P_{ij} is the polarization tensor, δ is the Kronecker delta and ε is the antisymmetric tensor.

In Cartesian coordinates, P_k and P_{ij} are related to the spin operator $\boldsymbol{S}$

$$\begin{aligned} P_i &= \frac{1}{\hbar}\langle S_i \rangle \\ P_{ij} &= \frac{3}{2\hbar^2}\langle S_i S_j + S_j S_i \rangle - 2\delta_{ij} \end{aligned} \tag{2.14}$$

Similar to (2.11), they can be expressed as a function of the number of particles in the different spin states [22].

$$\begin{aligned} P_z &= N_+ - N_- \\ P_{zz} &= 3(N_+ + N_-) - 2(N_+ + N_0 + N_-) = 1 - 3N_0 \\ P_{xx} &= P_{yy} = -\frac{1}{2}(1 - 3N_0) \end{aligned} \tag{2.15}$$

With the lower and upper bounds

$$\begin{aligned} -1 &\leq P_z \leq 1 \\ -2 &\leq P_{zz} \leq 1. \end{aligned} \tag{2.16}$$

Note that the bounds are not completely independent. For example, a tensor polarization of $P_{zz} = -2$ implies a vector polarization of zero and a vector polarization of $P_z = \pm 1$ implies $P_{zz} = 1$.

2.2.2. Spin in Nuclear Reactions

The behavior of polarized beams differs from the unpolarized case. In a reaction induced by an unpolarized beam, there is no distinguished direction except the beam axis. Therefore the distribution of scattered particles is invariant under a rotation about the beam axis. A polarized beam introduces an additional fixed axis, so the differential scattering cross sections are no longer independent of the azimuth. This azimuth asymmetry is the basis for most hadron polarimeters, including EDDA (see section 3.1.3) and the Low Energy Polarimeter (see section 4).

The notation and coordinate conventions outlined in the following section are adapted from Ohlsen and Keaton [23]. Fig. 2.2 shows the coordinate system. Given the momentum vectors of the incident particle $\boldsymbol{k}_{\text{in}}$ and the outgoing particle $\boldsymbol{k}_{\text{out}}$, the z-axis is defined to be parallel to $\boldsymbol{k}_{\text{in}}$, and the y-axis is parallel to $\boldsymbol{k}_{\text{in}} \times \boldsymbol{k}_{\text{out}}$. The x-axis forms a right-handed coordinate system with the other two. ϕ is defined as the angle between the spin axis projected into the x-y-plane, β is the angle between the spin axis and the z-axis. The left side of the detector is at $\phi = 0°$, right is at $\phi = 180°$, up is at $\phi = 270°$ and down at $\phi = 90°$. β is $90°$ in the experiments at the Low Energy Polarimeter (see section 4) as the spin axis is vertical, while the beam is horizontal.

The dependence of scattering reactions on the beam polarization is characterized by the so-called analyzing power $\boldsymbol{A}$. For a spin-$1/2$ particle the cross section is [20, chapter 3]

$$\sigma(\theta, \phi) = \sigma_0(\theta) \left(1 + \boldsymbol{P} \cdot \boldsymbol{A}(\theta)\right), \tag{2.17}$$

with the scattering angle θ and the unpolarized cross section σ_0. The cross sections are actually differential cross sections $\frac{d\sigma}{d\Omega}$, but written here as σ for ease of notation.

Using the above coordinate system and the assumption $\beta = 90°$, this simplifies to

$$\sigma(\theta, \phi) = \sigma_0(\theta) \left(1 + A_y P \cos \phi(\theta)\right), \tag{2.18}$$

with $P = |\boldsymbol{P}|$.

The cross section for spin-1 particles has a similar form that takes the tensor polarization into account as well.

$$\sigma(\theta, \phi) = \sigma_0(\theta) \left(1 + \frac{3}{2}\boldsymbol{A} \cdot \boldsymbol{P} + \frac{1}{3}\sum_{ij} P_{ij} A_{ij}\right) \tag{2.19}$$

Here $\boldsymbol{A}$ is the vector analyzing power, which works analogously to the spin-$1/2$ case while A_{ij} is the tensor analyzing power. The components A_{yz}, A_{xy} violate parity and are effectively zero as nuclear scattering reactions are dominated by the strong interaction. Like the tensor polarization, the tensor analyzing power is traceless:

$$A_{xx} + A_{yy} + A_{zz} = 0. \tag{2.20}$$

Using these simplifications and again $\beta = 90°$, the cross section becomes:

$$\sigma(\theta, \phi) = \sigma_0(\theta) \left(1 + \frac{3}{2}P_{\text{vec}} A_y \cos\phi + \frac{1}{2}P_{\text{tens}} \left(A_{xx}\sin^2\phi + A_{yy}\cos^2\phi\right)\right) \tag{2.21}$$

While the vector polarization leads to a 2π-periodic modulation in ϕ, the effect of tensor polarization is π-periodic.

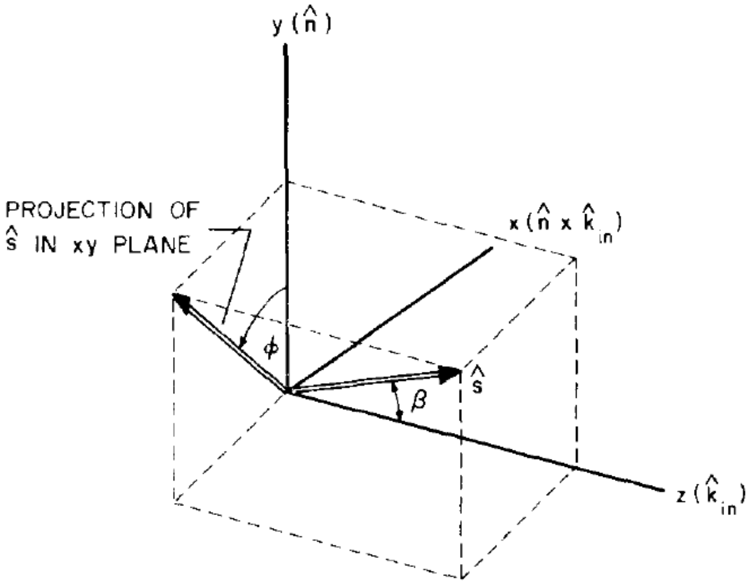

Figure 2.2.: Coordinate definitions for polarized particle scattering [23]

2.2.3. Polarimetry

Equations (2.17) and (2.21) are the basis for polarization measurements. Both EDDA and the Low Energy polarimeter measure the event rates of particles scattered up, down, left and right. The polarization can be inferred from the asymmetries of the rates if the analyzing power is known. Several different asymmetries can be constructed from the four different rates [23, table 1].

Table 2.2.: Observables in spin-1 polarimetry measurements and their statistical uncertainty [23, table 1, abridged]. L, R, U and D stand for the rates in each direction.

Asymmetry	Statistical Uncertainty	Polarization Observables
$\varepsilon_{\text{vec}} = \frac{L-R}{L+R}$	$\sqrt{\frac{1-\varepsilon_{LR}^2}{L+R}}$	$\frac{3}{2}\frac{P_{\text{vec}}A_y}{1+\frac{1}{2}P_{\text{tens}}A_{yy}}$
$\varepsilon_{\text{tens}} = \frac{(L+R)-(U+D)}{(L+R)+(U+D)}$	$\sqrt{\frac{1-\varepsilon_{\text{tens}}^2}{(L+R)+(U+D)}}$	$\frac{P_{\text{tens}}(A_{yy}-A_{xx})}{1+\frac{1}{4}P_{\text{tens}}(A_{yy}+A_{xx})}$

Table 2.2 shows the most important asymmetries for a spin-1 particles, such as deuterons. The statistical errors are given under the assumption that the errors of the rates are simple counting error $\sigma_N = \sqrt{N}$. The left-right asymmetry is used to measure vector polarization, the asymmetry between the detectors in the horizontal and the vertical plane is used for tensor polarization.

The relative error of the asymmetries depends on the beam polarization. It is not possible to find a trade-off between rate and analyzing power that is optimal for every polarization value. A figure of merit can be defined as σA_y^2 for vector polarization and

$\sigma\left(A_{yy}-A_{xx}\right)^2$ for tensor polarization, in analogy to the discussion of analyzing power measurements by Ohlsen and Keaton. This figure is inversely proportional to the squared relative error for $\varepsilon \approx 0$. For large polarizations, the figure of merit underestimates the advantage of large analyzing powers compared to large cross sections. [23]

Polarization measurements are susceptible to several systematic errors [23, 24]. While a perfect polarimeter would measure vanishing asymmetries for an unpolarized beam, real experiments find systematic discrepancies. The most important sources of systematic errors are detector efficiencies and the beam position.

Particle detectors always miss a certain fraction of events, which is never precisely the same on both sides of the beam.

The beam can be inclined with respect to the polarimeter or not aimed precisely at the center of the target. The effects of misalignment are discussed in detail by Brantjes et al. [24]. The two sides of the polarimeter are effectively not at the same scattering angle if the beam is not centered. As the cross section and the analyzing power are functions of θ, they are different for the two detectors as well. Additionally, the effective solid angle covered by the different detectors depends on the beam alignment, causing more fake asymmetry.

The effects of systematic errors can be mitigated by examining several different polarization states. At COSY and at most other polarized particle accelerators, an unpolarized beam is available. The polarization of that beam is known to be precisely zero, so any asymmetry that is still measured must be spurious and can be used to correct the measurements for the polarized states.

Another option is the so called cross ratio, which makes use of a positive and a negative polarization state.

$$\varepsilon_{CR} = \frac{r-1}{r+1} \tag{2.22}$$

with

$$r^2 = \frac{L_+ R_-}{L_- R_+} \tag{2.23}$$

where $L_\pm$ and $R_\pm$ are the event rates in the left and right detector for positive and negative polarization states. [24]

2.2.4. Review of Analyzing Power Data

Any measurement of beam polarizations requires a known analyzing power for calibration. This section gives an overview of existing data near the COSY injection energy of 75 MeV for deuterons. While no literature data exists at that precise value, an estimate can be made from results at similar energies.

One aim of the upgrade of the LEP read-out system was to facilitate analyzing power measurements at LEP itself to improve later calibration. The literature review is also relevant with respect to that goal.

The cross section (2.21) is only sensitive to products of the polarizations and analyzing powers. Therefore, all polarization measurements need an analyzing powers for calibration and all analyzing power measurements need the beam polarizations used in the experiment. For certain reactions, the conservation of angular momentum and parity guarantees that the analyzing powers must have certain extreme values [25]. These reactions can be used to resolve the circular dependence of analyzing power and polarization calibration. For example, all reactions with spins and parities in the form $1^+ + 0^+ \to 0^+ + 0^-$ have the analyzing power $A_{yy} = 1$. At the same time, the other components of the analyzing power must satisfy $A_y^2 + \frac{4}{9}A_{xz}^2 + \frac{1}{9}(A_{zz} - A_{xx})^2 = 1$ [25, 26]. A number of similar relations can be found for different combinations of spins and parities [25].

None of the reactions that can easily be identified with the Low Energy Polarimeter has a spin and parity configuration that guarantees extreme values. Most possible reactions with two spin-0 particles in the final state have outgoing α-particles, which loose most of their energy in the exit windows. They also require isolating specific excited final states, which is not possible given the energy resolution of the plastic scintillators.

The calibration of the polarization measurements at LEP instead relies on literature values. Vector polarization is measured by elastic scattering on a carbon target. However, this reaction is not very sensitive to tensor polarization. Elastic deuteron proton scattering could be suitable for tensor polarization measurements, but was not measured with polarized beams in this thesis.

Kato et al. provide measurements of elastic d-^{12}C scattering at energies from 35 to 70 MeV for angles from 30° to 65° in the laboratory frame. The measurement includes A_y and A_{yy} for the complete energy range, A_{xx} from 35 to 56 MeV and A_{xz} for 49 MeV and 56 MeV. The beam polarization was calibrated using the reaction $^{16}\mathrm{O}(d,\alpha)^{14}\mathrm{N}$ with 4.915 MeV excitation energy in the final state, for which A_{yy} is one because of conservation laws, as outlined above. The vector analyzing power is calibrated using the interdependency of the polarizations of the different beam states. The ion source used radio frequency transitions (RFT), which were used alone or in combination. As the efficiencies of the RFTs remain constant, this results in relations between the different polarizations.

The results for A_y and A_{yy} are reproduced in fig. 2.3. The highest beam energy used is 70 MeV, 5 MeV below the COSY injection energy. The vector analyzing power vanishes for small angles an becomes large at about 40° or more. The tensor analyzing power is vanishingly small for angles below about 50°. [26]

The vector analyzing power at the actual COSY injection energy was estimated as $A_y = 0.61 \pm 0.04$ at 40°. This estimate is based on the Kato et al. measurement and another unpublished data set taken at the KVI in Groningen [27, 28]. The results agreed with complementary measurements at EDDA. The tensor analyzing power at this angle and energy is too small for practical measurements.

A review of deuteron proton scattering reactions is given by Glöckle et al. [29]. Deuteron proton elastic scattering has large tensor analyzing powers at the relevant energy and angle range. Fig. 2.4 shows results in the relevant energy range. The

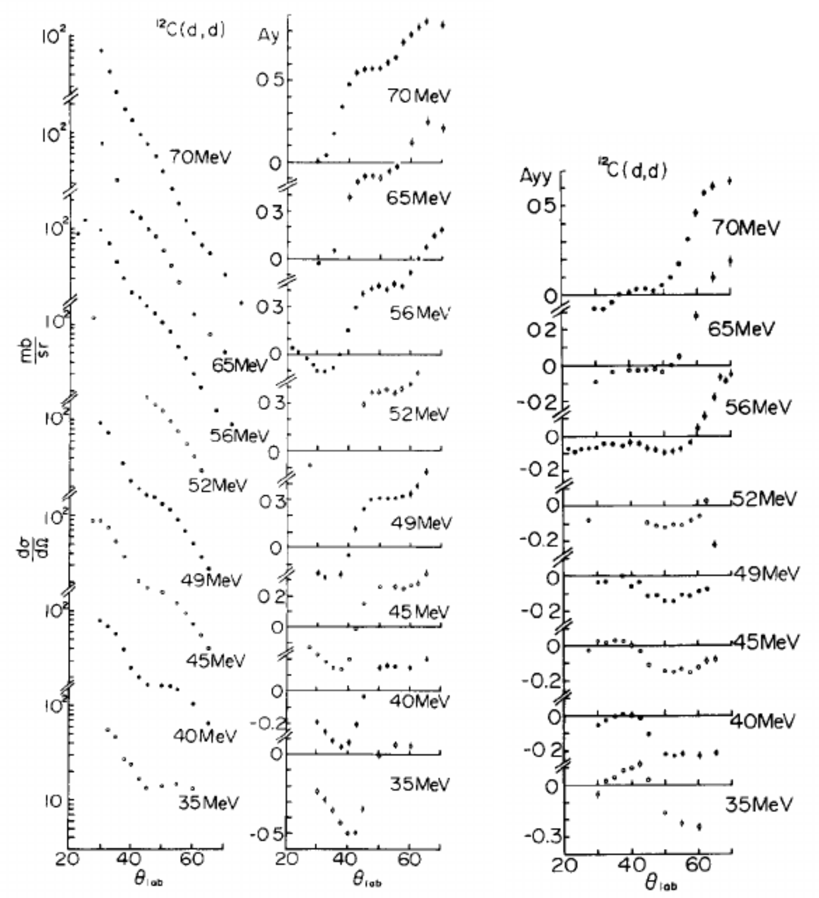

Figure 2.3.: Results for dC elastic scattering for σ, A_y and A_{yy} [26]

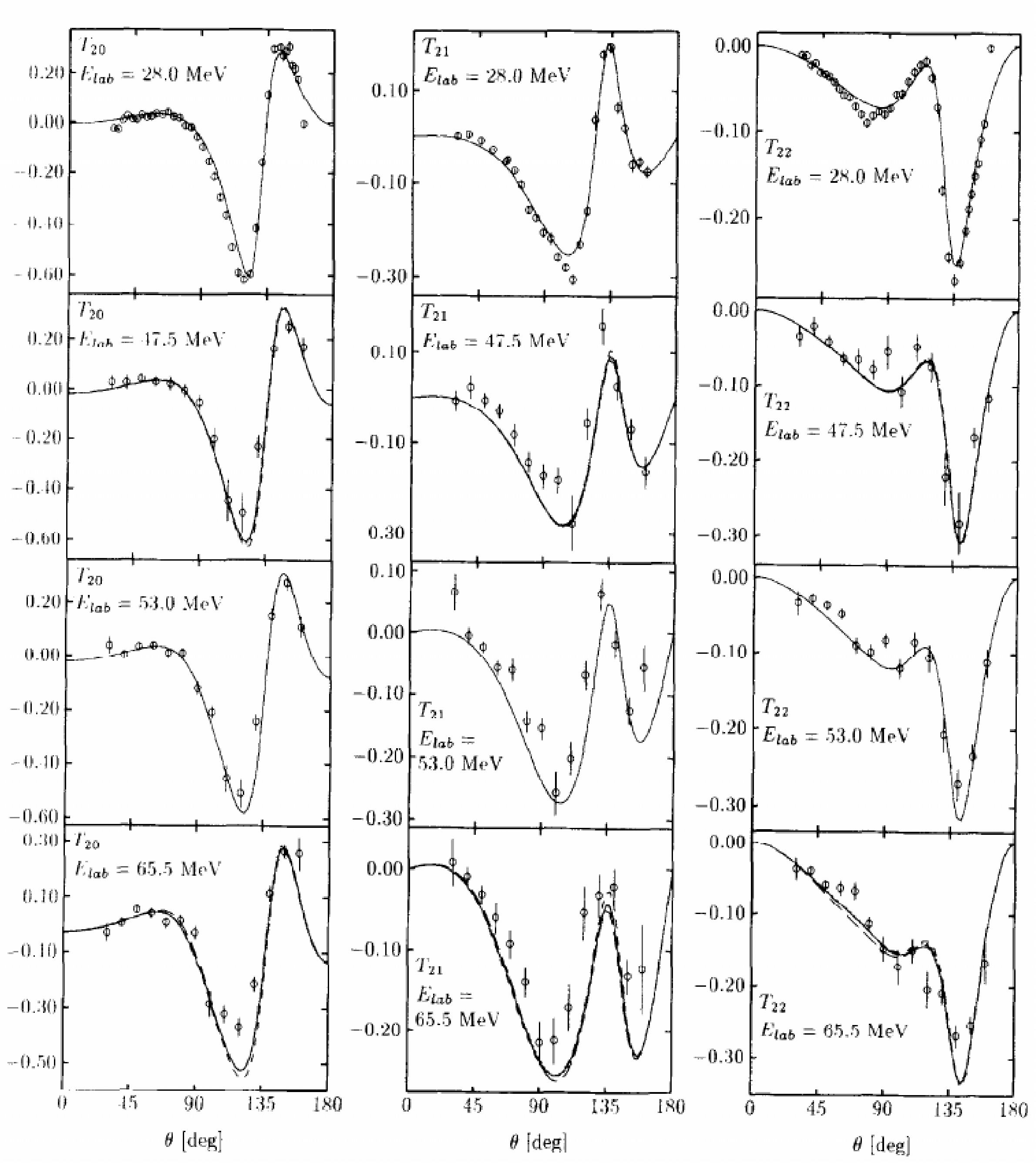

Figure 2.4.: Results for dp elastic scattering [29]. The given energies are per nucleon, i.e. half the deuteron kinetic energy.

analyzing powers are written in spherical coordinates defined as

$$\begin{aligned} iT_{11} &= \frac{\sqrt{3}}{2} A_y \\ T_{20} &= \frac{1}{\sqrt{2}} A_{zz} \\ T_{21} &= \frac{-1}{\sqrt{3}} A_{xz} \\ T_{22} &= \frac{1}{2\sqrt{3}} (A_{xx} - A_{yy}) \end{aligned} \tag{2.24}$$

Unlike a carbon nucleus, the recoil proton in this reaction can leave the target and be registered in the detectors. This allows for a coincidence measurement that reduces the background (see section 4.3.2). As the detectors of LEP are spaced 10° apart, symmetrical measurements are only possible if the recoil and ejectile angles differ by 0°, 10° or 20°.

Table 2.3.: Possible angles for coincidence measurements at LEP

$\Delta\theta_{\mathrm{lab}}$	θ_{cm}	θ_d	θ_p
0°	119.1°	30.0°	30.0°
10°	101.9°	28.6°	38.6°
20°	87.2°	25.9°	45.9°

Other angles could be used if the detector spacing was modified or by measuring without coincidence. Some of the largest analyzing powers are inaccessible because of the limited angular acceptance of LEP. The deuteron scattering angle in the laboratory frame is only above the minimum value of 25° if the center of mass angle is between 83° and 148°. Recoil protons are between 25° and 70° in the laboratory frame if the center of mass angle is between 39° and 129°.

2.3. EDM Measurement in Storage Rings

2.3.1. Principle

EDMs can only be detected using their interaction with electric fields. By using storage rings, a charged particle can be in an electric field in its own rest frame and still confined. An electric field $\boldsymbol{E}^*$ in the particles rest frame tilts the electric dipole moment $\boldsymbol{d}$, which must be parallel or antiparallel to the spin vector $\boldsymbol{P}$ [2].

$$\frac{d\boldsymbol{P}}{dt} = \boldsymbol{d} \times \boldsymbol{E}^* \tag{2.25}$$

All proposed storage ring experiments use this tilt to detect an EDM. The polarization vector is initially in the horizontal plane, the EDM then rotates it upwards or downwards out of the plane.

When the effect of the magnetic dipole moment is included, the spin motion is governed by the Thomas-BMT equation, [30], which can be simplified assuming that the electric and magnetic fields are perpendicular to the beam direction [2].

$$\begin{aligned} \frac{d\boldsymbol{P}}{dt} &= \boldsymbol{P} \times \boldsymbol{\Omega} \\ \boldsymbol{\Omega} &= \frac{e\hbar}{mc}\left[G\boldsymbol{B} + \left(G - \frac{1}{\gamma^2 - 1}\right)\boldsymbol{E} \times \boldsymbol{v} + \frac{1}{2}\eta\left(\boldsymbol{E} + \boldsymbol{v} \times \boldsymbol{B}\right)\right] \end{aligned} \tag{2.26}$$

$G = \frac{1}{2}(g-2)$ is the anomalous g-factor and η is a parameter for the electric dipole moment $d = \eta\frac{e\hbar}{2mc}$.

For an EDM-measurement, the parameters must be chosen such that (2.26) results in a macroscopic build-up of vertical polarization over time. Different methods for that have been proposed, which will be discussed in the next sections.

2.3.2. Magnetic Storage Rings

Storage rings, including COSY, typically use magnets to bend the beam around curves and for focusing. The required vertical magnetic fields cause a rapid spin precession around the vertical axis, due to the magnetic dipole moment. Setting $\boldsymbol{E} = 0$ in (2.26) yields [2]

$$\boldsymbol{\Omega} = \frac{e\hbar}{mc}\left[G\boldsymbol{B} + \frac{1}{2}\eta\boldsymbol{v} \times \boldsymbol{B}\right]. \tag{2.27}$$

The first term corresponds to the horizontal precession because of the magnetic dipole moment, the second term is the effect of the EDM.

The so-called spin tune can be defined as the ratio of the spin frequency and the revolution frequency of the beam:

$$\nu_s = \frac{f_{\text{spin}}}{f_{\text{beam}}}. \tag{2.28}$$

In an ideal ring the spin tune is $\nu_s = G\gamma$. The spin tune is the number of spin rotations between successive turns seen by an observer at a fixed position in the ring.

A magnetic storage ring was used to measure the electric dipole moment of muons parasitically in an experiment mainly intended to measure the g-factor at the Brookhaven National Laboratory (BNL). The ring used electric focusing elements, but the magnetic fields were dominant in a possible interaction with an EDM. The momentum was set to the "magic" value of 3.094 GeV to minimize the effect of electric fields (see also section 2.3.3).

Muon polarization can be measured using the angular distribution of the electrons and positrons emitted in muon decay, because muon decay is a weak process that maximally violates parity. Electrons from μ^--decay are more likely to be emitted opposite to the spin direction, positrons from μ^+-decay are mostly emitted in spin direction. A non-vanishing EDM leads to an oscillation of the vertical beam polarization. [31, 32]

This method is not well-suited for charged hadrons [1]. The muon magnetic anomaly is in the order of 10^{-3}, for protons it is about 1.79, for deuterons about -0.14. The larger G causes a faster precession about the vertical axis, leading to smaller vertical oscillations. An EDM in the order of 10^{-18} to 10^{-17} would be needed to reach the same tilt angle as in the muon measurement [1].

Hadron EDM-measurements could still be measured in purely magnetic rings using an rf Wien filter (see section 2.3.4).

2.3.3. Electric and Combined Storage Rings

In a storage ring using only electric elements, equation (2.26) reduces to

$$\boldsymbol{\Omega} = \frac{e\hbar}{mc}\left[\left(G - \frac{1}{\gamma^2 - 1}\right)\boldsymbol{E}\times\boldsymbol{v} + \frac{1}{2}\eta\boldsymbol{E}\right]. \tag{2.29}$$

For particles with $G > 0$, the contribution of the magnetic dipole moment can be reduced to zero by setting the momentum to the “magic” value of

$$p_{\text{magic}} = \frac{m}{G}, \tag{2.30}$$

for which $G - (\gamma^2 - 1)^{-1} = 0$. A measurement of the proton EDM with a purely electric ring has been proposed at BNL [33].

Purely electric rings do not work for deuterons as their anomalous magnetic moment is below zero. By using a combination of electric and magnetic fields, the contribution of the magnetic dipole moment to the spin precession can be set to zero for an arbitrary particle. The condition is

$$G\boldsymbol{B} + \left(G - \frac{1}{\gamma^2 - 1}\right)\boldsymbol{E}\times\boldsymbol{v} = 0. \tag{2.31}$$

A combined magnetic and electric ring for EDM measurement is being studied by the JEDI collaboration in Jülich. [2]

2.3.4. Wien Filter Method

As discussed in section 2.3.2, an EDM leads to an oscillation of the vertical beam polarization in a magnetic ring. The small oscillation can be converted to a macroscopic build-up over time by inserting an rf Wien filter into the ring [34, 35]. A Wien filter is a device consisting of a magnetic and an electric field that are perpendicular to each other and to the beam. The total force on the beam must be zero at the desired momentum. Particles of a different momentum are deflected to the side as either the magnetic or the electric force is stronger than the other, hence the name filter.

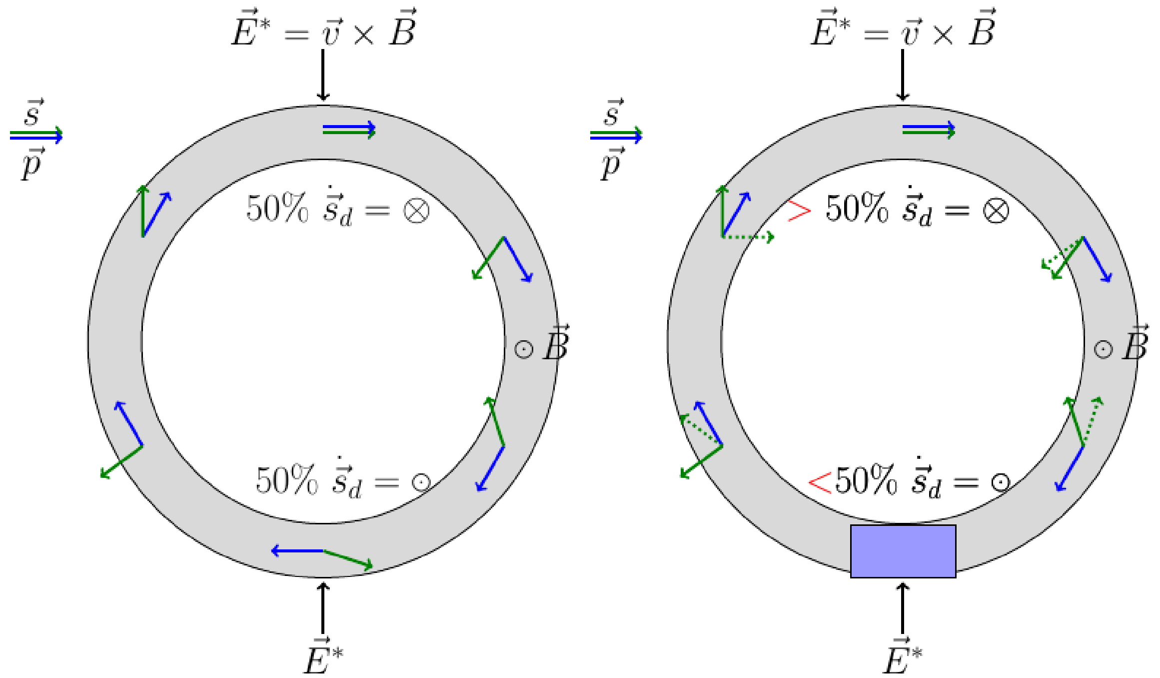

Figure 2.5.: Principle of an EDM measurement using a Wien filter [2]

Fig. 2.5 shows the principle of an EDM measurement using a Wien filter. In an unperturbed magnetic ring, the spin points in the direction of the momentum and in the opposite direction half the time each. The Wien filter rotates the spin about the vertical axis, breaking the symmetry of upward and downward motion. The Wien filter would be operated on a spin resonance frequency, i.e. there would be a fixed phase relation between the spin precession and the Wien filter signal.

The calculation of the effects of the Wien filter is described analytically in [35] and numerically in [1]. The effect of the Wien filter can be interpreted as a constant component to the in-plane polarization vector in addition to a rapidly precessing mode that also exists in an unperturbed ring. The radial and longitudinal polarization (P_R and P_L) can be described by the equations [35]

$$\begin{aligned} P_L &= P_0 \cos\phi \\ P_R &= P_0 \sin\phi \\ \phi &= \nu_s \omega_C t - \frac{eB_{\text{Wien}}}{mc\nu_s\omega_C} \frac{1+G}{\gamma^2} \sin(\nu_s \omega_C t), \end{aligned} \tag{2.32}$$

where ω_C is the angular revolution frequency, B_{Wien} is the field strength of the Wien filter and ν_S is the spin tune. Expanding equation (2.32) in the term proportional to the Wien filter field makes the constant component more apparent [35].

$$\begin{aligned}\cos\phi \approx \cos\left(\nu_s\omega_C t\right) + \frac{1}{2}\left(1-\cos\left(2\nu_s\omega_C t\right)\right)\frac{eB_{\mathrm{Wien}}}{mc\nu_s\omega_C}\frac{1+G}{\gamma^2} \\ -\frac{1}{4}\cos\left(\nu_s\omega_C t\right)\left(1-\cos\left(2\nu_s\omega_C t\right)\right)\left(\frac{eB_{\mathrm{Wien}}}{mc\nu_s\omega_C}\frac{1+G}{\gamma^2}\right)^2 \\ +\mathcal{O}\left(\left(\frac{eB_{\mathrm{Wien}}}{mc\nu_s\omega_C}\frac{1+G}{\gamma^2}\right)^3\right).\end{aligned} \tag{2.33}$$

The trigonometric functions average out to zero over time, the remaining terms are the mean longitudinal polarization.

To the first order, the build-up of vertical polarization due to the EDM is

$$\left(\frac{dP_V}{dt}\right)_{\mathrm{EDM}} = \eta\frac{eB_{\mathrm{Wien}}}{4mc}\frac{1+G}{\gamma^2}P_0\frac{e\left(-E_R+\beta B_V\right)}{mc\nu_s\omega_C}, \tag{2.34}$$

where E_R is the radial electric field in the ring (zero for a purely magnetic one) and B_V is the radial magnetic field [35].

The above calculations are under the assumption that the phase between the Wien filter rf signal and the spin rotation remains fixed at zero, which results in the maximum possible EDM signal. An active feedback system is required to keep the phase difference fixed over the necessary time spans in the order of 1000 s. The feedback system is discussed in detail in chapter 5.

3. Polarized Beams in COSY

3.1. Cooler Synchrotron (COSY)

3.1.1. Main Storage Ring

The Cooler Synchrotron (COSY) [36] is a storage ring for polarized protons and deuterons located at Forschungszentrum Jülich. Fig. 3.1 shows the COSY ring. COSY is a race-track storage ring with a total circumference of about 184 m. Particles can be accelerated to momenta up to 3.5 GeV/c.

The most distinctive feature of COSY is the eponymous beam cooling, which means shrinking the beam phase space. Up to a momentum of 600 MeV/c for protons or 1200 MeV/c for deuterons a so-called electron cooler is used [37]. The electron cooler is located in the straight section of COSY and works by injecting an electron beam at the same velocity and position as the main hadron beam. This electron beam has a smaller phase space compared to the main beam. Through Coulomb interaction, transverse momentum can be transferred from the main beam to the electron beam. Stochastic cooling is used for higher momenta from 1500 MeV/c upward.

COSY provides a beam to several experiments, including EDDA (see section 3.1.3) and WASA [38]. The beam can also be extracted to an external experimental area.

3.1.2. Polarized Source

The polarized particle source at COSY [39, 40, 27] is a colliding beam source [22]. Fig. 3.2 shows the layout of the source. The basic principle is to first create a beam of electrically neutral, polarized hydrogen or deuterium atoms. This atomic beam collides with a beam of atomic cesium, causing one electron to be transferred from a cesium atom to the polarized atom. The polarization of the nucleus is preserved in the resulting negative ion. The negative ions can then be extracted and sent to the cyclotron, where they are accelerated and injected into COSY.

In the atomic beam source, the hydrogen or deuterium molecules are first dissociated into individual atoms using an electric discharge. Small amounts of oxygen and nitrogen are added to reduce recombination. The atoms pass through a nozzle, cooling them to about 30 K.

The dissociated atoms are polarized using the magnetic moment of their electron and hyperfine coupling. The electron angular momentum L (0 in the ground state) and spin S couple to a total spin J. In a weak magnetic field, small compared to a certain value B_{crit}, this spin couples with the nuclear spin I to a total spin F. In larger fields, F is no

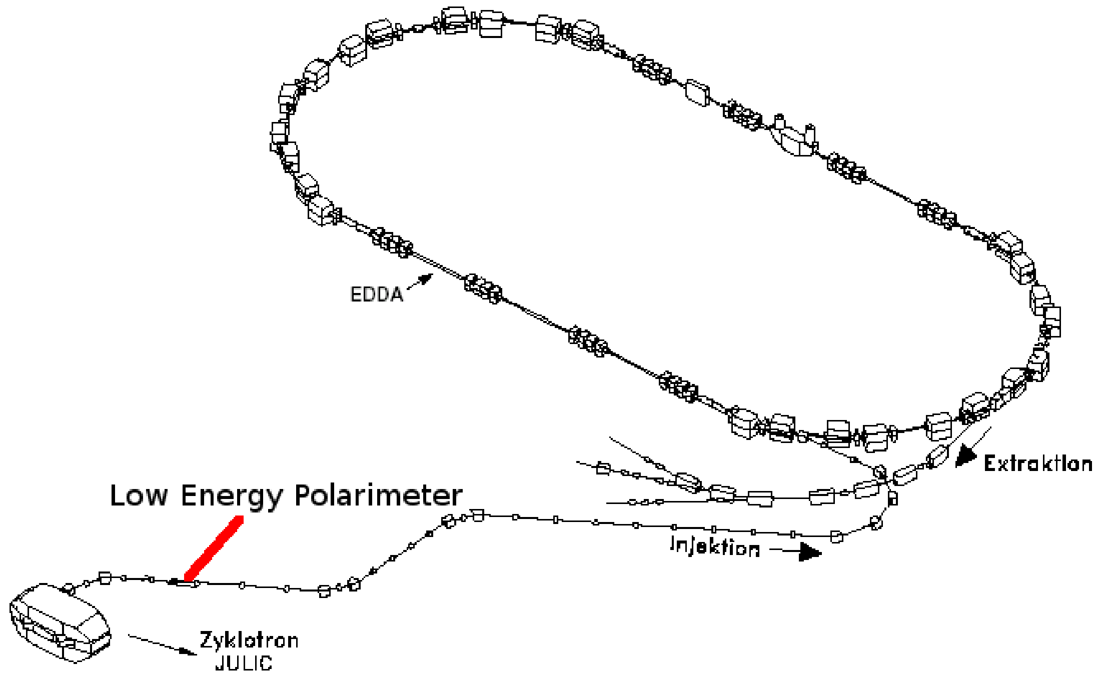

Figure 3.1.: Layout of COSY

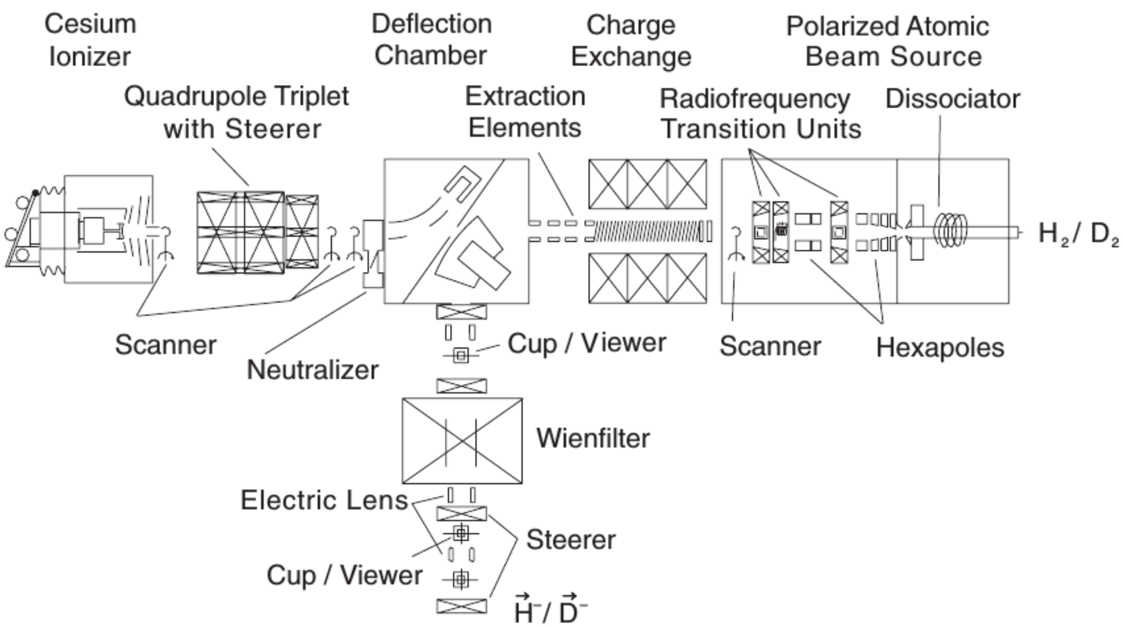

Figure 3.2.: Polarized beam source at COSY [27]. The cesium beam is produced in the left branch of the T-shaped setup, the polarized beam of hydrogen or deuterium atoms is produced in the right branch. The negative ions created in the collision are extracted through the branch at the bottom of the picture.

longer a good quantum number because J and I couple more strongly to the external field than to each other [22, 40].

The critical field is defined as

$$B_{\text{crit}} = \frac{\Delta W}{(g_I - g_J)\mu_B}, \tag{3.1}$$

where ΔW is the hyperfine splitting without a magnetic field, μ_B is the Bohr magneton and g_I and g_J are the nuclear and electron g-factors. The numerical values are $\Delta W = 5.8 \cdot 10^{-6}$ eV and $B_{\text{crit}} = 50.7$ mT for protons, and $\Delta W = 1.4 \cdot 10^{-4}$ eV and $B_{\text{crit}} = 11.7$ mT for deuterons.

Tables 3.1 and 3.2 show the quantum numbers of the hyperfine states of hydrogen and deuterium for weak and strong fields. The states are numbered from highest to lowest energy.

Table 3.1.: Hydrogen hyperfine states [22]

	$B \ll B_{\text{crit}}$		$B \gg B_{\text{crit}}$	
State	F	m_F	m_J	m_I
1	1	1	$1/2$	$1/2$
2	1	0	$1/2$	$-1/2$
3	1	-1	$-1/2$	$-1/2$
4	0	0	$-1/2$	$1/2$

Table 3.2.: Deuterium hyperfine states [22]

	$B \ll B_{\text{crit}}$		$B \gg B_{\text{crit}}$	
State	F	m_F	m_J	m_I
1	$3/2$	$3/2$	$1/2$	1
2	$3/2$	$1/2$	$1/2$	0
3	$3/2$	$-1/2$	$1/2$	-1
4	$3/2$	$-3/2$	$-1/2$	-1
5	$1/2$	$-1/2$	$-1/2$	0
6	$1/2$	$1/2$	$-1/2$	1

Fig. 3.3 shows the energy levels as a function of the magnetic field, figs. 3.5 and 3.4 show the corresponding nuclear polarizations. If all states are occupied equally, the beam is unpolarized. Polarized beams are created by changing the relative occupation.

After the nozzle, the atoms enter a magnetic hexapole. The magnetic fields in the hexapole are in the strong regime, acting on the electron dipole moment J, causing a focusing force for the states with positive m_J and a defocusing force for others. As the defocused components are removed, the resulting beam is polarized in radial direction. However, the net nuclear polarization of the remaining hyperfine states is zero in large fields, which can be seen in the graphs.

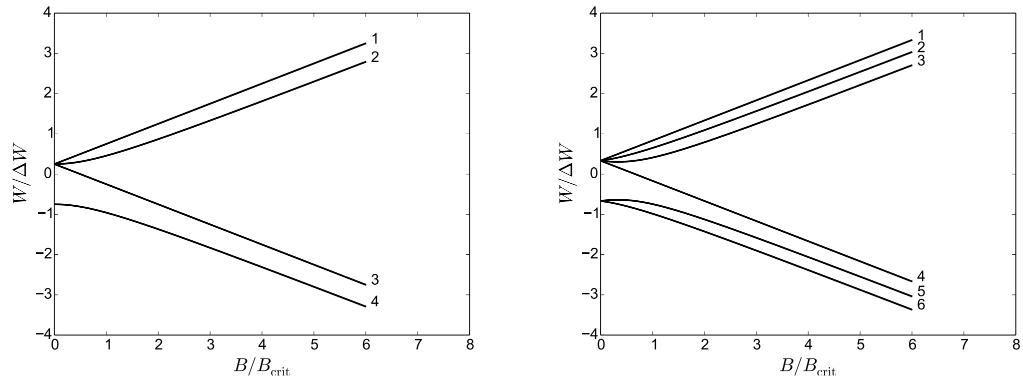

Figure 3.3.: Hyperfine states for hydrogen (left) and deuterium (right) as a function of the magnetic field [22, reproduced].

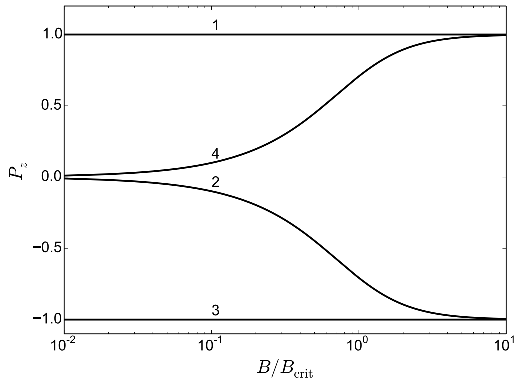

Figure 3.4.: Polarization of the hyperfine states of hydrogen as a function of the magnetic field [22, reproduced].

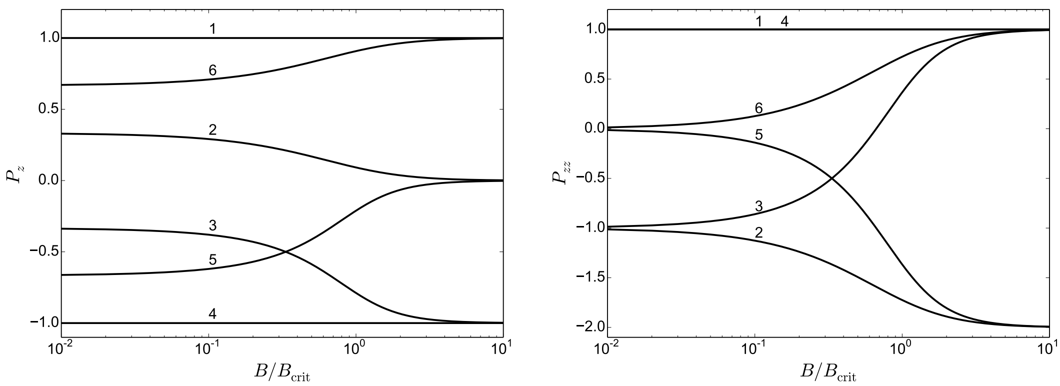

Figure 3.5.: Polarization of the hyperfine states of deuterium as a function of the magnetic field [22, reproduced].

To obtain a nuclear polarized beam, the relative occupation of the hyperfine states is changed using three radio frequency transfers (RFT). These consist of an adjustable magnetic field that causes a split between the hyperfine energy levels and a radio frequency electromagnetic signal to induce transitions between the different states. Different combinations of vector and tensor polarization can be achieved by using different combinations of RFTs, see [27]. For example, a deuteron state with a vector polarization of $-2/3$ and a tensor polarization of zero is obtained by transferring particles from state 1 to state 4. In practice, the RFTs are imperfect, leading to lower polarizations. Typically, the polarization state is changed after every COSY cycle.

The second part of the polarized source is the cesium beam. The cesium atoms are first ionized at the surface of a porous tungsten button and then accelerated electrostatically to around 45 keV to achieve an optimal cross section for the charge exchange reaction. The beam of ionized cesium is then neutralized in a cell of cesium vapor. Any remaining ions in the beams are deflected to the side.

The neutral cesium beam and the polarized atomic beam collide in a central charge exchange region, which lies inside a solenoid that determines the spin quantization axis. At up to 200 mT, the magnetic field is strong compared to the critical field of both protons and deuterons. The charge exchange reaction $\mathrm{H} + \mathrm{Ce} \longrightarrow \mathrm{H}^- + \mathrm{Ce}^+$ produces negatively charged ions that can be extracted. Finally, the polarized beam passes a Wien filter that rotates the spin to match the direction of the magnetic field in the cyclotron.

3.1.3. EDDA

The EDDA (Elastic Dibaryons, Dead or Alive?) [41, 42] detector is located in one of the straight sections of COSY. EDDA can be used as a polarimeter in the COSY ring to measure the vertical and in-plane polarization. Fig. 3.6 shows a drawing of EDDA. The detector consists of plastic scintillators that are arranged in an inner layer of 32 bars parallel to the beam and an outer layer of rings around the beam. Photomultiplier tubes are used to read out the signals.

For the purpose of polarization experiments, the bars of EDDA are grouped into four

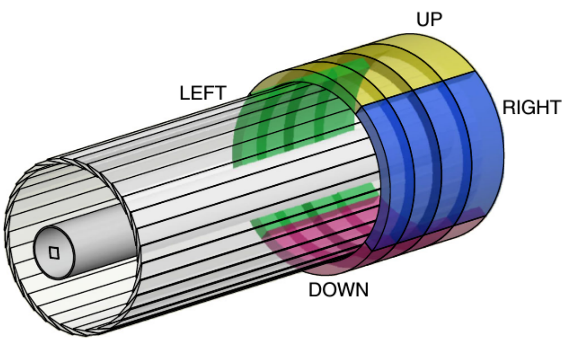

Figure 3.6.: Layout of the EDDA detector [41]. Only the rings that are used in the polarization measurement are shown.

segments corresponding to the cardinal directions: up, down, left and right. The vertical beam polarization can be determined directly from the asymmetry between the left and right counting rates. Although the radial polarization component could in principle be found the from the up-down-asymmetry, the rapid precession of the in-plane polarization in magnetic guiding field makes this method impractical. The in-plane polarization requires a more complicated analysis described in section 3.2.2.

One essential requirement for measuring the in-plane polarization is to precisely know the time of each measured event. As the polarization precesses rapidly, at about 120 kHz, the time-integrated rates in the up and down detectors are essentially symmetric. Knowing the time of each event, and by inference the number of turns the beam has taken around the ring, facilitates the reconstruction of the in-plane polarization and spin tune (see sec. 3.2.2).

Fig. 3.7 shows the read-out electronics used for the EDDA detector for one of the four directions. To count as a hit, the deposited energy of a particle in the rings, in the bars and the sum of the energies must each be above a threshold. This is checked by the three discriminators connected to the “AND” gate. The resulting logic signal is connected to a time to digital converter (TDC), along with a time reference signal that arrives once for every 100 periods of the COSY acceleration frequency. The events are also counted in a scaler.

3.2. Spin Dynamics

3.2.1. Spin Precession and Coherence

COSY is a storage ring that uses dipole magnets to bend the beam around the curves, so the magnetic fields are mostly vertical. Therefore, vertical polarization in COSY is stable over long times as it is parallel to the quantization axis.

The horizontal polarization component precesses rapidly around the vertical axis. Typical frequencies for the measurements presented in this thesis were around 120 kHz for the spin precession and around 750 kHz for the COSY frequency, corresponding to spin tunes around 0.16.

As the beam is an ensemble of many particles with slightly different momenta, the different particles precess at different rates. Given enough time, the phase differences between the particles will add up and the horizontal polarization will decrease as the individual spins are pointing in different directions.

The spin coherence time can be defined as the time until the in-plane polarization drops to $e^{-1/2} = 0.606$ of its original magnitude [43]. A spin coherence time of around 1000 s was achieved at COSY [43], which is required to measure the electric dipole moment to the desired accuracy of $10^{-29}\,e\,\mathrm{cm}$ [43, 44]. Without measures to improve the lifetime, the in-plane polarization is lost over tens of milliseconds.

The long spin coherence time is achieved by multiple changes to the machine settings [43]. The beam is bunched using an rf cavity so that all particles take the same average time per turn. Electron cooling is used to reduce the momentum spread. These two

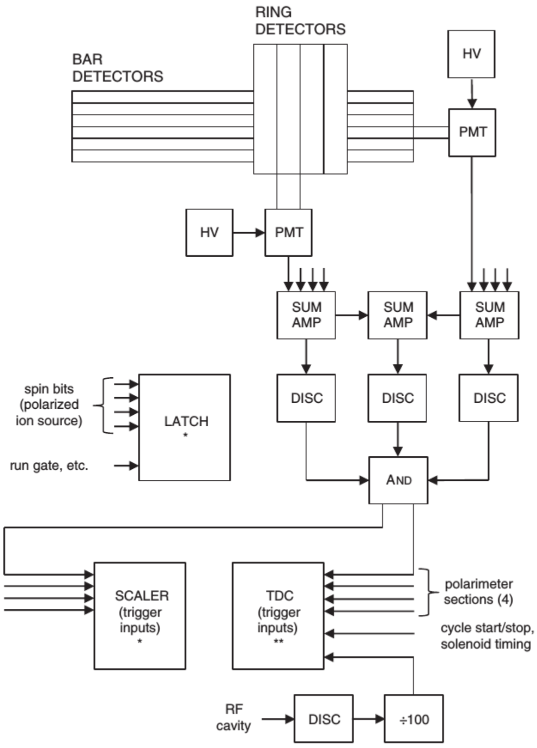

Figure 3.7.: Read-out scheme for EDDA [41]. Only one of the four directions is shown.

steps lead to coherence times of several seconds.

Even higher coherence times are achieved by optimizing the sextupole fields in the ring to compensate for second order effects. The particles oscillate transversely around the normal orbit, which increases the path length and therefore the momentum, as the beam is bunched. This effect is compensated by the sextupoles as they move oscillating particles to an orbit with a smaller radius in the arcs. Additionally, the sextupoles can be used to adjust the chromaticity of the ring. Small or zero chromaticity is associated with long spin coherence times [45].

3.2.2. Spin Tune Measurement

The spin tune ν_s, defined in equation (2.28), can be measured to a precision in the order of 10^{-8} during a time interval of 2.6 s using data from the time marking system (see section 3.1.3). A precision of 10^{-10} could be achieved over a period of 100 s [46].

The in-plane spin rotation, along with the scattering cross section for polarized beams (2.21), modulates the event rates on the upper and lower detector side. The main problem for spin tune measurements is that the spin precession (about 120 kHz) is far faster than the event rate in the detectors (about $5000\,\mathrm{s}^{-1}$). Only one event is recorded in about 24 spin revolutions, which makes a fit to the binned event rates impractical.

The spin tune is instead determined by mapping all events to two periods (4π) of the spin precession. First, the data is divided into segments 10^6 turns, within which the polarization and the spin tune are assumed to be constant. A phase $\phi_s = 2\pi n|\nu_s^0|$ is calculated for each event assuming a spin tune value ν_s^0. These phases are filled into one histogram each for the upper and lower detector side. If the assumed spin tune value is sufficiently close to the real one, this results in two sinusoidal functions with opposite signs.

From each of these histograms, a function oscillating around zero over 2π can be generated.

$$N_X^{\pm}(\phi_s) = \begin{cases} N_X(\phi_s) \pm N_X(\phi_s + 3\pi) & 0 < \phi_s < \pi \\ N_X(\phi_s) \pm N_X(\phi_s + \pi) & \pi < \phi_s < 2\pi \end{cases} \tag{3.2}$$

X is either up (U) or down (D). The sum is ideally constant, while the difference oscillates around zero.

Finally, the two rates are combined to one asymmetry

$$\begin{aligned} \varepsilon(\phi_s) &= \frac{N_D^-(\phi_s) - N_U^-(\phi_s)}{N_D^+(\phi_s) + N_U^+(\phi_s)} \\ &= \frac{3}{2} P_H \frac{\overline{\sigma_{0D}}\,\overline{A_{yD}} - \overline{\sigma_{0U}}\,\overline{A_{yU}}}{\overline{\sigma_{0D}} + \overline{\sigma_{0U}}} \sin\left(\phi_s + \tilde{\phi}\right). \end{aligned} \tag{3.3}$$

$\overline{\sigma_0}$ is the unpolarized scattering cross section averaged over the acceptance of the upper or lower detector, $\overline{A_y}$ is the average analyzing power and P_H is the in-plane polarization. $\tilde{\phi}$ is the starting phase of the spin precession. A sine curve is fitted to the result of (3.3).

$$\varepsilon = \tilde{\varepsilon} \sin\left(\phi_s + \tilde{\phi}\right) \tag{3.4}$$

The initial spin tune can be set to a value ν_s^{fix} to minimize the phase variation. The spin tune is then

$$|\nu_s(n)| = |\nu_s^{\text{fix}}| + \frac{1}{2\pi} \frac{d\tilde{\phi}(n)}{dn}. \tag{3.5}$$

[46]

A simpler algorithm based on discrete Fourier transformations was also developed at RWTH Aachen and Forschungszentrum Jülich [47].

4. Low Energy Polarimeter

4.1. LEP Detector Layout

One main goal of this thesis was to develop a new read-out system for the Low Energy Polarimeter (LEP). The old system, which was in use until 2015 had to be replaced because of its limited data rate and because some of the hardware was over twenty years old and no longer supported. It was replaced by a new system based on FPGAs.

The Low Energy Polarimeter (LEP) [39] is located in the injection beam line of COSY, behind the cyclotron and before the main ring. LEP measures the beam polarization at a kinetic energy of 45 MeV for protons and 75 MeV for deuterons.

Fig. 4.1 shows a photograph of LEP. The beam enters the polarimeter from the left hand side, the target is at the center. The target can be chosen using a movable target ladder; carbon and polyethylene (CH_2) were used for the experiments in this thesis. The target thickness is between 0.1 mm and 0.5 mm. For polarization measurements parallel to experiments at COSY, a carbon target is positioned in the upper edge of the beam while letting most of it pass.

The scattered particles are detected by plastic scintillator detectors with photomultiplier tubes for read-out. In total there are twelve detectors, three for each cardinal direction, left, right, up and down. These detectors are spaced 10° apart and can be moved forward and backward as a rigid group to select a scattering angle. The signals from all twelve detectors are preamplified and sent to the cyclotron control room over a distance of about 80 m. Originally, LEP was designed with one sodium iodide scintillator in each direction, which were replaced by the current detectors [39].

Fig. 4.2 shows a drawing of the detectors at one side of the polarimeter. The scintillators are 5 cm long, stopping all charged particles from the target. Collimators with a radius from 0.5 mm to 6 mm can be attached to the detectors to adjust the rate. The different radii can be chosen such that detectors at different scattering angles measure similar rated despite the greater differential cross-section at forward angles. For most measurements with the new read-out system, the collimators were removed.

The central vacuum chamber has eight exit windows made of 10 µm steel foils, through which particles pass before reaching the detectors. This limits the angular acceptance to a range of 25° to 70° in the forward exit windows and 110° to 155° in the backward windows.

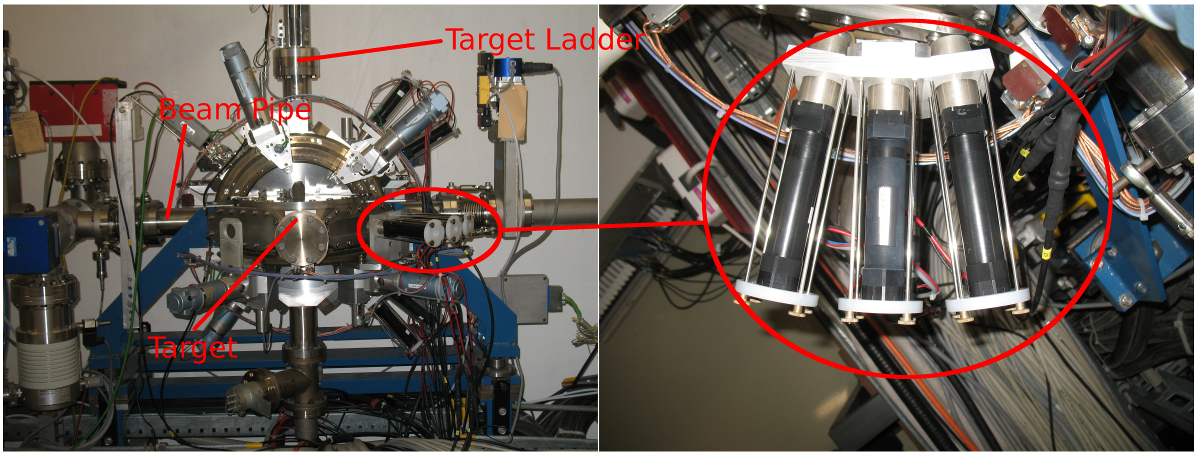

Figure 4.1.: Low Energy Polarimeter (left) and close-up of one set of detectors (right) [48].

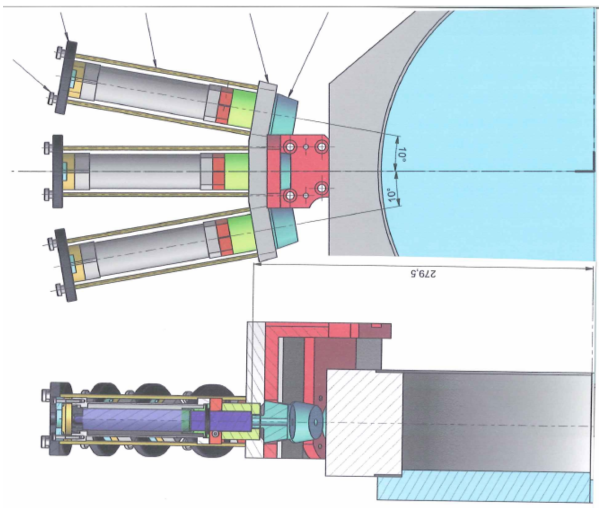

Figure 4.2.: Drawing of detectors.

4.2. Development of a Read-Out System for LEP

4.2.1. Old Read-Out System

The old, now decommissioned read-out system for LEP consisted of analog NIM modules. It was able to measure signal amplitude spectra, the rates of events within an adjustable amplitude window and kinematic coincidences of recoil and ejectile particles at different sides of the detector.

Fig. 4.3 shows the layout of the old read-out system. Each incoming signals is connected to a fan-out. One copy of the incoming signal is connected to an amplifier and then a multichannel analyzer to measure the amplitude spectrum. The other copy is sent to a discriminator converting the scintillator signals to logical pulses, which are counted to obtain the detector rates.

Coincidence measurements are performed using time to amplitude converters (TAC). Two detectors between which a kinematic coincidence is possible, such as the forward left detector (L3) and the backward right detector (R1), are connected to the start and stop inputs of a TAC. The resulting spectrum of times shows a clear peak corresponding to kinematic coincidence (fig. 4.4). The full width half maximum resolution is about 2.5 ns. Smaller peaks in the spectrum are random coincidences appearing every 38.5 ns. This time interval corresponds to the frequency of the cyclotron. The rate of coincidences is measured using a single channel analyzer integrated into the TAC.

The old read-out system was limited in a number of ways. The multichannel analyzer used to measure the pulse height spectrum required longer pulses than provided by the scintillators, which made a shaper-amplifier necessary, that limited the possible rate. To select elastic events, the discriminator thresholds had to be adjusted by hand using an oscilloscope. No data except the final rates were saved, making offline reanalysis impossible. Additionally, some parts of the hardware were over twenty years old and no longer supported.

4.2.2. New Read-Out Hardware

The new read-out consists of two so-called GANDALF modules originally developed for the COMPASS experiment [49]. Each module has an eight channel analog to digital converter (ADC) and an FPGA for signal processing, so that all functions of the old read-out can be implemented on a single device. The GANDALF board itself is a VME board containing the signal processing FPGA, the ADCs are mezzanine cards mounted on the main board. Other types of mezzanine cards are also available but not used here.

Each ADC has eight input channels with a sampling rate of 500 kHz at 12 bit resolution. The effective number of bits is above 10.1 over a wide frequency range [49, fig. 5]. A sampling rate of 1 GHz is achieved by interleaving two adjacent channels and alternately sampling the signal with two different ADCs. Therefore, there are effectively only four usable ADC channels on each mezzanine card, meaning eight channels per GANDALF module. The time resolution for pulses is in the order of 50 ps. Voltages in a range of 2 V can be measured. The baseline of each ADC channel can be adjusted using

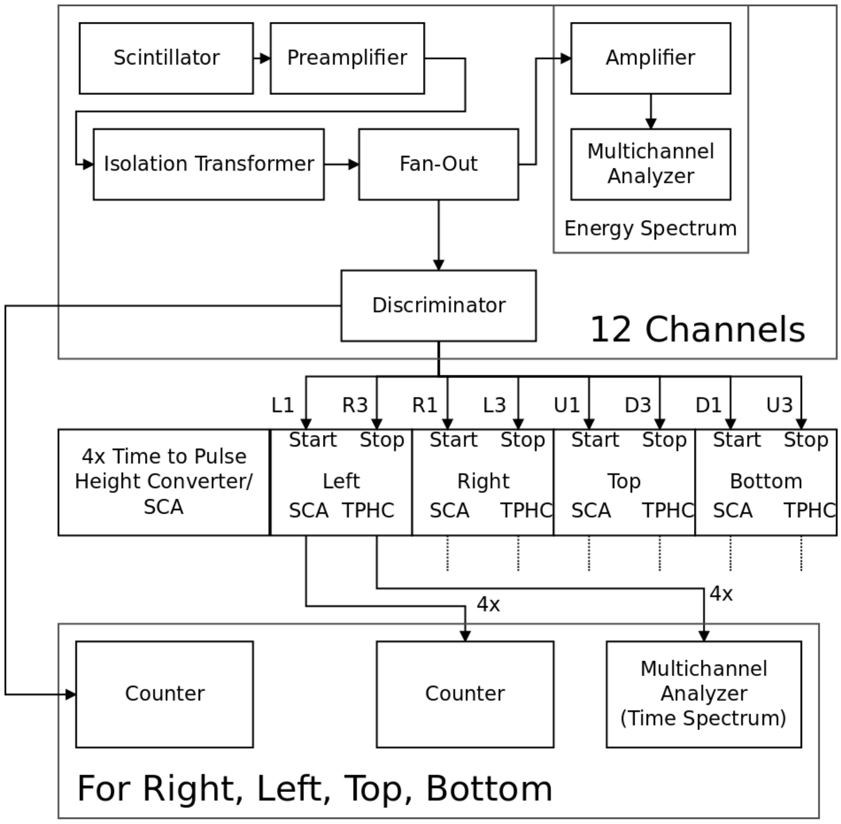

Figure 4.3.: Principle of the old read-out.

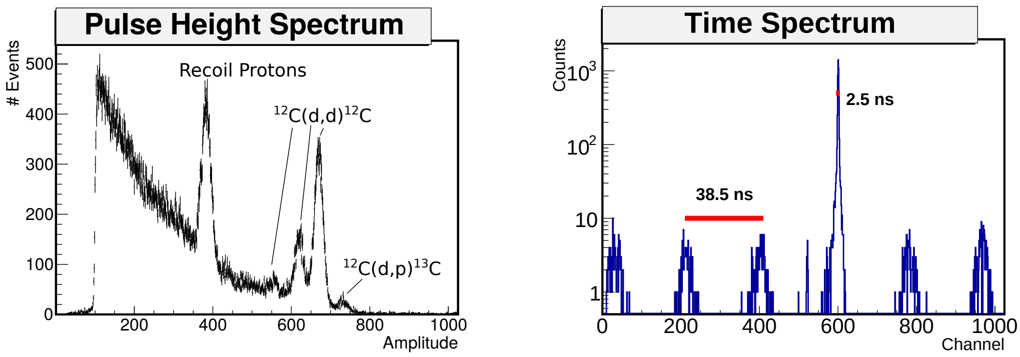

Figure 4.4.: Spectra of amplitudes and time differences measured with the old read-out system. The left plot shows an amplitude spectrum for deuterons scattered off a polyethylene (CH_2) target, the right plot shows the times between particles in kinematic coincidences.

a 16-bit digital to analog converter (DAC). Signals can be bipolar or unipolar depending on the DAC settings. [49]

Data transfer to a computer is possible over a link card on the back of the module, VME or a USB 2 port on the front panel. At LEP, GANDALF is used without a VME crate in a stand alone box that provides a power supply and cooling. The USB port is thus the only way to transfer both configuration and measurement data. The transfer rate is $20\,\mathrm{MB\,s^{-1}}$.

Two modules are necessary to measure the output of all twelve detector channels. One module is used for the channels in the vertical directions and one for the horizontal ones. This way, all possible kinematic coincidences occur between detectors connected to the same module.

The four bit signal showing the state of the polarized source is measured using a "Lab-Jack U12" USB data acquisition device. Fig. 4.5 shows the two GANDALF modules and the computer they are connected to in the cyclotron control room.

4.2.3. Firmware Overview

The main goal for the firmware development was to implement the functions of the old system on a single device: pulse height spectrum measurement, time measurement for coincident particles and counting events within an adjustable values for amplitude and time. In addition to these functions, the shapes of individual pulses can be recorded. It was found during test runs that the function used to measure the time between coincident particles can also be used to measure the time between cyclotron extraction and the detection of a particle. This facilitates a time of flight measurement, albeit at a poor resolution and with a constant unknown offset due to the unknown beam and signal run times.

All firmware was written in the hardware description language VHDL. A large part of the original source code developed for use at the COMPASS experiment could be reused, especially the Constant Fraction Discriminator algorithm used to determine the amplitude and time of each pulse (sec. 4.2.4) [50]. Functions that had to be added include self-triggering of read-out, checking whether events lie in an acceptable amplitude and time range, counting events and a new simpler output data format optimized for LEP data.

The pulse height (sec. 4.2.5) and coincidence (sec. 4.2.6) measurement firmware is designed both to count events on the board and to send event-by-event information to the USB interface. The former mode allows for a better use of the available data rate while the latter allows for inspection of the spectra. Event-by-event information can also be prescaled to conserve data rate. At the typical rates during the beam times unprescaled output of all event-by-event data was feasible in almost all situations. The output format and the rates are discussed in detail in sec. 4.2.8.

Figure 4.5.: New data acquisition system: Two GANDALF boards and the computer

4.2.4. Constant Fraction Discriminator

A constant fraction discriminator (CFD) is an electronic element that receives an analog pulse as input, for example from a photomultiplier, and generates a logic pulse if the input amplitude is sufficient. The difference from a normal discriminator is that the time of the output signal is independent from the amplitude of the input signal, which makes this method suitable for time measurements. The algorithm used here [50] also determines the amplitude of the input signal.

On an FPGA, the pulses are represented as a series of discrete voltage samples. The CFD algorithm works by inverting the polarity of the signal, delaying it, reducing the amplitude by a certain factor and adding the result to the original signal. The point where the resulting curve crosses the time axis is independent of the signal amplitude and can be used to measure the pulse time. A first, rough estimate of the time is the last point of the resulting curve is above zero. Linear interpolation between this point and the next one is used to obtain a more precise value. Fig. 4.19 shows a simulation of the algorithm applied to a measured pulse.

The amplitude of the signal is the estimated by the maximum sample in an adjustable range around the zero crossing.

The final output of the CFD is a 9-bit number for the amplitude and a 16-bit number for the time. The least significant time bin corresponds to about 17 ps, the least significant amplitude bin is about 3.9 mV.

4.2.5. Pulse Spectrum Measurement

The amplitude measurement is handled by the `SCA_counter` module in the code, so named because it acts as a single channel analyzer. The module receives the pulses found in the CFD as input. Additionally, a minimum and maximum amplitude can be set. Whenever a pulse is registered whose amplitude is within the given range, a counter is incremented and the pulse information is forwarded to the output buffer. One such module is generated for each ADC channel and all settings can be adjusted separately for each channel. The amplitude output can be prescaled to save data rate.

Table 4.1 shows an overview of the input and output ports. The `data_in` and `valid` port are directly connected to the CFD module of the corresponding channel. `data_in` contains the pulse information, `valid` is set to 1 when a pulse is found, indicating that the port `data_in` can be read now. The output uses a FIFO (first in first out) with a maximum length of 1024 events as a buffer, which is implemented using the RAM blocks on the FPGA. Output buffers are necessary because because all data has to be transmitted sequentially via USB. When several channels find pulses at once, some have to be delayed before being transmitted (see also section 4.2.8).

To select events, `SCA_counter` has to compare the amplitude of each incoming pulse to the minimum and maximum value. The FPGA on the GANDALF board provides so-called digital signal processing (DSP) slices, which can perform various operations more efficiently than the lookup tables and registers on the FPGA, including addition and subtraction. When one input port of a subtractor is connected to the pulse amplitude

Table 4.1.: Input and output ports for pulse spectrum measurement

Name	I/O	Width	Description
data_in	I	30 bit	Contains the time and amplitude information from the CFD
valid	I	1 bit	Is set when a pulse is registered in the CFD
min_amp	I	9 bit	Minimum amplitude
max_amp	I	9 bit	Maximum amplitude
prescaler_in	I	32 bit	If the prescaler is set to 0, all pulse information is send out. If it is set to n, the information for every $(n+1)$th event is written.
reset	I	1 bit	Resets the counter
clk	I	1 bit	Clock input for the main logic using a frequency of 200 MHz
fifo_data_out	O	30 bit	Buffered output data
fifo_empty	O	1 bit	On if the output FIFO is empty
fifo_ren	I	1 bit	Read enable for the output FIFO
fifo_read_clk	I	1 bit	Clock input for the output buffer (see below) also 200 MHz
count	O	24 bit	Number of registered events in range

and the other is connected to the signal for the minimum or maximum amplitude, the carry bit of the subtractor shows which one is larger, allowing for an efficient comparison. If the conditions `amp` > `min_amp` and `amp` < `max_amp` are both fulfilled, the input pulse information is written to the output FIFO and the counter is incremented.

The comparison operation has a latency of two clock cycles. By the time the comparison is finished, the state of `data_in` might not be the same as when it started. A shift register with a length of two is used to delay the pulse information, keeping it synchronized with the subtractor output. When the comparison is finished, the correct pulse data can be found at the end of the shift register.

4.2.6. Coincidence and Time of Flight Measurement

A method for identifying coincident pulses was implemented in the `kinematic_selector` hardware module. Although the original plan was to identify pairs of coincident particles on the FPGA, the module was later adapted to measure the time between a maximum in the cyclotron rf voltage and the arrival of a particle, which is closely related to the time of flight.

The cyclotron operates at a frequency of 27.4 MHz for deuterons. The particles are extracted when the cyclotron voltage is at a certain phase. They then travel on to the polarimeter in a constant amount of time. After the particles are scattered, their kinetic energy and therefore the time they take from the target to the detector can vary. The measured time difference is equal to the variable time of flight between target and detector plus a constant offset from the delays in the beam line and the signal cables.

Coincidences can still be identified in an offline analysis by finding particles whose difference in time of flight matches the expectation. The measurement as originally planned should still be possible with the new firmware but was not attempted during the beam times as it provides less information than the time of flight technique.

Table 4.2.: Input and output ports for coincidence and time of flight measurement

Name	I/O	Width	Description
`start_data_in`	I	30 bit	Time and amplitude for the start channel
`start_valid`	I	1 bit	Is set when a pulse is registered at the start channel
`stop_data_in`	I	30 bit	Time and amplitude for the stop channel
`stop_valid`	I	1 bit	Is set when a pulse is registered at the stop channel
`min_start_amp`	I	9 bit	Minimum start amplitude
`max_start_amp`	I	9 bit	Maximum start amplitude
`min_stop_amp`	I	9 bit	Minimum stop amplitude
`max_stop_amp`	I	9 bit	Maximum stop amplitude
`min_diff_time`	I	16 bit	Minimum time difference
`max_diff_time`	I	16 bit	Maximum time difference
`max_count`	I	6 bit	Number of cycles after which the “start found” state reverts to “idle”
`prescaler_in`	I	32 bit	If the prescaler is set to 0, all pulse information is send out. If it is set to n, the information for every $(n+1)$th event is written.
`count_matches`	O	24 bit	Number of registered events in range
`reset`	I	1 bit	Resets the counter
`clk`	I	1 bit	Clock input for the main logic using a frequency of 200 MHz
`fifo_data_out`	O	30 bit	Buffered output data
`fifo_empty`	O	1 bit	On if the output FIFO is empty
`fifo_ren`	I	1 bit	Read enable for the output FIFO
`fifo_read_clk`	I	1 bit	Clock input for the output buffer (see below) also 200 MHz

The module takes the pulse information from two ADC channels as input, henceforth referred to as the start and stop channel. In time of flight measurements, the start channel is connected to the cyclotron rf signal and the stop channel is connected to one of the LEP detectors. In a coincidence measurement, the start channel would be the channel on which the first of two coincident particles is expected. Both the start and the stop pulse must be within an adjustable amplitude range. The time between the start and stop pulse must also be within an adjustable range.

The first step in a time measurement is to check the pulse amplitudes for the start and stop channel. This is done using DSP slices as explained in section 4.2.5. The time difference is tested after that, considering only those pulses that meet the amplitude condition.

Testing the time difference is more complicated than testing the amplitude as the start and stop signals can arrive in different clock cycles. The delay between the start and stop data can vary, making it difficult to compensate using shift registers. Additionally, there can be several stop signals for one start signal, for example when two particles are detected in the same cyclotron period. Checking the time difference takes four clock cycles, two for subtracting the start and stop time and two for comparing the result to the minimum and maximum value. Keeping the electronics unresponsive for multiple clock cycles of 4 ns each would lead to significant dead times compared to the cyclotron period of 38.5 ns. To avoid such dead times and to handle several events per cyclotron turn, the electronics must be able to process several potential pairs of pulses in parallel.

These problems are solved using a separate module called `DT_checker` that calculates the time difference between two pulses and compares it to the minimum and maximum values. Several such modules exist for each pair of start and stop channels; each of the parallel instances can compare one stop pulse to the start pulse from the cyclotron. The precise number of instances, which is equal to the number of pulses that can be handled at the same time, can be adjusted in the code and was set to 10.

`DT_checker` is implemented as a finite state machine (FSM) (fig. 4.6). A finite state machine is a virtual automaton that is in one of a finite number of states at any time and changes between these states depending on input. `DT_checker` can be in an "idle" state, waiting for a start pulse, in a "start found" state, in which a start pulse has been registered but the stop pulse has not arrived yet, and in a "compare" state, in which both pulses have been detected and are being processed.

In addition to the input ports for the start and stop pulse data, `DT_checker` has an "active" input. It only responds to stop signals when "active" is set to one. At any given time the `kinematic_selector` module sets the "active" input of the first `DT_checker` that is not in the "compare" state to 1 and all others to 0. This ensures that the stop pulse is only used once and that it is handled by a free instance of `DT_checker`.

All instances of `DT_checker` are initially in the "idle" state. When a start pulse is registered, the FSM saves the data of that pulse and switches to the "start found" state. When the active `DT_checker` receives a stop signal it changes from "start found" to "compare" and remains in this state until the time difference has been calculated and compared to the minimum and maximum value. If the time difference is in the right range, the counter of the `kinematic_selector` is incremented and the data for the start and stop pulse are sent to the computer. If the start and stop pulse arrive in the same clock period, a direct transition from "idle" to "compare" is possible.

If another start pulse arrives in the "start found" state, it replaces the old start pulse data. After an adjustable number of clock cycles in the "start found" state, the FSM reverts to "idle". This number was set higher than the duration of one cyclotron turn so that the electronics only completely revert to the initial state if the signal is lost.

Like the pulse height measurement, the time of flight measurement has an optional prescaler to manage the data rate.

Fig. 4.7 shows an example of pulses being processed. The initial start pulse arrives

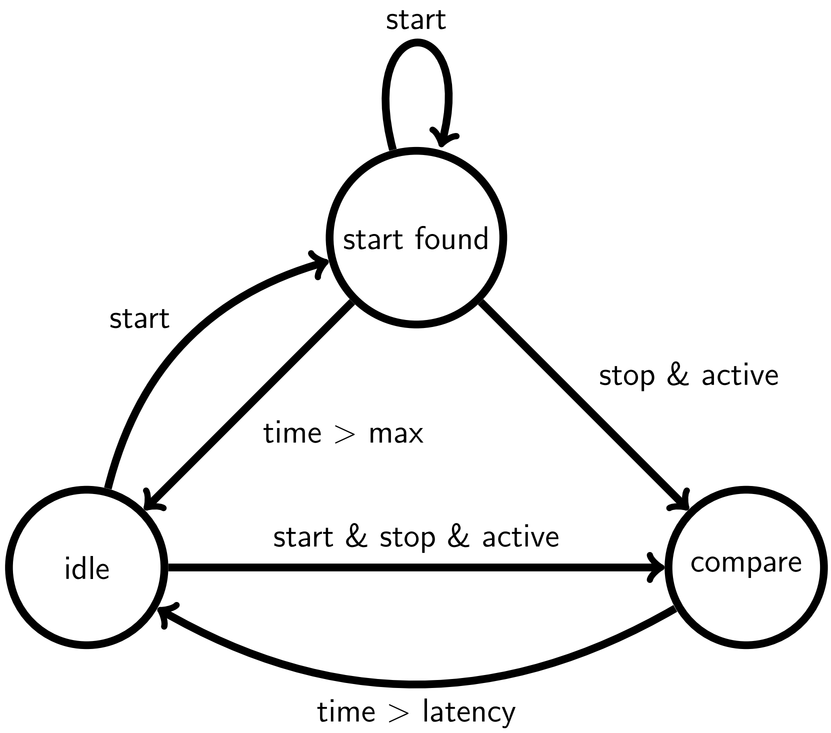

Figure 4.6.: Finite state machine used to measure the time of flight or coincidence.

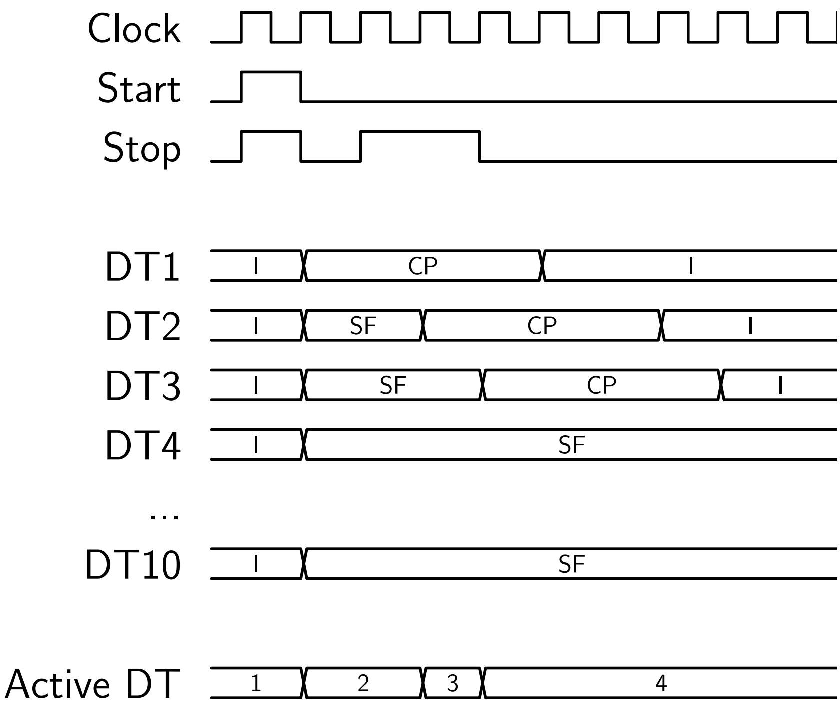

Figure 4.7.: Example of three pulses being processed in an instance of `kinematic_selector`. The abbreviations I, SF and C stand for "idle", "start found" and "compare".

simultaneously with a stop pulse. The first instance of `DT_checker` is initially active and switches to the "compare" state to processes these two pulses. The other instance switch to the "start found" state and wait for more stop pulses. When the second stop pulse arrives, the second `DT_checker` is active and switches to "compare". This pattern continues for further pulses.

Similar to the pulse spectrum measurement, the output uses a FIFO buffer with a depth of 1024 events.

4.2.7. Pulse Shape Measurement

The final function that was added to the firmware is a pulse shape measurement, which sends the complete wave form of an input pulse to the computer, like an oscilloscope. While the pulse spectrum and coincidence measurements only use the output data of the constant fraction discriminator, the pulse shape consists of raw ADC data.

The module for pulse shape measurement is called `wave_buffer`, as its main part is a ring buffer that contains the input voltage samples. This buffer is necessary because a pulse is already over when the CFD has registered it as a pulse. Therefore the electronics has to keep the samples in memory so data from before the trigger can be transferred to the computer.

Table 4.3.: Input and output ports for pulse shape measurement

Name	I/O	Width	Description
`data_i_r`	I	24 bit	Input data from one ADC
`data_i_l`	I	24 bit	Input data from other ADC
`wrclk`	I	1 bit	Write clock, 250 MHz
`rdclk`	I	1 bit	Read clock, 200 MHz
`prescaler_in`	I	32 bit	If the prescaler is set to 0, all pulse information is send out. If it is set to n, the information for every $(n+1)$th event is written.
`pulse_length`	I	9 bit	Length of the pulse in units of four samples
`read_write_delay`	I	9 bit	Number of samples taken before the trigger signal in units of four samples
`get_pulse`	I	1 bit	Signal that buffer content should be read out
`writing_pulse`	O	1 bit	Set to 1 when a pulse is being written from the buffer to the output fifo
`reset`	I	1 bit	Resets the memory
`fifo_data_out`	O	48 bit	Output data
`fifo_empty`	O	1 bit	On if the output FIFO is empty
`fifo_ren`	I	1 bit	Read enable for the output FIFO

Table 4.3 shows an overview of the input and output ports. As already mentioned in section 4.2.2, the sampling rate of 1 MHz is achieved by interleaving the read-out of

two ADCs. Each ADC is operated at a frequency of 250 MHz with double data rate, meaning that a sample is taken on the rising and on the falling edge of the clock signal.

To handle all samples in real time, the firmware must process four samples in each 250 MHz clock cycle. The input ports `data_i_r` and `data_i_l` each contain two samples from one ADC. Chronologically, the first sample is the bits from 11 down to 0 of `data_i_r`, the second sample is the bits from 11 down to 0 of `data_i_l`, the third sample is the remaining bits of `data_i_r` and the last sample is the remaining bits of `data_i_l`.

The main buffer is implemented using the integrated RAM blocks of the FPGA. The firmware keeps track of a read address and a write address on the buffer. Each `wrclk` cycle, four samples are written to the buffer at the write address, and the write address is incremented so that the next samples are written to the following memory block in the next cycle. The read address is also incremented each cycle and always remains at a distance of `read_write_delay` to the write address. When either address reaches the end of the buffer memory, it returns to the start. This way, the wave form can be retrieved by reading `pulse_length` data words starting from the read address.

Unlike the previous hardware modules, `wave_buffer` uses two different clocks, one writing clock at 250 MHz and on reading clock at 200 MHz. The ADCs and the buffer writing operations are synchronized to the faster writing clock. The CFDs and the USB readout are synchronized to the reading clock.

Whenever one of the CFDs registers a pulse, the `get_pulse` bit is set and firmware writes data from the read address of the buffer to the output FIFO for `pulse_length` cycles of the writing clock. This data can then be read from the FIFO at the slower reading clock speed and the sent on to the computer.

The `wave_buffer` on ADC channel seven is exceptional as it is connected to the cyclotron rf signal and not to a detector. It is not triggered by the signal on its own channel, but whenever one of the other `wave_buffer` modules is triggered. This way each pulse can be viewed relative to the cyclotron signal, for example to verify the time of flight measurements.

4.2.8. Data Output

The purpose of the data output process is to turn the measurement results into a single stream of data that can be sent to the computer. All hardware modules described in the previous sections write their outputs independently to a buffer. However, the data transfer to the computer uses 32-bit words that are sent sequentially.

Data can arrive from several channels at once. It is also possible for new data to arrive while other data is being sent. The output process has to schedule the data from the different modules and convert them into a consistent format. Table 4.4 shows the data format used for the different kinds of measurement.

The first two bits in all data types are a counter that increments after each word. This counter can be used to verify that no data is lost in transmission. If the hardware is running correctly, all data words received by the computer are consecutively numbered. If some data words are lost, for example because the detector rate is greater than the

Table 4.4.: Data format

<table>
<tr><td colspan="6">Amplitude Spectrum</td></tr>
<tr><td>31-30</td><td>29-28</td><td>27-25</td><td colspan="2">24-9</td><td>8-0</td></tr>
<tr><td>Word No.</td><td><code>00</code></td><td>Channel</td><td colspan="2">Time</td><td>Amp</td></tr>
<tr><td colspan="6">Coincidence Start</td></tr>
<tr><td>31-30</td><td>29-28</td><td>27-25</td><td colspan="2">24-9</td><td>8-0</td></tr>
<tr><td>Word No.</td><td><code>01</code></td><td><code>111</code></td><td colspan="2">Time</td><td>Amp</td></tr>
<tr><td colspan="6">Coincidence Stop</td></tr>
<tr><td>31-30</td><td>29-28</td><td>27-25</td><td colspan="2">24-9</td><td>8-0</td></tr>
<tr><td>Word No.</td><td><code>01</code></td><td>Channel</td><td colspan="2">Time</td><td>Amp</td></tr>
<tr><td colspan="6">Wave Form</td></tr>
<tr><td>31-30</td><td>29-28</td><td>27-25</td><td>24</td><td>23-12</td><td>11-0</td></tr>
<tr><td>Word No.</td><td><code>11</code></td><td>Channel</td><td>Last Word</td><td>Sample</td><td>Sample</td></tr>
<tr><td colspan="6">Counter</td></tr>
<tr><td>31-30</td><td>29-28</td><td>27-25</td><td>24</td><td colspan="2">23-0</td></tr>
<tr><td>Word No.</td><td><code>10</code></td><td>Channel</td><td>Coinc</td><td colspan="2">Counter Value</td></tr>
</table>

maximum transfer rate and the output buffer overflows, the received words can be out of sequence.

The next two bits specify the type of measurement the data word represents. `00` stands for amplitude measurements, `01` for coincidence measurements, `10` stand for counter values and `11` stands for wave form data.

The three bits after that encode the channel number, which goes from zero to seven.

The remaining 25 bits are used in different ways depending on the data type.

Amplitude spectrum data are the simplest case, as one event can be described in a single data word. 16 bits are used for the event time, 9 bits for the amplitude.

The values of the counters on the FPGA can also be transferred using one word for each channel. These counter values are sent to the computer in regular intervals, which can be adjusted in the configuration.

Coincidence and time measurements need two data words per event, one each for the start and the stop pulse. The word belonging to the start pulse is marked by setting the channel number bits to `111`, which corresponds to the number 7. This number cannot otherwise occur in time measurements because there can only be up to seven instances of `kinematic_selector`, which would be numbered 0 through 6.

Wave form data can take an arbitrary number of words per event depending on the pulse length set in the configuration. Each word contains two samples. The samples are sent to the computer sequentially. Bit number 24 is set to `1` for the last word to indicate that the pulse is finished and that subsequent data words belong to a different event.

The output process is implemented as a finite state machine (fig. 4.8). The finite state machine waits in an "idle" state as long as the output FIFOs of all modules are empty. If data is found in one of the modules, the process goes to the corresponding

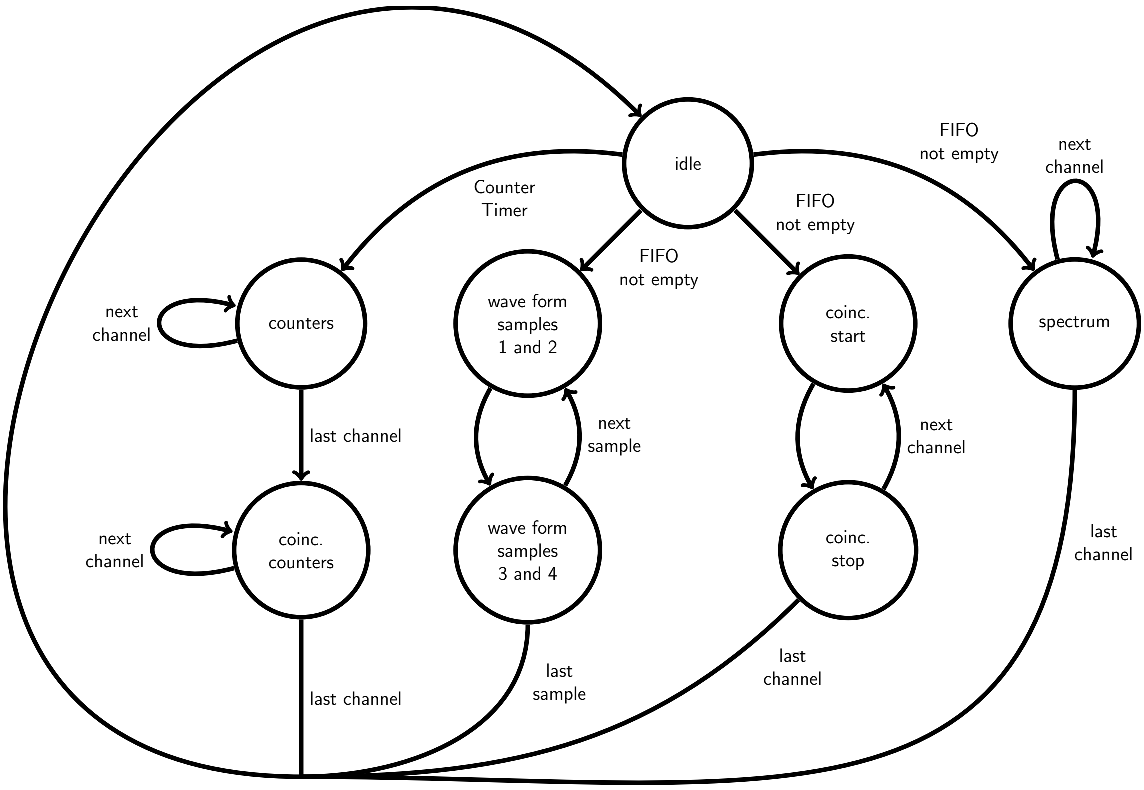

Figure 4.8.: Finite state machine used for data output.

state. If multiple modules deliver data, they are prioritized from left to right as shown in fig. 4.8.

When it is in the “idle” state, the state machine checks the timer for transmitting the counters to the computer in every clock cycle. If the timer has expired, the state machine switches to a state for transmitting the counters for the amplitude spectrum measurement. It remains in this state for eight clock cycles, transmitting the state of the counter for one ADC channel in each cycle. Afterward, the same procedure is repeated for the coincidence counters.

Wave form data is transferred sequentially at two samples per data word. Due to the interleaved measurement of two ADCs and double data rate, there are four samples per clock cycle and input channel. The state machine alternates between two states, “wave form samples 1 and 2” and “wave form samples 3 and 4”. In the former state the four samples are read parallelly from the `wave_buffer` output FIFO. Two of the samples are sent in the same cycle, the other samples are sent in the next cycle, when the process is in the “wave form samples 3 and 4” state. This is repeated until the output buffer is empty. In the final data word, bit 24 is set to `1` to indicate that the pulse is finished.

When one of the `kinematic_selector` modules delivers a data, the finite state machine iterates over all such modules, going through one cycle of the state “coinc. start” and “coinc. stop” for each module. If a module has data in its output buffer, it is sent to the computer. Pulse spectrum data is treated the same way, except that it only takes one cycle per channel.

This method is less efficient than going immediately to the first module with data in it. However, it has the advantage that no channel is treated differently from the others. If the program went directly to the first module with data, the first modules to be checked would be checked more often than the later ones. If the read-out system was operated at excessive rates, the data lost due to buffer overflows would be disproportionally from the channels checked later in the loop. In an experiment that measures asymmetry between the different channels to determine the polarization such behavior is unacceptable. The loss in efficiency is negligible, because the bottleneck in transfer speed comes after the output process, when the data is buffered one more time before being sent to the USB port.

4.2.9. Data Acquisition Software

The data acquisition software was written in python [51]. The ROOT framework [52] was used to store and analyze the data.

The DAQ software consists of several different programs: the python module `nepol`, which contains recurring functions to handle the raw data from the USB connection, the script `nepolread` that is used to take data and the script `nepolSpectrumViewer` that remotely monitors the spectra and rate asymmetries.

The `nepol` module provides a variety functions to extract variables from the 32-bit words from the FPGA, such as the type of data, the amplitudes and times of a given event, the samples in a pulse shape measurement or the state of the 2-bit counter that checks for lost data words. There are also functions for converting a histogram to a string that can be sent via MQTT and for calculating rate asymmetries along with their statistical errors.

Apart from that, the `nepol` module contains the class `treeWrapper`, which takes the raw data from one GANDALF module, converts it to normal variables, and writes the result to a ROOT tree [53, chapter 14]. One tree is used for each type of data: amplitudes, coincidence/time of flight, counters and wave form measurements. Each data word is assigned to one of the types based on the value of bits 29 and 28. Spectrum and counter data are written to the hard drive immediately on reception. For coincidence data, start and stop information is written after both have arrived. Pulse shape data is saved once the stop bit is found. The tree `treeWrapper` class also keeps track of value of the counter on bits 31 and 30. If the arriving data words are not sequentially numbered, an error message is sent to the console, because this indicates that some data is lost in transmission. Lost words are normally due to the firmware writing more data to the read-out buffer than the USB connection can transmit.

The class `multiTreeWrapper` handles an arbitrary number of `treeWrapper` instances simultaneously, while each instance processes the data from one GANDALF module. No more than two modules at a time were used in any measurement in this thesis, but the software could in principle handle any number. `multiTreeWrapper` also creates the strings that are sent via MQTT, containing the current polarization, the unix time and an amplitude spectrum for each cardinal direction. Whenever it receives counter data, `multiTreeWrapper` checks whether the values have increased since the last counter output. If there is no change between the current and the previous counter state, but change between that state and the one before, this means that the last pulse of beam from the cyclotron has ended.

The main part of the DAQ is the program `nepolread`, which is executed to start a measurement. `nepolread` was loosely adapted from a preexisting read-out script provided by the university of Freiburg. Because processes for USB and network connections often spend time waiting for input, the read-out is designed as a multithread program to prevent the different functions from blocking each other. Fig. 4.9 shows the program structure. One thread reads the data from the USB ports and writes them to a queue. Another thread gets the polarization state from the LabJack module at the maximum possible speed and writes it to a shared variable. A third tread sends MQTT messages and handles the connection to the broker.

All of these threads interact with one main tread that combines the information from the other ones and generates the output. This thread reads the queue with the raw data and feeds each word into the aforementioned `multiTreeWrapper` class to write them to the hard drive. If the `multiTreeWrapper` detects the end of a 20 ms beam pulse, an MQTT message is generated and written to a queue, from which the MQTT thread retrieves it and sends it to the broker. The histograms and event counts in the MQTT messages are incremental, including only the data that has been taken since the last message. If no pulses are found for 20 s, the program sends an MQTT message containing empty histograms and zero events counted. This verifies that the DAQ is still running and helps to distinguish DAQ problems from other issues like a loss of the beam.

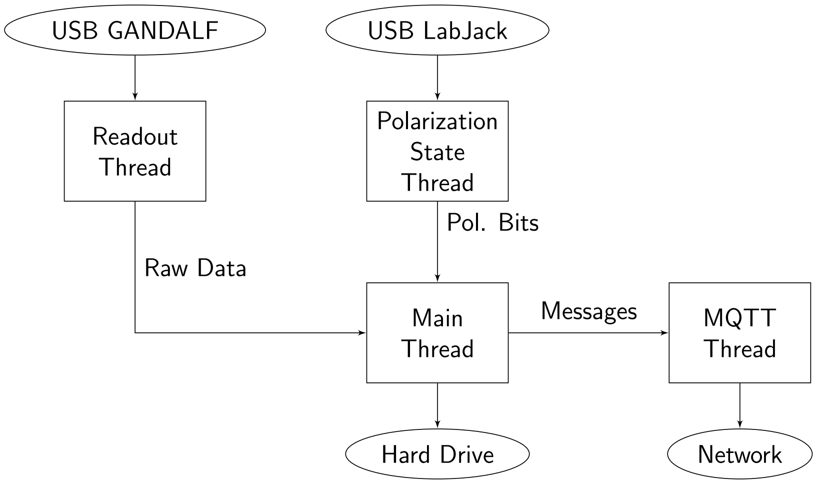

Figure 4.9.: Structure of threads in `nepolread`

The MQTT messages can be received using the program `nepolSpectrumViewer`. All amplitude spectra in the message are converted back into ROOT histograms and added up on the client side. The results are displayed on screen in a separate window and updated whenever a new message arrives. In the graphical interface (fig 4.10), the user can specify a polarization state to view. For each direction and polarization state, a minimum and maximum amplitude can be entered to specify the position of the peak used for polarimetery. Two methods for estimating the peak content are available: a simple integration of the bins in range, and a Gaussian fit with or without a linear background.

In a third window, the program displays the asymmetries and detector rates over an adjustable time range for each polarization state to show possible instabilities.

The GUI also has a button to pause and resume the updates of the spectra, which can be used to examine them more closely without interruption from updates. As the spectra are displayed in a ROOT window, the usual functions for viewing and manual fitting can be used.

On closing the program, the settings and integrated histograms are saved automatically and loaded when the program is started again. The data in the histogram can be reset manually using a button on the interface.

The software also includes a simple analysis script called `analyze`, which can generate spectra and plots of the rate asymmetries over time from the trees created by `nepolread`. Fig. 4.11 shows a typical graph generated by the script. The script is controlled using a configuration file following the ini format. A start and stop time can be specified to limit the analysis to a specific range, which reduces the required computation time as the program does not have to iterate over the complete file, which can reach tens of gigabytes in size over a few days. Other settings include minimum and maximum amplitudes and the hardware channel numbers connected to the different directions.

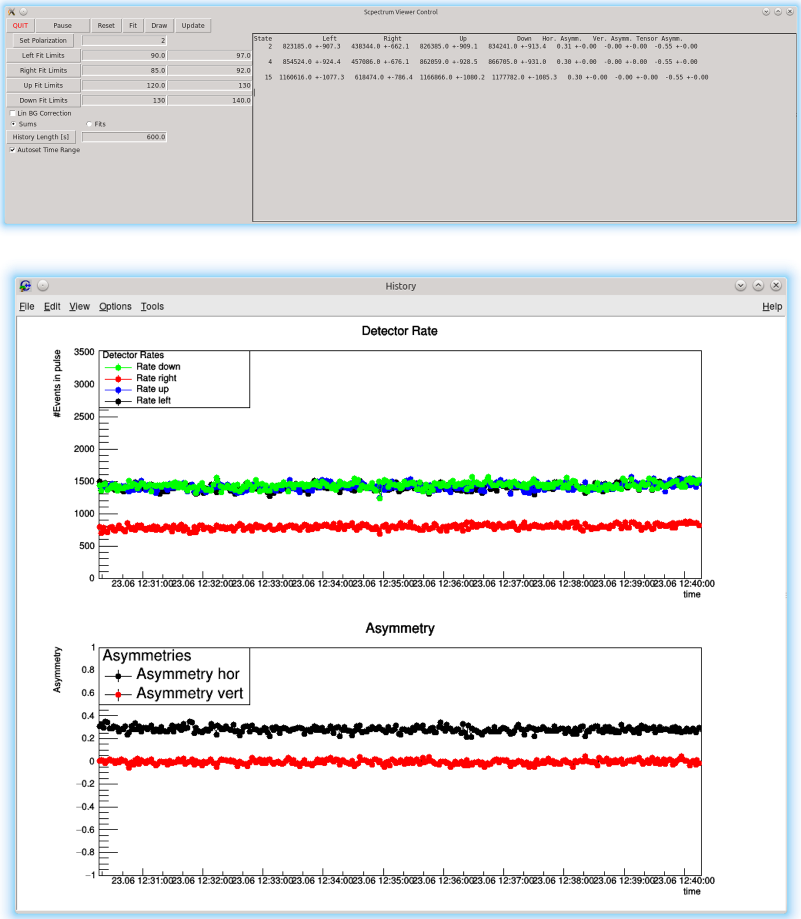

Figure 4.10.: Graphical interface of `nepolSpectrumViewer` (top) and monitor window (bottom)

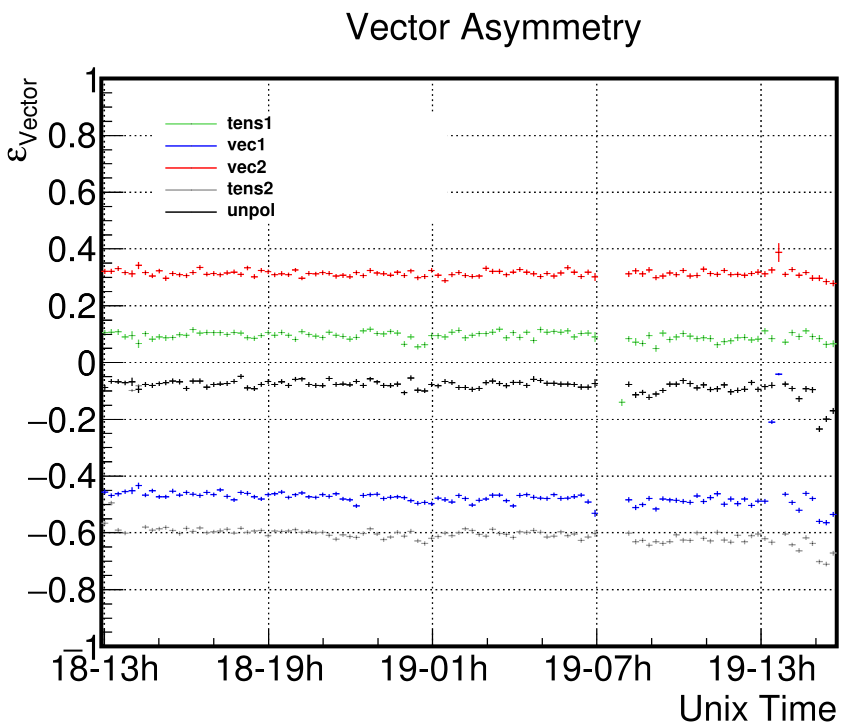

Figure 4.11.: Graph of asymmetries over time generated by analysis script

4.3. Measurements

4.3.1. General

The first version of the new read-out electronics was tested during the beam time of summer 2015 [48]. It has since become the routine tool for calibrating the polarized particle source during machine development.

Amplitude and time of flight measurements were taken for a deuteron beam on a carbon target at different angles, a deuteron beam on a polyethylene target at kinematic coincidence and a proton beam on a carbon target. The selection of elastic events was performed using only the amplitude information as signal and background were not well separated in time of flight. It is possible to distinguish between outgoing protons and deuterons using time of flight information (sec. 4.3.3). However, the method is not very robust and has little advantage over an analysis using only amplitude data.

4.3.2. Amplitude and Time of Flight Spectra

Fig. 4.12 show a typical amplitude spectrum for deuteron carbon scattering at 40°. A deuteron beam incident on a carbon target can cause several different reactions. The most useful reaction for polarimetery is elastic scattering, which is visible in the spectra as the single largest peak. The carbon nucleus has several excited states that are visible to varying extends. One state at 4.4 MeV is clearly visible in most measurements. As

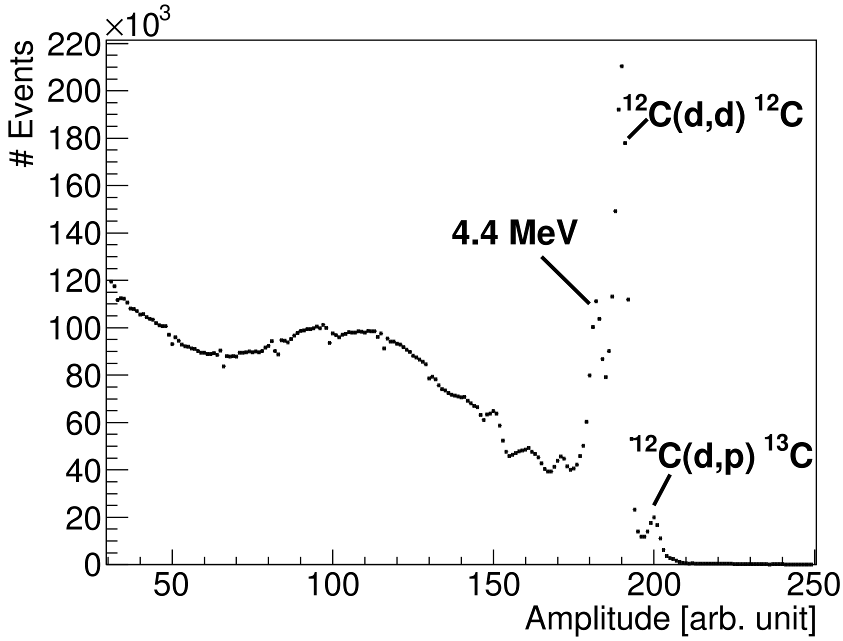

Figure 4.12.: Typical amplitude spectrum for deuteron carbon scattering at 40°, which is the marginal distribution of the data in fig. 4.13.

the binding energy of a deuteron is only 2.2 MeV, deuterons can break up into protons and neutrons when hitting the target, leading to a wide, continuous distribution of amplitudes. Finally, a deuteron can lose its neutron to the target nucleus in the reaction ^{12}C(d,p)^{13}C. As this reaction has only two outgoing particles, all outgoing protons at a given angle have the same energy. In the spectrum, it is visible as a peak at slightly higher amplitudes than elastic scattering.

Fig. 4.13 shows a two-dimensional plot of the time of flight and the amplitude for the same data as fig. 4.12. Under ideal circumstances, one would expect the time of flight to be a function of the amplitude for every type of outgoing particle. As the kinetic energies of the particles are small compared to their rest masses, the first order dependency is

$$\Delta t = \frac{s}{v} + t_0 \approx s\sqrt{\frac{2m}{E_{\mathrm{kin}}}} + t_0, \tag{4.1}$$

where $s \approx 20\,\mathrm{cm}$ is the distance from the target to the detector, t_0 is a constant offset due to run times of the beam and measured signals, m is the mass of the particle and E_{kin} is its kinetic energy.

In fig. 4.13, the observed time decreases with amplitude for amplitudes smaller than 100 and then increases again. This is an unphysical effect probably due to imperfections in the CFD algorithm causing the time to depend on the pulse amplitude. For the analysis in section 4.3.3, this is no problem as the time distribution is examined separately for each amplitude bin and not compared between different amplitudes.

Although the read-out electronics can measure time to a precision in the order of 50 ps, the distribution of the time of flight is smeared out over several nanoseconds. This is due

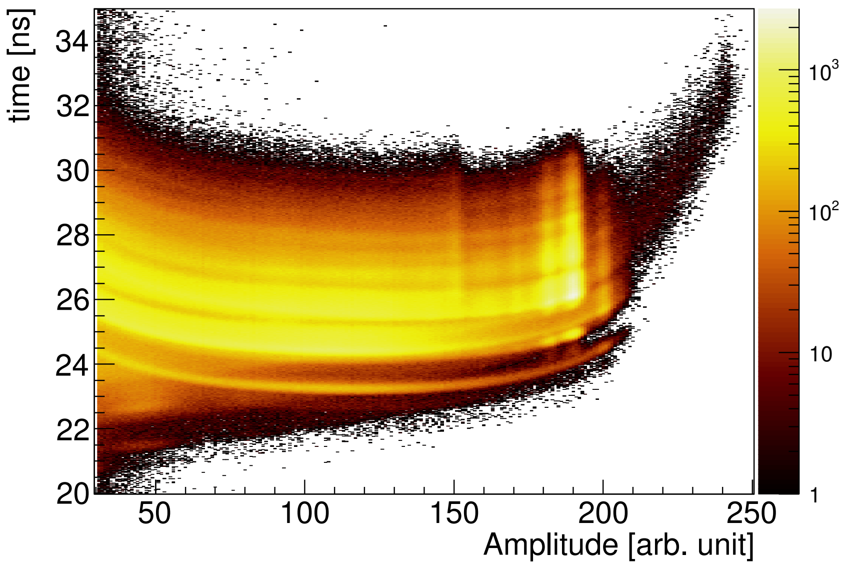

Figure 4.13.: Amplitude and time of flight spectrum for the same measurement as fig 4.12

to the so-called multiturn extraction in the cyclotron. Particles are not only extracted from the outermost turn of the spiral-shaped trajectory inside the cyclotron but from several turns. This causes a spread of the times at which particles arrive at the target relative to the cyclotron rf signal that is used to measure the time. Sec. 4.3.3 deals with a method to distinguish different types of particles despite this broadening effect.

Fig. 4.14 shows the results of a measurement of deuterons scattered off a polyethylene target. The scattering angles of 25.9° for the inner detector and 45.9°, where kinematic coincidences can be observed. The coincidences were identified offline by finding pairs of events at the appropriate channels that were measured during the same cyclotron period. The coincidence measurement leads to an almost background free spectrum.

4.3.3. Analysis of Time of Flight Spectra

Despite the broadening of the time of flight distributions due to multiturn extraction it is possible to obtain the number of protons and deuterons at a given amplitude. Assuming only two types of particles interacting with the detector, protons and deuterons, the time of flight distribution at a given amplitude can be described as

$$f_A(t) = [N_1\delta(t - t_1) + N_2\delta(t - t_2)] * g(t), \tag{4.2}$$

neglecting the limited amplitude resolution. The $*$ symbol stands for convolution, $t_{1,2}$ is the time at which the particles are detected, $N_{1,2}$ is their number and δ is the Dirac distribution. g is the longitudinal profile of the cyclotron pulse, i.e. the distribution of times that would be measured by holding a detector directly into the beam. The convolution can be trivially evaluated.

$$f_A(t) = N_1 g(t - t_1) + N_2 g(t - t_2) \tag{4.3}$$

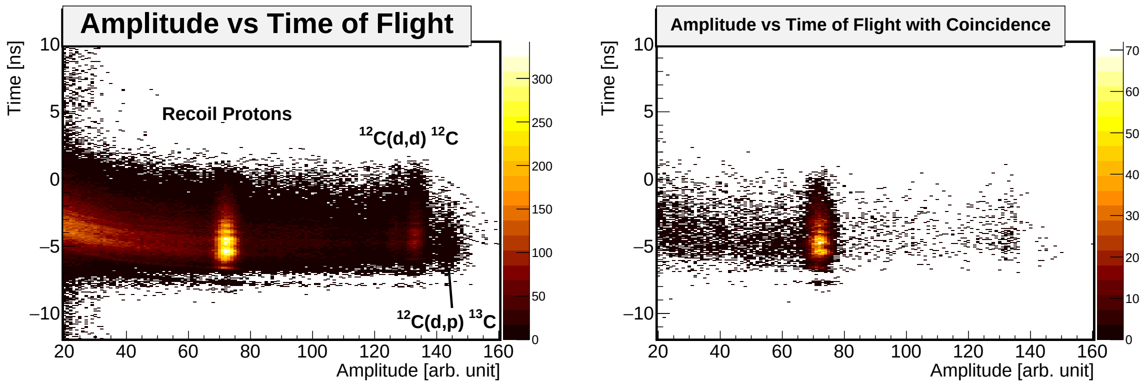

Figure 4.14.: Amplitude and time of flight spectra for a coincident measurement of deuterons scattered off a CH_2-target, using either all events or only coincident ones [48].

If g is known this function can be fitted to the time of flight distribution for every amplitude bin to find $t_{1,2}$ and $N_{1,2}$.

g is a complicated, multimodal distribution that changed between measurements and does not resemble any simple mathematical function. It can be estimated from data using the ^{12}C(d,p)^{13}C peak in the spectra. This peak has the highest amplitude of all processes and is therefore very pure. The empirical distribution of t for events with amplitudes in this peaks is proportional to g as only one of the Ns in (4.2) is nonzero. An adaptive kernel density estimator [54, 55][52, class "TKDE"] is used to estimate g in fits.

Given a sample of measured times $t_1 ... t_n$ and a kernel function K, the kernel density estimator is defined as

$$g(t) = \frac{1}{n} \sum_{i=1}^{n} \frac{1}{h_i} K\left(\frac{t - t_i}{h_i}\right), \tag{4.4}$$

where h_i is a weighting parameter that is computed for each event as

$$h_i = \rho \left(\frac{4}{3}\right)^{1/5} \sqrt{\frac{\sigma}{g_0(t_i)}} n^{-1/5}. \tag{4.5}$$

σ is the standard deviation of the data and g_0 is another kernel density estimator with h fixed to 1 time channel. The choice of the fixed h in g_0 has almost no influence on the final result [54]. ρ was set to 0.02, K is a normal distribution around zero with a standard deviation of 1. For some measurements with lower statistics, increasing ρ to 0.05 improved the results.

Fig. 4.15 shows examples of the time of flight distribution for ^{12}C(d,p)^{13}C and the corresponding kernel density estimators. The kernel density estimators are smoother than interpolated histograms, which is helpful for fitting as it makes the χ^2-function smooth as well.

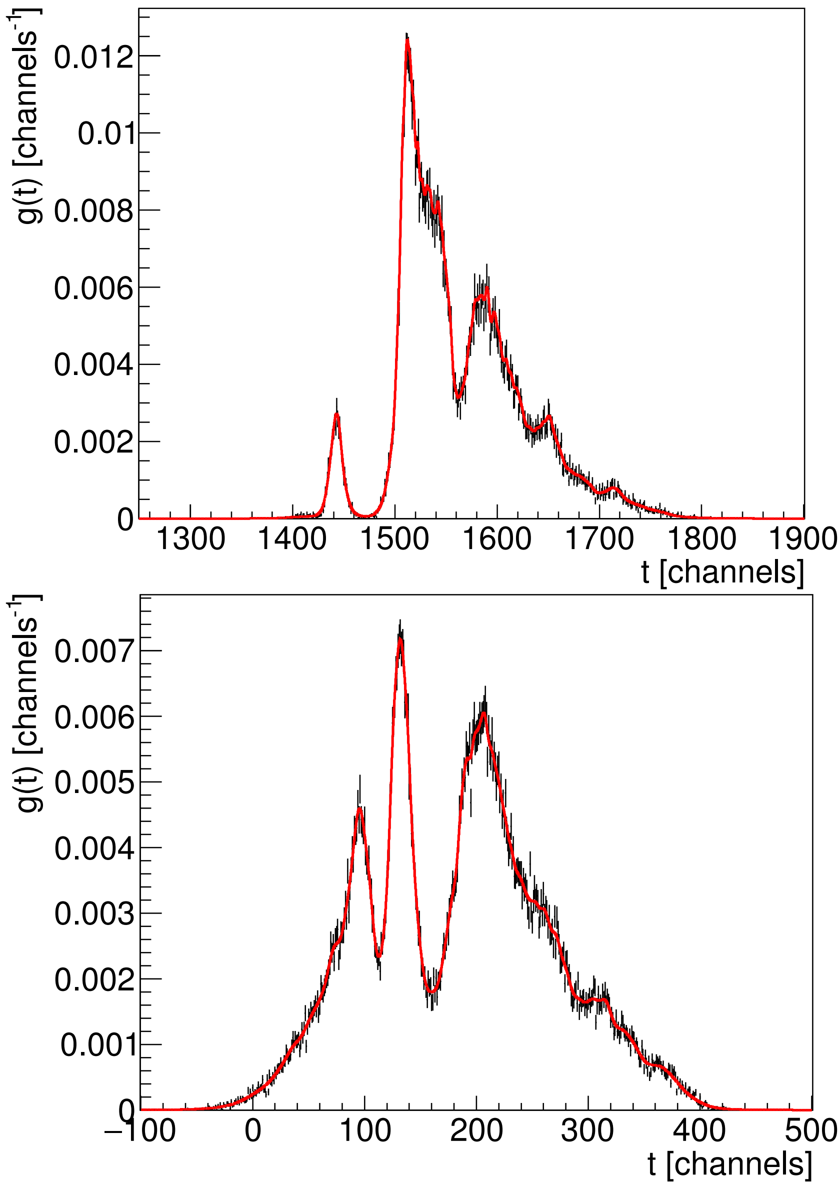

Figure 4.15.: Kernel density estimator measured on 16.11.2016 with a carbon target (top) and on 15.3.2016 with a polyethylene target (bottom).

For fitting, it was found that the following parametrization of (4.3) leads to better results:

$$f_A(t) = \frac{N}{2}\left[(1+\epsilon)g(t_1) + (1-\epsilon)g(t_1+\Delta t)\right]. \tag{4.6}$$

$N = N_1 + N_2$ is the total number of events, $\Delta t = t_2 - t_1$ is the difference in time between the two particle types and $\epsilon = \frac{N_1-N_2}{N_1+N_2}$ indicates the relative proportion of the particle types.

To reach a meaningful optimum in the fit, a good initial value close to the optimum is required. A robust initial estimate can be found by examining the mean, variance and third central moment of f_A as a function of the fit parameters. A central moment of a distribution is defined as

$$\mu_n = \int_{-\infty}^{\infty} f(t)(t-\hat{t})^n dt, \tag{4.7}$$

where $\hat{t}$ is the mean. The standard deviation σ is the square root of the second central moment.

Using this definition and (4.6) the following identities can be proven:

$$\hat{t} = \hat{t_0} + t_1 + \frac{1+\epsilon}{2}\Delta t \tag{4.8}$$

$$\sigma^2 = \sigma_0^2 + t_1 + \frac{1-\epsilon^2}{4}\Delta t^2 \tag{4.9}$$

$$\mu_3 = \mu_{3,0} + \frac{3}{4}(\epsilon - \epsilon^3)\Delta t^3. \tag{4.10}$$

The index 0 denotes properties of the distribution g, the corresponding variables without an index belong to f_A.

As $\hat{t}$, σ and μ_3 are known empirically for both f and g, equations (4.8), (4.9) and (4.10) can be solved for the fit parameters:

$$\epsilon = \frac{\mu_3 - \mu_{3,0}}{\sqrt{4(\sigma^2-\sigma_0^2)^3 + (\mu_3-\mu_{3,0})^2}} \tag{4.11}$$

$$\Delta t = \sqrt{4(\sigma^2-\sigma_0^2) + \left(\frac{mu_3 - \mu_{3,0}}{\sigma^2-\sigma_0^2}\right)^2} \tag{4.12}$$

$$t_1 = \hat{t} - \hat{t_0} - \frac{1+\epsilon}{2}\Delta t. \tag{4.13}$$

The total number of particles N can be trivially estimated using the integral over the histogram.

The final result is obtained by fitting (4.6) to time distribution for each amplitude bin using a χ^2-minimization and the above starting values.

Fig. 4.16 shows an example for a fit for one amplitude bin. The data is reproduced well by (4.6). Fig. 4.17 shows the amplitude spectrum for deuteron carbon scattering.

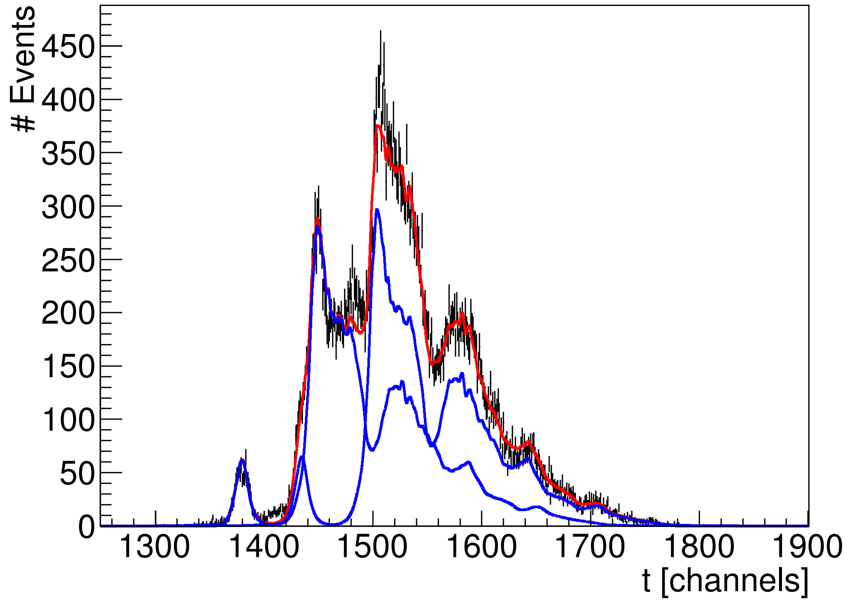

Figure 4.16.: Example of a fit of (4.6) to amplitude bin 160 in figs. 4.17 and 4.18.

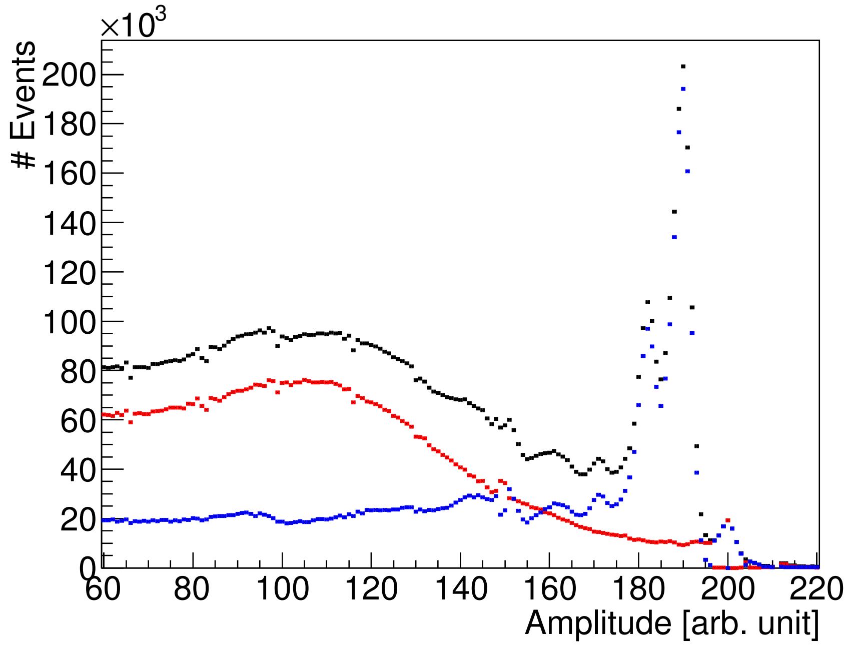

Figure 4.17.: Numbers of particles from carbon scattering. The blue histogram shows the number of deuterons, the red histogram shows the number of protons.

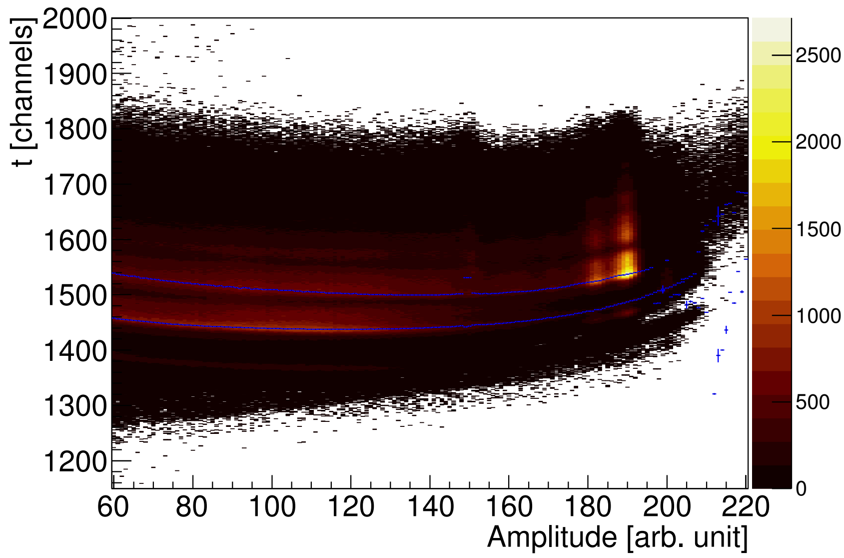

Figure 4.18.: Times of flight for the same data as above. Curves for t_1 and t_2 superimposed on the histogram.

Fig. 4.18 shows t_1 and t_2 plotted over the histogram. The time curves were shifted so that they go through the maximum of the kernel density estimator for their respective particle type. As expected, the time curve follow the visible maximuma in the histogram.

The method described here relies on a measurement of the time distribution in the $^{12}C(d,p)^{13}C$ peak with good statistics, requiring several hours of data taking. It can therefore not easily be adapted to online measurements. However, the results of the fits confirm the assumption that there are two types of outgoing particles and that the spread in time of flight is due to the cyclotron extraction.

4.3.4. Pulse Shape Measurements

The pulse shape measurement function was mainly implemented to verify that the hardware works correctly and to check for problems in ongoing measurements, such as possible baseline drifts. It is not regularly used to measure polarizations. During the beam time in spring 2015, pulse shape data was taken using carbon and polyethylene targets. Similar data was taken using a LYSO crystal in summer 2016, whose scintillation signal decays far more slowly than the signal of the organic scintillators. The data can be used to test the correct operation of the constant fraction discriminator and to compare it to possible other ways of signal processing.

Fig. 4.19 shows some typical pulses measured using the new hardware. Note that the amplitude axis uses the full 12 bits of the ADC and not the 9 bits that are used in the CFD output, so the scale differs by a factor of 8. Pulses have a rise time of about 5 ns and a total duration of about 20 ns. The CFD algorithm was simulated in software resulting in the red curve.

The amplitude of the time reference signal was too large to sample the complete sine

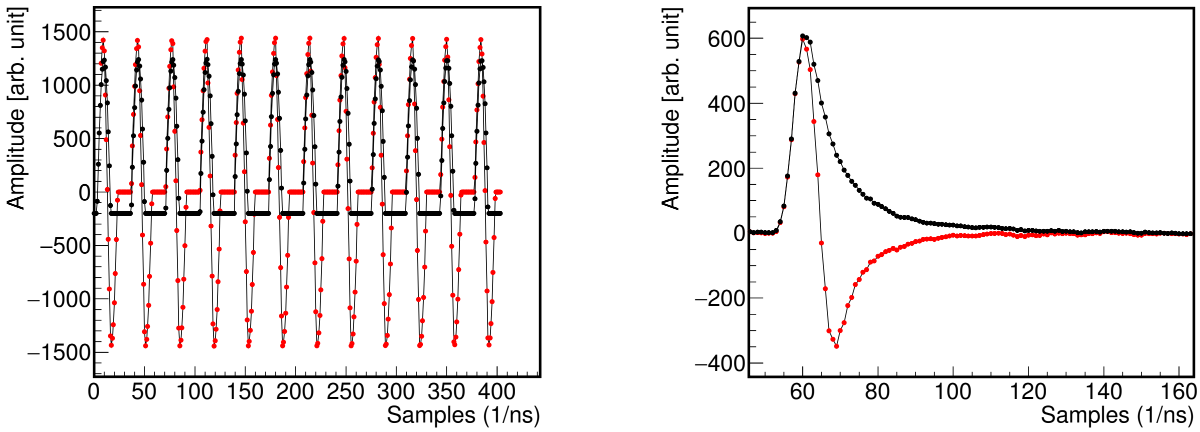

Figure 4.19.: Typical pulses from the cyclotron rf (left) and the plastic scintillators (right). The CFD algorithm was simulated in software. The black points are the measured amplitudes, the red points are the sum of the signal with a delayed and inverted copy of itself. The zero crossing of the red points is the pulse time.

shape. By setting the ADC baselines appropriately, it is possible to measure the voltage maxima, which are used as a timing reference using the same algorithm as for the pulses.

Data from pulse shape measurements can be used to compare different algorithms for determining the amplitude. The CFD uses the highest sample in a pulse, potentially leading to a larger statistical uncertainty than pulse integration. Fig. 4.20 shows integrals and maximum samples from the measured pulses. The integrals are computed by summing up the sample amplitudes from 15 samples before the maximum value up to 50 samples after it, thus including the complete area under the graph. To a good approximation, the integral is proportional to the maximum amplitude. When varying the boundaries of the integral to include only the rising or falling flank, the proportionality remains. There is no indication that the pulse shape differs depending on the type of incoming particle, which would result in distinct populations of pulses in fig. 4.20.

Fig 4.21 shows the amplitude spectrum of deuteron carbon scattering generated from pulses using the maximum amplitude and the pulse integration method. Both result in almost the same resolution of peaks.

In conclusion, an algorithm using pulse integration is unlikely to improve the accuracy significantly.

Fig. 4.22 shows the time difference and maximum signal amplitude from the simulated CFD. Although the statistics is far lower because of the reduced data rate, the results qualitatively match fig. 4.13. This indicates that the CFD on the board is working correctly.

Fig. 4.23 shows a LYSO crystal scintillator being tested at LEP. LYSO (lutetium-yttrium oxyorthosilicate) is an inorganic scintillating material with a better energy resolution than organic materials and a slower decay time, although the pulses still decay faster than in most other inorganic scintillators.

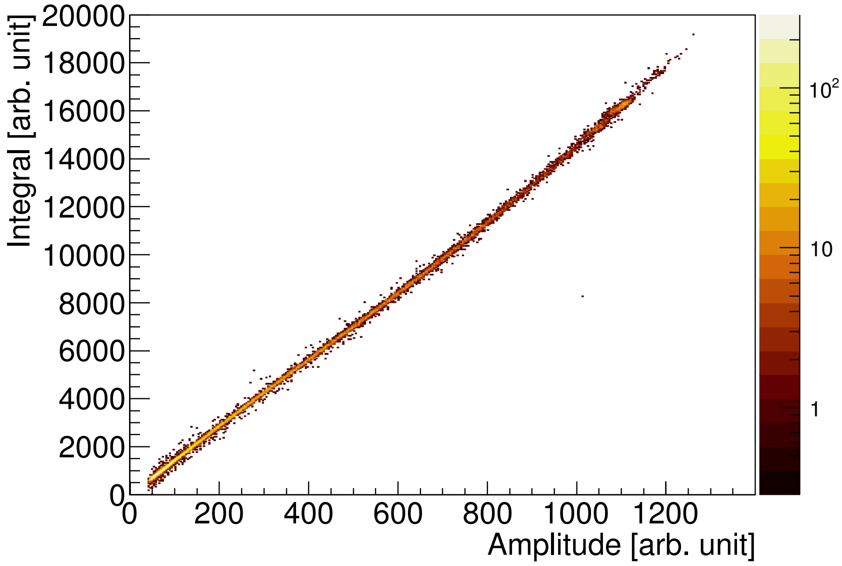

Figure 4.20.: Maximum pulse amplitudes and integrals from an offline simulation of the CFD algorithm

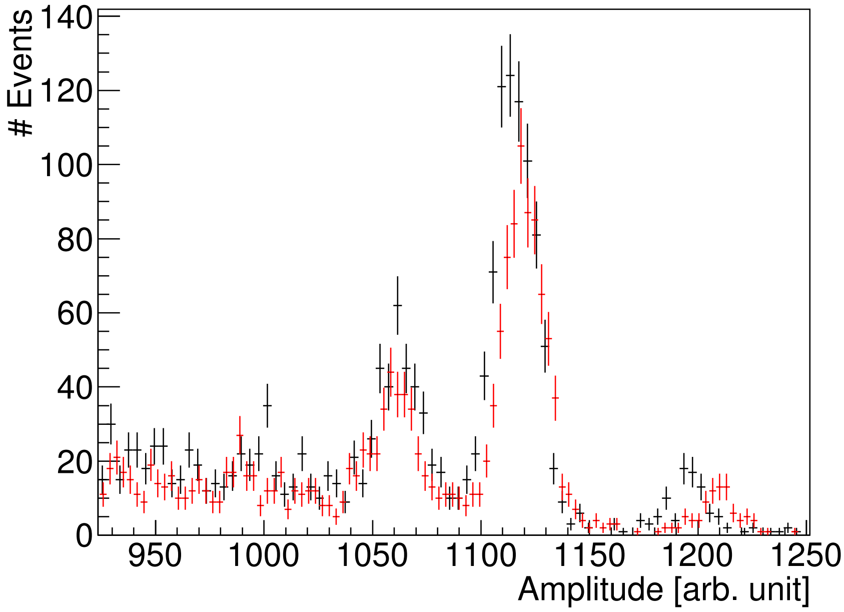

Figure 4.21.: Spectrum of deuteron carbon scattering using the maximum amplitude method (black), and the integral method (red), for the same data. The spectra are rescaled along the x-axis to match the peak positions.

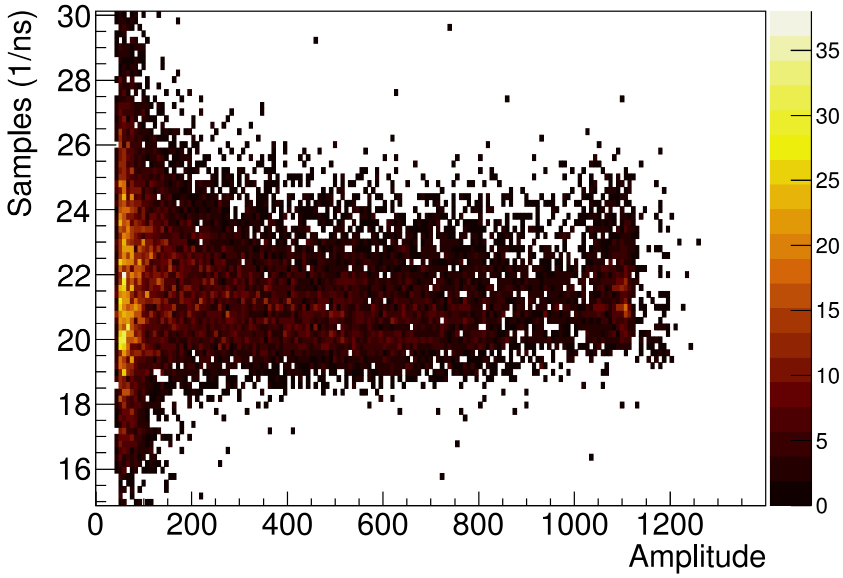

Figure 4.22.: Pulse amplitudes and times with respect to the cyclotron rf from the simulated CFD algorithm

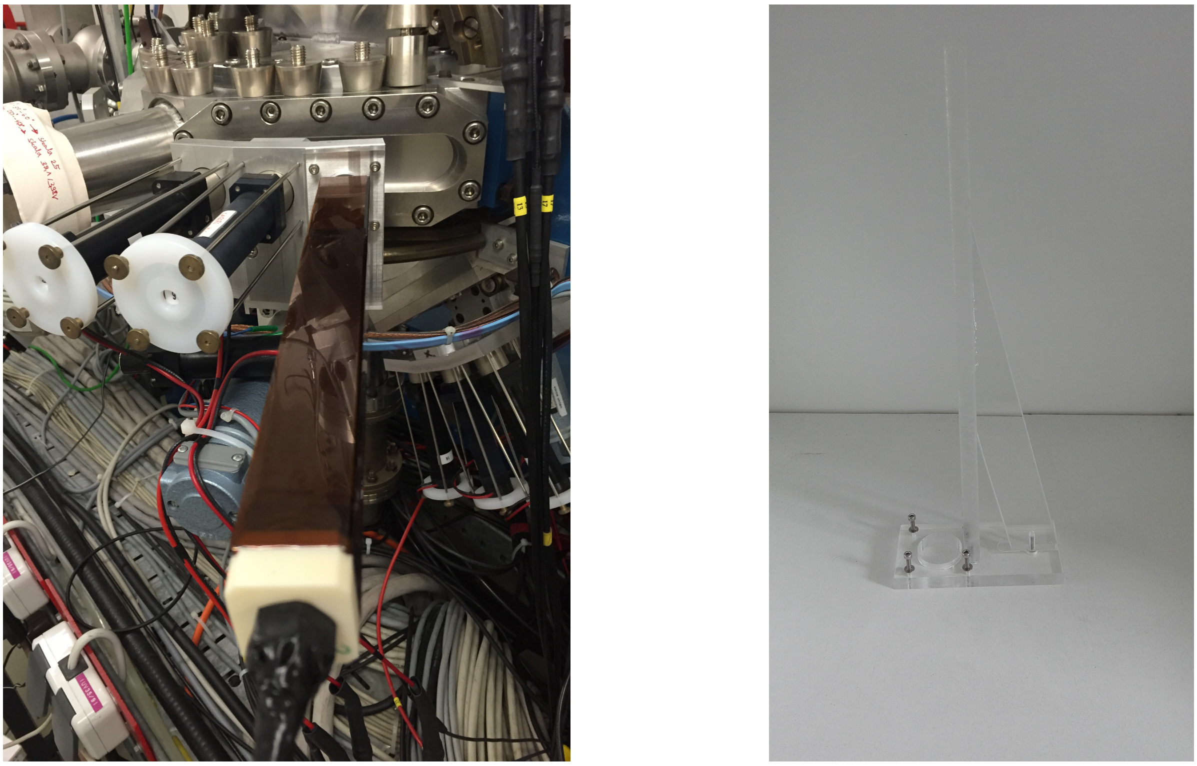

Figure 4.23.: Lyso crystal installed at the Low Energy Polarimeter (left) and detector holder (right)

The most forward organic scintillator on the right side of the beam was removed to make place for the LYSO detector. The LYSO module tested here was developed for a future polarimeter to be used in an EDM storage ring. The crystal has a cuboid shape of 3 cm by 10 cm, a silicon photomultiplier (SiPM) is was used for read-out.

Fig. 4.24 shows a pulse measured using the LYSO detector. Its rise-time is about 25 ns at a total length of about 250 ns. The increased pulse length is a problem for the amplitude determination in the CFD. With a maximum delay of 12 ns and a search window for the maximum of 10 ns, the maximum value found is on the rising flank and varies considerably. Fig. 4.25 shows the spectrum measured using the CFD on the FPGA and using an offline analysis taking the maximum sample in each pulse. The offline analysis yields better results. Due to the problems with the CFD, no timing measurements could be taken.

The LYSO spectra show no strong improvement in resolution compared to spectra taken with the organic scintillators. Although LYSO crystals should have a better energy resolution, the spectrum is blurred by the large acceptance angle of the detector. Half of the width of the crystal, 1.5 cm, is equivalent to a change in scattering angle of 4° or a change of the kinetic energy of about 1% at 40°, which is a significant fraction of the observed width. In conclusion, the performance of LEP would probably not improve significantly if the detectors were replaced with LYSO crystals.

4.3.5. Analyzing Power Measurements

This section presents analyzing power data taken in fall 2016 during the so-called database run. The main aim of the beam time was to measure analyzing powers and differential cross sections for deuteron carbon scattering and background reactions at different energies using the WASA detector [38]. The results can be used in the design of future polarimeters for EDM measurements.

In the main ring, deuteron energies of 170, 200, 235, 270, 300, 340 and 380 MeV were used. Analyzing power data is available at energies of 140, 200 and 270 MeV for deuteron proton scattering. This data is used to calibrate the beam polarization for measurements at the other energies.

The calibrated polarized beam makes parasitic measurements of the analyzing power at the Low Energy Polarimeter possible, assuming that the polarization does not change during injection. Five different polarization states were used (see table 4.5). The analysis

Table 4.5.: Polarization states during database run in 2016 with ideal P_z and P_{zz}

Name	P_z	P_{zz}
vec1	$-\frac{2}{3}$	0
vec2	$\frac{2}{3}$	0
tens1	$\frac{1}{2}$	$-\frac{1}{2}$
tens2	-1	1
unpol	0	0

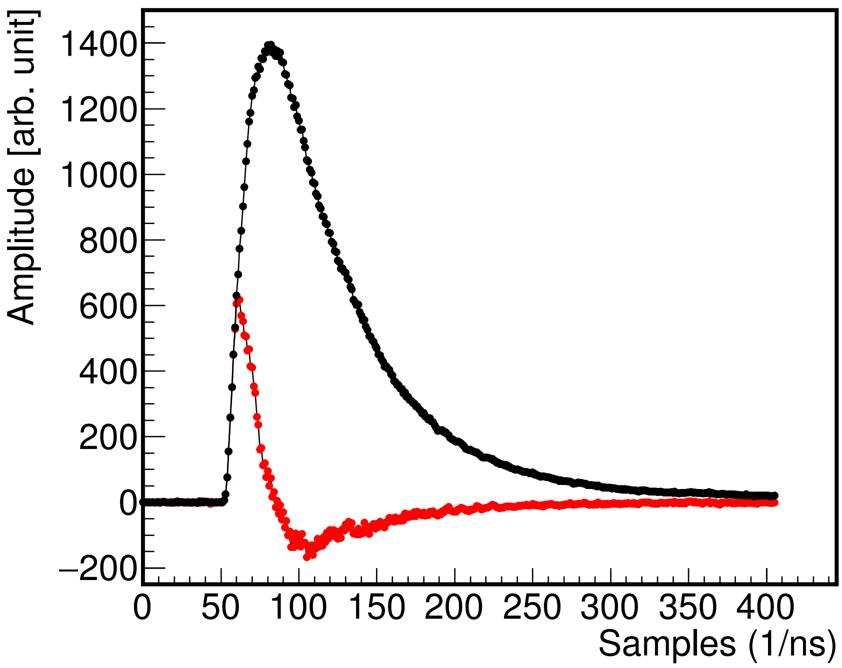

Figure 4.24.: Pulse measured using a LYSO crystal

of the WASA data is not finished as of May 2017, which means that the final polarization calibration is not available. Only uncalibrated data is presented here.

The data at the Low Energy Polarimeter was taken using all three detectors at each side, taking data for three different angles simultaneously. The detectors were moved in steps of 2.5° until the most forward detector arrived at the position the central detector initially had. Amplitude and time of flight spectra were measured at each point. Data on the total beam luminosity of the different states is not available.

The aim of the data analysis is to estimate the number of particles from elastic scattering, inelastic scattering at 4.4 MeV excitation energy and $^{12}C(d,p)^{13}C$ at each point. The asymmetries for each reaction and state are calculated as a function of the scattering angle.

The number of elastic and 4.4 MeV inelastic events is obtained using a fit of two normal distributions. Fig. 4.26 shows an example for one angle and polarization state. The background is estimated using a flat line between the local minima to the left of the inelastic peak and to the right of the elastic peak. The peak of the protons from the $^{12}C(d,p)^{13}C$ reaction is assumed to be background free. Here the number of events is estimated by integrating over the histogram from the second local minimum upward.

Fig. 4.27 shows the resulting asymmetries for the different reactions. The error bars in the y-direction result from the statistical uncertainty, the error bars in x-direction are the estimated uncertainty of the angle scale at the polarimeter. In the right column, the asymmetries have been corrected to set the unpolarized state to zero.

There are likely more systematic errors as the asymmetries of the vec1 and vec2 states are not proportional to each other within the statistical uncertainty, which would

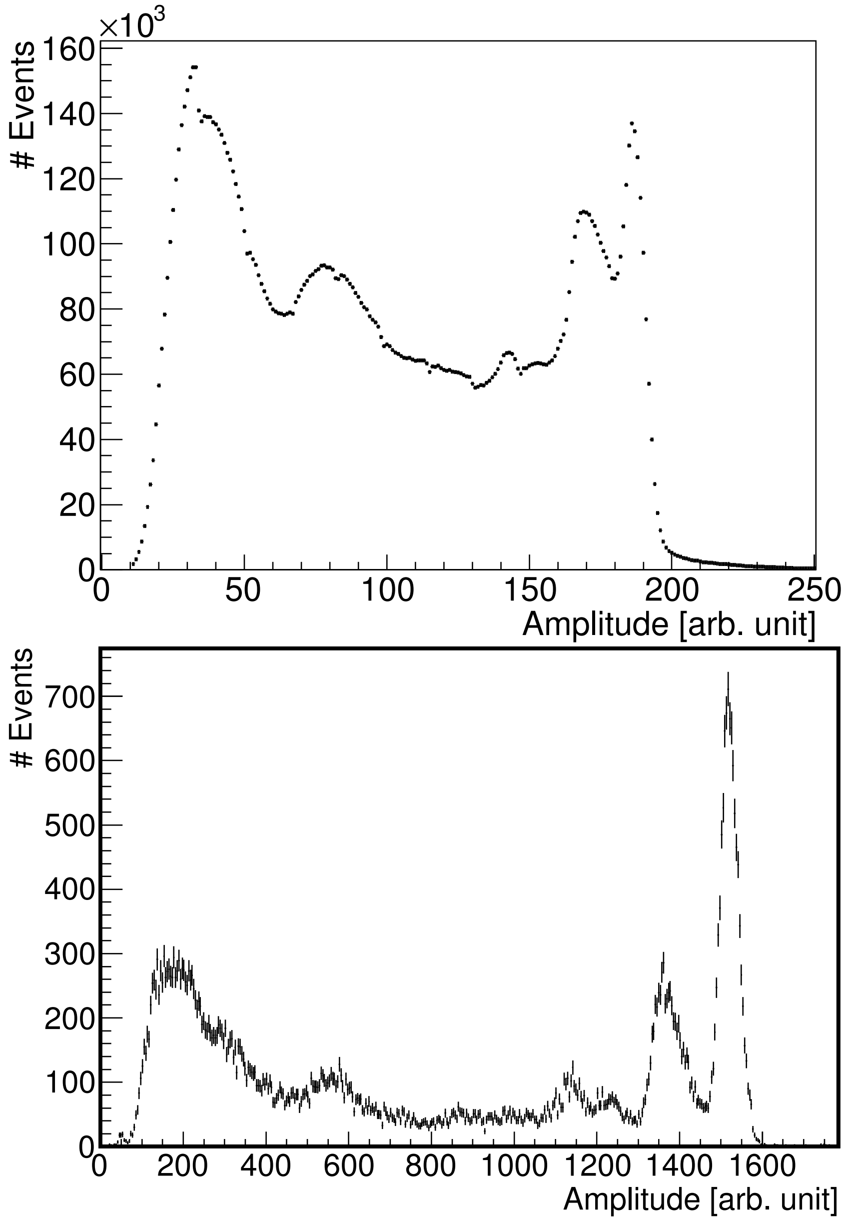

Figure 4.25.: Energy spectrum measured with LYSO crystal using the CFD (top) and an offline analysis of the data (bottom)

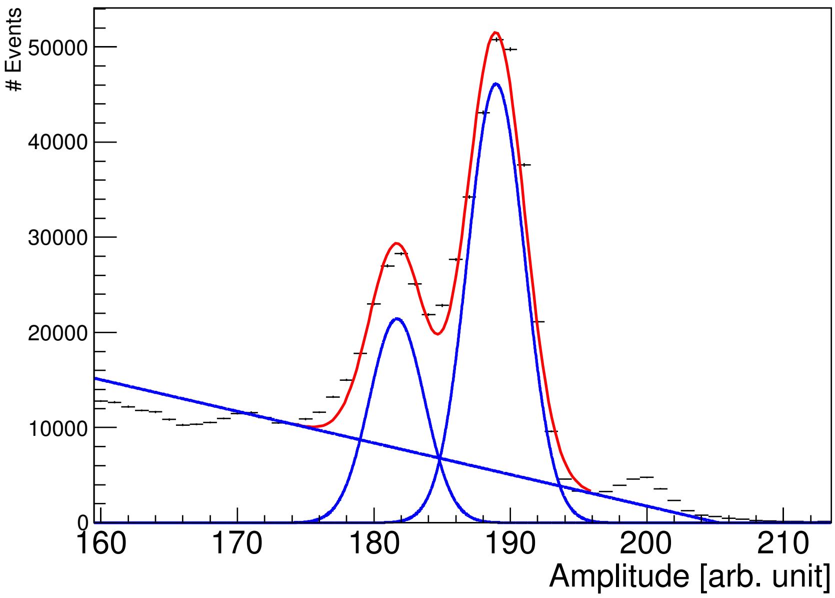

Figure 4.26.: Fit to an amplitude spectrum to obtain the numbers of elastic and inelastic events

be expected from the equations in table 2.2. The elastic scattering reaction has a low analyzing power at 30° which increases up to 40° and then remains almost flat. Inelastic scattering only shows asymmetries at higher angles over 40°. The protons from the stripping reaction show an almost constant asymmetry over all angles.

The tensor asymmetries are consistent with zero.

4.3.6. Performance and Comparison to the Old System

The new read-out system has been used as a routine tool for monitoring and setting up the polarized source since the end of 2015, regularly running for several days without interruption. Compared to the old readout system (see section 4.2.1), the new system has several advantages.

In the old system, the rate measurements were separate from the spectrum measurements. The discriminator window was set roughly using an oscilloscope. There was no way to see the limits of the discriminator window in the amplitude spectra. This could result in problems as the scale of the amplitude measurements can shift during measurements, moving the peaks out of the selected amplitude window.

Fig. 4.28 shows a typical development of the amplitude spectrum over time. The spectrum remains constant for hours to days but can occasionally and abruptly shift so that the analysis settings have to be adjusted. The shifts are in the same order of magnitude as the elastic peak width. With the new system, these shifts can be detected and corrected for in the offline data. They are also visible in the online data shown by the MQTT client.

The data rate of $20\,\mathrm{MB\,s^{-1}}$ per GANDALF module allows for transmitting amplitude

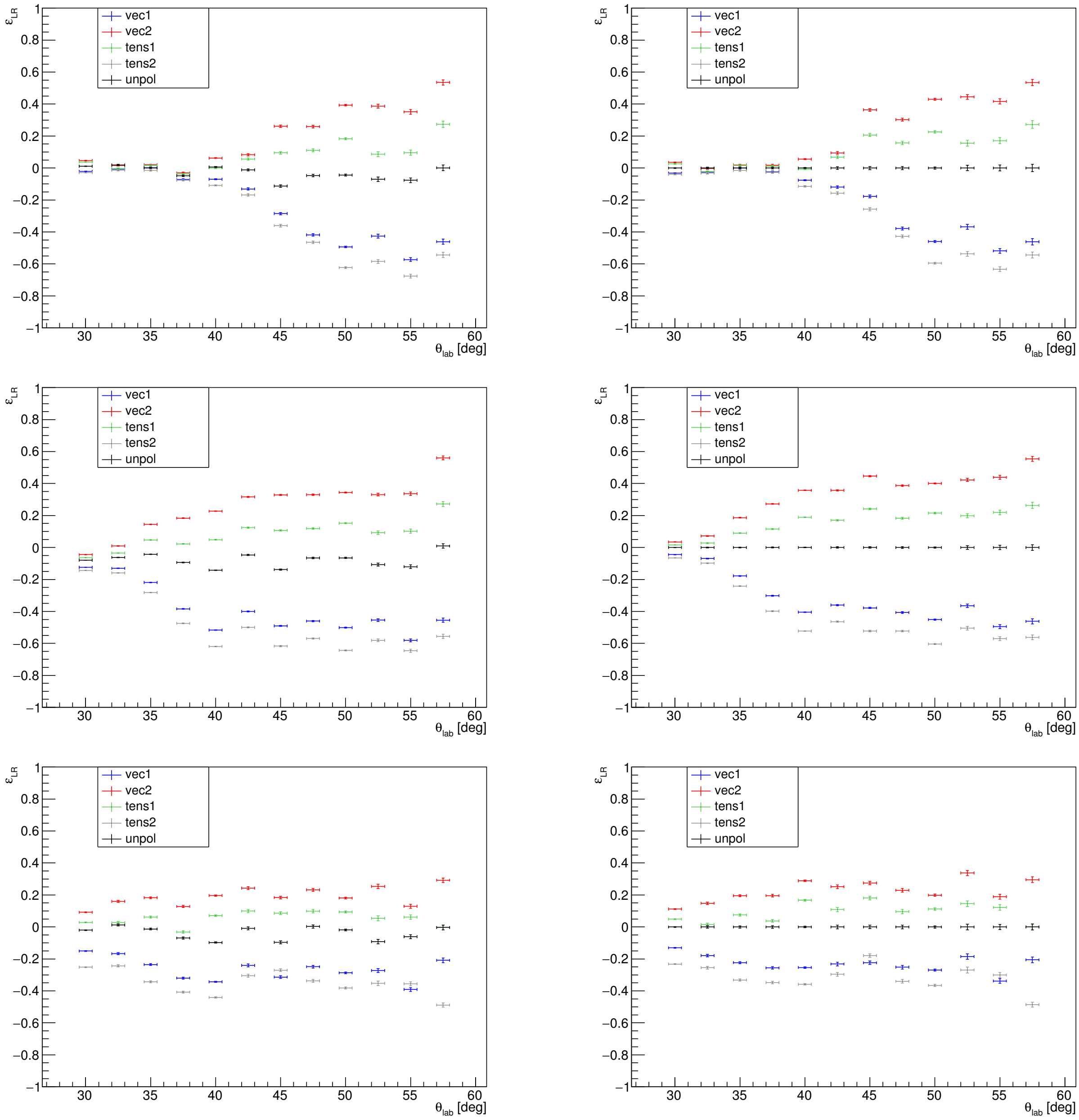

Figure 4.27.: From top to bottom: Left-right asymmetries for 4.4 MeV inelastic scattering, elastic scattering and $^{12}C(d,p)^{13}C$. The right column is corrected for the asymmetry of the unpolarized state.

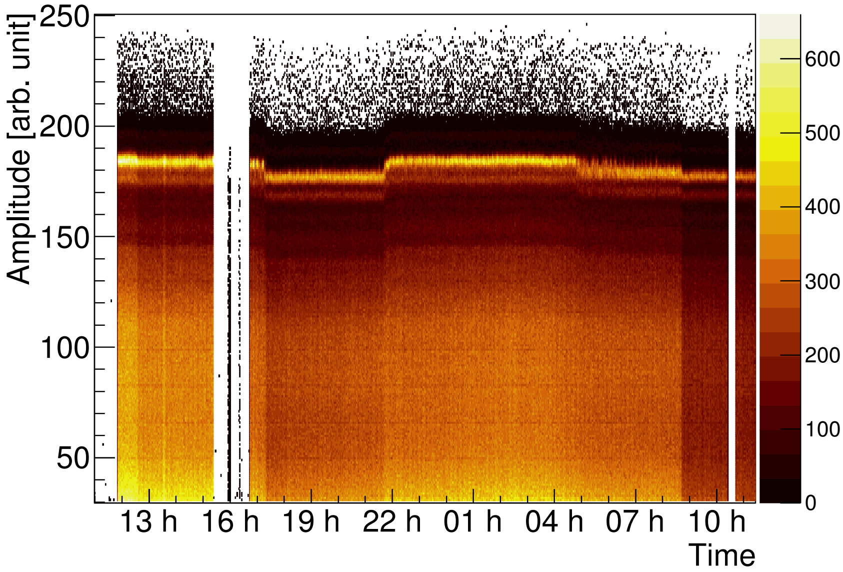

Figure 4.28.: Amplitude spectrum as a function of the system time

data at a rate of five million events per second, or time data at half that rate. Almost all data is sent during the 20 ms per 2 s duty cycle during which the beam is on. The 4096 words that fit in the output buffer are negligible.

Typical rates observed over the complete spectrum range from 30 kHz at 50° to over 150 kHz at 30°. The old system typically worked with rates around 10 kHz, requiring proportionately longer measurements.

The read-out was originally designed with rates in the order of several megahertz per channel in mind, so that the band width of the USB port would have been exhausted. The prescalers for all hardware modules were included in the design for that reason and tested successfully with a standard pulser.

4.3.7. Outlook

While the performance of the Low Energy Polarimeter has been satisfactory, there are several possible improvements.

The software part of the read-out could be automated to a greater extend. The position of the elastic peak could be determined continuously by a peak finding algorithm, which would recognize shifts of the amplitude spectrum as shown in fig. 4.28. This could make the manual analysis script redundant.

The ability of LEP to measure tensor polarization is limited by its angular acceptance. It has been proposed to shift the target inside the central vacuum chamber about 15 cm upstream to measure more forward scattering angles. This arrangement would allow for coincident measurements of deuteron proton scattering with the existing detector mounting at proton laboratory angles of 22° and deuteron angles of 28.5°. The center of mass scattering angle would be 135°, where the analyzing powers show a local maximum. If LEP could measure tensor polarization this way, it could be used to provide a beam polarization calibration for later experiments with polarized beams.

In addition to the use at LEP, a GANDALF module could also be used for diagnostics in the cyclotron. The cyclotron has eight phase probes that measure the position of the beam using a capacitive pick-up. The resulting signals have the same frequency as the cyclotron rf voltage and could be sampled and analyzed using GANDALF.

4.4. Conclusion

The new read-out system is a significant improvement over the old electronics. The detection rates were improved by a factor of 3 to 15, depending on the angle.

For the first time, the time of each event relative to the cyclotron frequency could be measured. Although the new time spectra are not used for polarimetry, they lead to a better understanding of the background.

The new electronics stores the amplitude and time data for each event, making offline analysis possible. The amplitude spectra are also sent to the COSY MQTT servers, allowing for an easier optimization of the polarized source.

5. Analysis of Feedback System Data

This chapter deals with the second main topic of the thesis, the analysis of data taken with the spin feedback system.

The feedback system was installed and successfully tested in the fall of 2015 [56]. Sections 5.1 and 5.2 are based on that publication. The purpose of the feedback system is to keep the spin precession in phase with the rotation of the beam around the ring, which is required for an EDM precursor experiment at COSY using the Wien filter method (see section 2.3.4).

The feedback system was used in two different types of experiments. The first type are vertical polarization build-up experiments, during which the polarization is rotated slowly from the horizontal plane towards the vertical axis (section 5.2). During the whole cycle, the feedback system is active, keeping the relative phase constant as the polarization vector moves. Since the speed of vertical spin build-up is a function of the phase, this measurement can be used to validate the feedback system.

The second type of experiments deals with driven spin oscillations induced by the rf solenoid (section 5.3). The feedback system was used to set the initial phase difference. After that, the solenoid was switched on and the feedback system was switched off, allowing the phase to move freely. This resulted in an oscillation of the vertical polarization and of the phase.

5.1. Design

In general, feedback means that the output of a system is reentered as an input, creating a closed loop. In case of the spin feedback system, this output is the relative phase of the spin precession and the rf solenoid. This phase is constantly measured and adjusted by changing the COSY frequency and thereby the beam velocity. This changes the phase of the spin precession at the detector because the particles arrive at a different time and because the spin tune is changed.

A Wien filter is being developed for use at COSY [57] but was not ready for the commissioning of the feedback system. The rf solenoid was used as a substitute. The solenoid works in a similar way to the Wien filter, but rotates the spins about the beam axis rather than the vertical axis.

Fig. 5.1 shows the basic principle of the feedback system. COSY is operated with a bunched beam, which is required anyway to achieve sufficient spin coherence times. The beam velocity can therefore be adjusted using the rf frequency of the accelerator cavities.

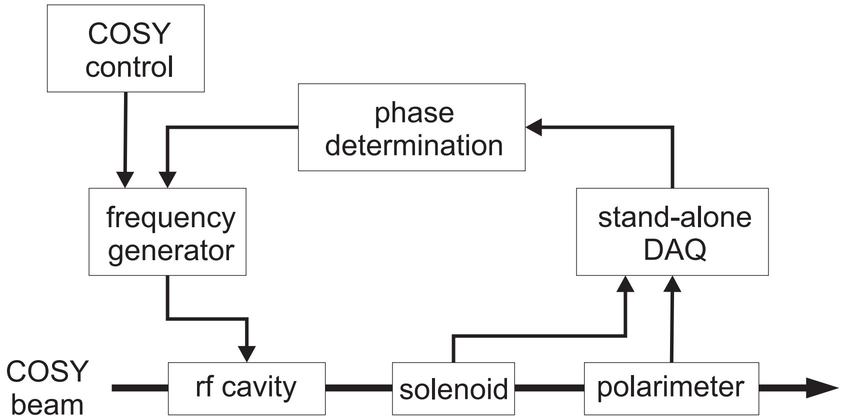

Figure 5.1.: Basic principle of the feedback system [56]

The frequency is chosen based on the phase difference between the solenoid and the spin precession. The rf frequency of the solenoid (and later the Wien filter) is measured along with all events in the polarimeter on a common reference clock. The phase of the spin precession is calculated using the algorithm described in [46] (see also section 3.2.2).

The measured phase difference

$$\phi_{\text{meas}} = \phi + \phi_{\text{det}} \tag{5.1}$$

is shifted from the phase difference at the solenoid by a constant offset. The offset ϕ_{det}, where "det" stands for detector, is due the different positions of the polarimeter and the solenoid in the ring, and to cable delays. One measurement of the phase difference takes about 2 s.

Changing the accelerator frequency f_{COSY} has two effects on the phase difference: the spin tune of the machine changes and the particles arrive at the solenoid at a different time. The phase difference at a given turn number n is

$$\phi(n) = 2\pi n \left(\frac{f_{\text{rf}}}{f_{\text{COSY}}} - \nu_s \right) + \phi_0, \tag{5.2}$$

where ϕ_0 is the phase at $n = 0$ and f_{rf} is the external frequency to which the spin precession is adjusted, either the solenoid frequency or later the Wien filter frequency. Taking the derivative with respect to f_{COSY} yields

$$\frac{d\phi}{df_{\text{COSY}}} = 2\pi n \left(-\frac{f_{\text{rf}}}{f_{\text{COSY}}^2} - \frac{d\nu_s}{df_{\text{COSY}}} \right). \tag{5.3}$$

The first term in the sum corresponds to the time at which the beam arrives at the solenoid, the second term corresponds to the change in spin tune. Using $\nu_s = \gamma G$, that term becomes

$$\frac{\Delta\nu_s}{\nu_s} = \frac{\Delta\gamma}{\gamma} = \beta^2 \frac{\Delta p}{p} = \frac{\beta^2}{\eta} \frac{\Delta f_{\text{COSY}}}{f_{\text{COSY}}}. \tag{5.4}$$

$\eta = -0.58$ is the so-called slip factor, which is defined as the ratio of the relative change in momentum and frequency. At COSY, the numerical value is

$$\frac{d\phi}{dt} \approx 6.93 \frac{\text{rad}}{\text{Hz s}} f_{\text{COSY}}. \tag{5.5}$$

The COSY frequency can be adjusted in steps of 3.7 mHz, resulting in $\frac{d\phi}{dt} = 26\,\text{mrad/s}$ per step.

At the beginning of a run, the feedback system sets the phase to the specified value by setting a large frequency difference for a short period of time in the order of 100 ms. This is repeated during the run if the phase difference becomes sufficiently large. To stabilize the phase at the right value, the phase is adjusted in smaller steps for longer periods of time.

Fig. 5.2 shows the effect of the feedback system over one cycle. During the test runs, the phase could be kept stable within a standard deviation of 0.21 rad. Without feedback, the phase drifted over the complete 2π angular range. [56]

5.2. Vertical Polarization Build-Up

5.2.1. Experimental Procedure

The feedback system was validated by tilting the spin up or down slowly using the solenoid while keeping the feedback running. While the measurement of the phase difference over the course of one beam storage already proves that the feedback is working, the measurement of the vertical build-up has some additional advantages. The build-up rate depends on the phase difference at the solenoid, not at the polarimeter, providing a way to measure ϕ_{det} in (5.1). The method also proves that the feedback system still works when the spin is being moved. Finally, the slow tilt from the horizontal plane towards the vertical axis resembles the expected EDM signal. The effects of a limited spin coherence time also apply to future EDM measurements (see section 5.2.3).

Fig 5.3 shows the principle of a build-up measurement. Two different initial polarization states are used, one with positive vertical vector polarization (0.30 ± 0.03) and one with negative polarization (-0.46 ± 0.03). The tensor polarization is zero. The polarization is first tilted into the horizontal plane by switching on the rf solenoid briefly at a high amplitude. While the spin is precessing about the vertical axis, the feedback system is switched on and the phase is set to the specified value. 115 s after the start of the run, the solenoid is switched on again at a lower amplitude, causing a small rotation of the polarization about the longitudinal axis every turn. This leads to a gradual build-up of vertical polarization at a rate that is proportional to $\sin\phi$ to a good approximation. $\phi = 0$ means that the polarization vector is parallel to the beam momentum when the solenoid field is at maximum strength, which means that the rotation has no effect. For $\phi = \pm\pi/2$ the polarization is perpendicular to the beam, so the build-up rate reaches its maximum value.

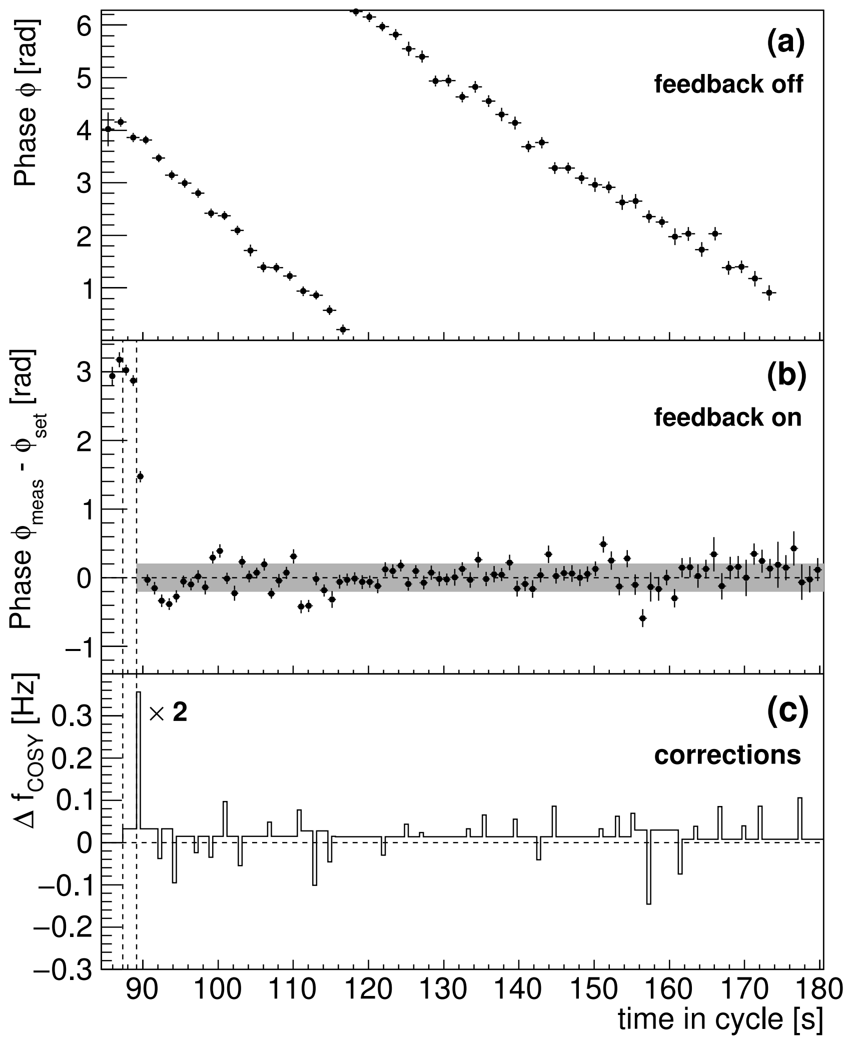

Figure 5.2.: Relative phase over one cycle without feedback (top) and with feedback (center). The bottom plot shows the corrections to the COSY frequency.

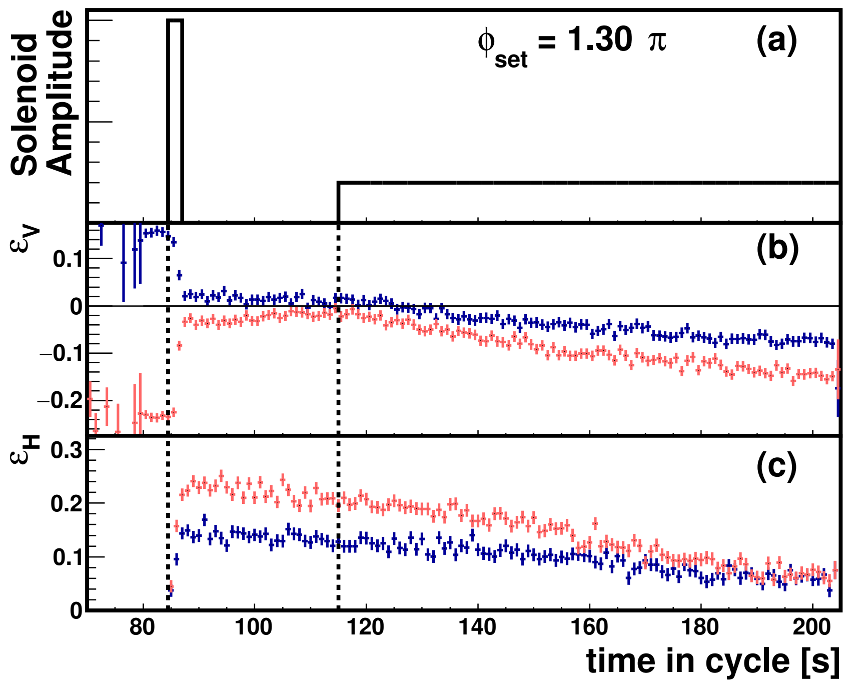

Figure 5.3.: Principle of a vertical polarization build-up measurement. The vertical asymmetry ε_V is proportional to the vertical polarization, ε_H is proportional to the in-plane polarization. (already published in [56])

To verify that the phase is really set to a constant value, the build-up rate is measured as a function of the phase for ϕ values from 0 to 2π. Several curves were measured at different amplitudes of the solenoid. For some measurements, a 20 dB attenuator was added to the solenoid signal input to reduce the amplitude below the minimum value possible with the normal frequency generator.

5.2.2. Simple Analysis

The goal of the analysis is to calculate the build-up rate of the vertical polarization from the polarization measured over time. The vertical polarization can be obtained from the asymmetry of the counting rates between the left and right detector parts

$$\varepsilon_V = \frac{N_L - N_R}{N_L + N_R}. \tag{5.6}$$

As the tensor polarization is zero, ε_V is proportional to the vertical component of the vector polarization.

The horizontal polarization component is obtained from the spin tune algorithm. It is proportional to the horizontal asymmetry ε_H, which is identical to $\tilde{\varepsilon}$ in equation (3.4) and was renamed here for consistent notation.

The angle between the horizontal plane and the polarization vector is

$$\alpha = \arctan \frac{P_V}{P_H} = \arctan \frac{\varepsilon_V}{\varepsilon_H}. \tag{5.7}$$

This angle is independent of the magnitude of the polarization and of analyzing powers, making it a convenient variable to describe the effect of the solenoid.

α cannot be rotated beyond $\pm\pi/2$ while the feedback is active. When the polarization vector is vertical, it will not precess as it is parallel to the magnetic field. The phase of the spin precession is undefined, so there is no reference point for the feedback system. The solenoid is still running and can still move the spin. However, whenever the solenoid has created an appreciable horizontal polarization, the feedback system tries to adjust the phase again, which prevents the solenoid from running on resonance properly.

Fig. 5.4 shows α as a function of time for $\phi = 0.5\pi$. The initial asymmetries are close to zero. After the solenoid is switched on again at $t = 115\,\mathrm{s}$, there is a roughly linear decrease in α. The curve looks similar for both initial polarization states.

A curve of α over time is calculated for each value of ϕ and for each polarization state. The slope is determined by fitting a straight line trough the curves.

Fig 5.5 shows these slopes as a function of ϕ. The curve follows the expected sinusoidal shape. There is no significant difference between measurements taken with a positive or negative initial polarization, proving that the results do not depend on the initial polarization direction and magnitude.

The sine is phase shifted because the slope is proportional to the sine of the relative phase at the solenoid, while the phase that the feedback system uses (on the x-axis in fig 5.5) is defined at the polarimeter. The initial phase of the observed sine is therefore ϕ_{det}.

The observation of the sinusoidal dependency of the build-up rate on the relative phase is another proof that the method works even when the polarization is being rotated.

5.2.3. Spin Coherence Time

The analysis in section 5.2.2 and [56] assumes that the magnitude of the polarization is stable over time. In fact, a significant fraction of the initial polarization decays over the course of one COSY cycle. This effect can influence the measured slope, because the horizontal and vertical polarization components decay at different rates, which is illustrated in fig. 5.6. While the vertical polarization is essentially stable, the in-plane component decays due to decoherence, faking a tilt towards the vertical axis. For example, in a situation with $\alpha = \pi/4$, ε_H and ε_V would be equal. Even without a solenoid, ε_H will decay, leaving only the vertical component and a final α of $\pi/2$.

The effects of spin decoherence and the solenoid (or an EDM signal) can be distinguished by examining the magnitude $P = \sqrt{P_V^2 + P_H^2}$ of the polarization as well. The horizontal part is determined using the spin tune algorithm, see section 3.2.2. The solenoid conserves the magnitude of the polarization as it only rotates the vector. Spin decoherence causes a loss in magnitude. As the vertical and horizontal asymmetries are proportional to the respective vector polarization components, it is possible to define a polarization magnitude $\varepsilon = \sqrt{\varepsilon_V^2 + \varepsilon_H^2}$.

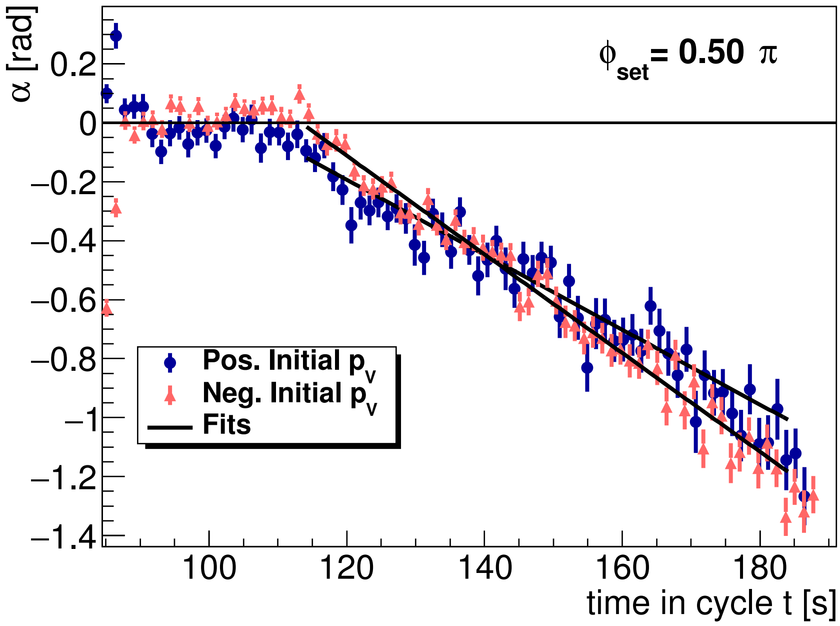

Figure 5.4.: α plotted for one run for both initial polarization states (already published in [56])

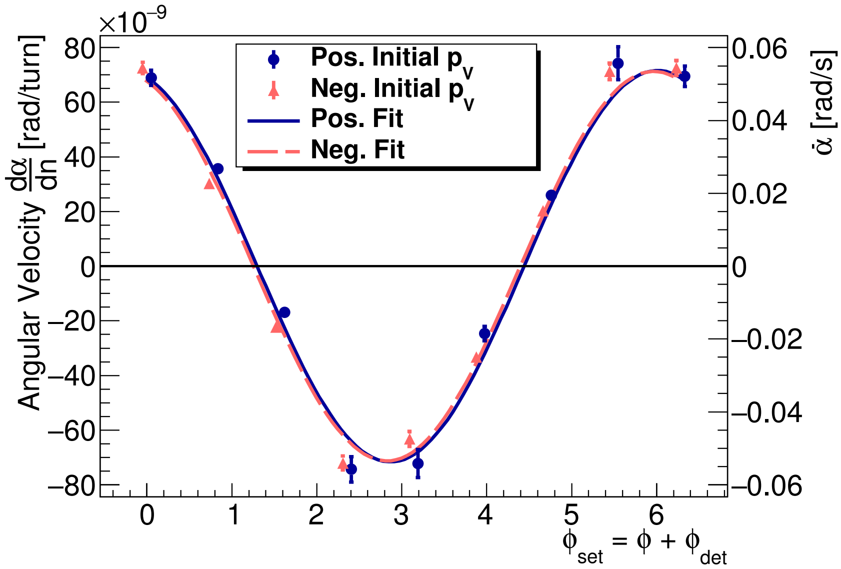

Figure 5.5.: Slope $\frac{d\alpha}{dt}$ as a function of ϕ (already published in [56]). The points were shifted horizontally for better readability

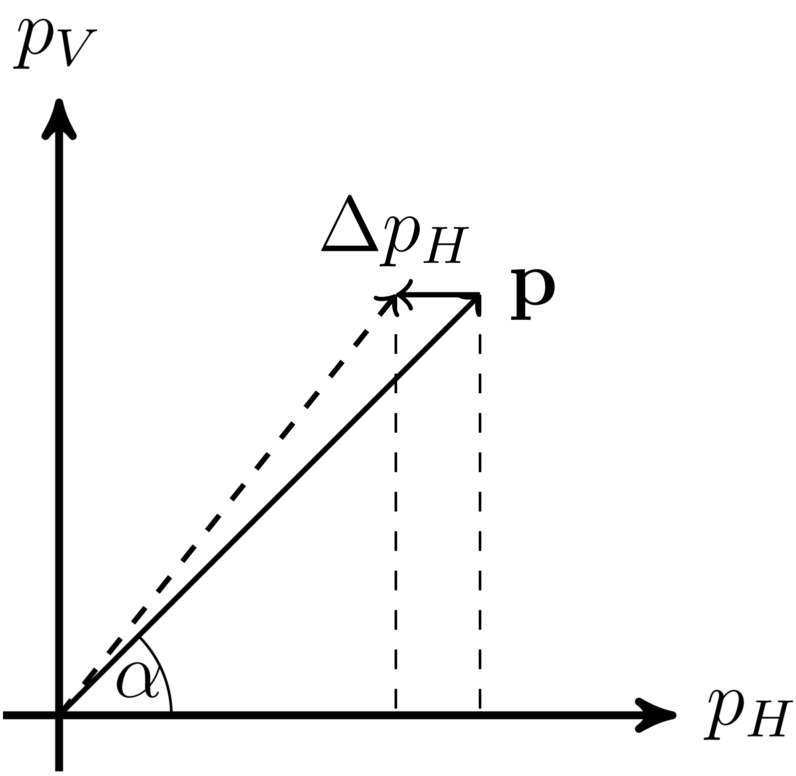

Figure 5.6.: Effect of spin decoherence on vertical polarization build-up

The evolution of α and ε can be modeled using two coupled differential equations:

$$\begin{aligned}
\frac{d\alpha}{dt} &= \frac{\partial\alpha}{\partial t} + \left.\frac{\partial\alpha}{\partial\varepsilon_H}\right|_{\varepsilon_V} \frac{\partial\varepsilon_H}{\partial t} \\
\frac{d\varepsilon}{dt} &= \frac{d}{dt}\sqrt{\varepsilon_V^2 + \varepsilon_H^2} \\
&= \frac{1}{\sqrt{\varepsilon_V^2 + \varepsilon_H^2}} \left[\varepsilon_V \frac{d\varepsilon_V}{dt} + \varepsilon_H \frac{d\varepsilon_H}{dt}\right] \\
&= \frac{1}{\varepsilon} \left[\varepsilon_V \left.\frac{\partial\varepsilon_V}{\partial\alpha}\right|_{\varepsilon} \frac{\partial\alpha}{\partial t} + \varepsilon_H \left(\frac{\partial\varepsilon_H}{\partial t} + \left.\frac{\partial\varepsilon_H}{\partial\alpha}\right|_{\varepsilon} \frac{\partial\alpha}{\partial t}\right)\right]
\end{aligned} \tag{5.8}$$

The subscript in the derivatives indicates the variable that is treated as a constant. These equations result from the chain rule of calculus and do not yet make any model assumptions. The explicit time dependency of α only comes from the solenoid, hence

$$\frac{\partial\alpha}{\partial t} = k \sin\phi =: A. \tag{5.9}$$

k is the angular velocity at which the solenoid rotates the spin and ϕ is again the phase difference.

Although the decay rate of P_H is measured while optimizing the sextupole magnets for maximum spin coherence time, these measurements cannot be easily reused for the build-up experiment as the solenoid itself can have an influence on the spin coherence time. In each turn, the solenoid rotates the spin distribution about the longitudinal axis, changing the precession phase of each spin and hence the width of the total distribution.

The decay of the in-plane polarization is approximated as proportional to the in-plane polarization itself, which would result in an exponential decrease over time without a solenoid.

$$-\frac{1}{\varepsilon_H}\frac{\partial\varepsilon_H}{\partial t} = \text{const.} =: B \tag{5.10}$$

This model does not precisely match the behavior over time observed in studies of the spin coherence time [43], but allows for a reasonable estimate. As explained above, the shape measured without a solenoid cannot easily be transferred to the case with a solenoid.

The remaining partial derivatives in (5.8) can be found geometrically from fig. 5.6 and the fact that ε is proportional P.

$$\begin{aligned}
\left.\frac{\partial\varepsilon_V}{\partial\alpha}\right|_{\varepsilon} &= \varepsilon_H \\
\left.\frac{\partial\varepsilon_H}{\partial\alpha}\right|_{\varepsilon} &= -\varepsilon_V \\
\left.\frac{\partial\alpha}{\partial\varepsilon_H}\right|_{\varepsilon_V} &= -\frac{\varepsilon_V}{\varepsilon^2}
\end{aligned} \tag{5.11}$$

Inserting all these into (5.8) yields

$$\begin{aligned}\frac{d\alpha}{dt} &= A + B\cos\alpha\sin\alpha \\ \frac{d\varepsilon}{dt} &= -B\varepsilon\cos^2\alpha.\end{aligned} \tag{5.12}$$

Several terms cancel in the first equation so there is no longer an explicit dependency on ε. The first equation can therefore be integrated directly. The second equation can then be integrated after inserting the solution for α. The result for α is

$$\alpha(t) = \begin{cases} \arctan\left(\tan\alpha_0 e^{Bt}\right) & A = 0 \\ \arctan\left(\frac{1}{2A}\left(\sqrt{4A^2 - B^2}\frac{D + \tan\left(\frac{t}{2}\sqrt{4A^2-B^2}\right)}{1 - D\tan\left(\frac{t}{2}\sqrt{4A^2-B^2}\right)} - B\right)\right) & 4A^2 > B^2 \\ \arctan\left(\frac{1}{2A}\left(\sqrt{B^2 - 4A^2}\frac{D - \tanh\left(\frac{t}{2}\sqrt{B^2-4A^2}\right)}{1 - D\tanh\left(\frac{t}{2}\sqrt{B^2-4A^2}\right)} - B\right)\right) & 4A^2 < B^2, \end{cases} \tag{5.13}$$

with

$$D = \frac{2A\tan\alpha_0 + B}{\sqrt{|4A^2 - B^2|}}.$$

$\alpha_0 = \alpha(0)$ is the starting condition. The second and third line are equal for all values of A, B and t, the piecewise definition was chosen to emphasize that the result is always real-valued. The result is continuous with respect to A and B.

For ε, the result is

$$\log\left(\frac{\varepsilon(t)}{\varepsilon_0}\right) = \frac{1}{2}\log\left(\frac{2A + B\sin(2\alpha_0)}{2A + B\sin(2\alpha)}\right) + \begin{cases} \frac{B}{\sqrt{4A^2 - B^2}}\arctan\left(\frac{\sin(\alpha_0 - \alpha)\sqrt{4A^2 - B^2}}{2A\cos(\alpha_0 - \alpha) + B\sin(\alpha_0 + \alpha)}\right) & 4A^2 > B^2 \\ \frac{B}{\sqrt{B^2 - 4A^2}}\operatorname{artanh}\left(\frac{\sin(\alpha_0 - \alpha)\sqrt{B^2 - 4A^2}}{2A\cos(\alpha_0 - \alpha) + B\sin(\alpha_0 + \alpha)}\right) & 4A^2 < B^2. \end{cases} \tag{5.14}$$

Again, the two cases are equal for all values.

Equations (5.13) and (5.14) are used in a combined χ^2-fit of α and ε data. The correlation between the errors of α and ε is neglected. Fig. 5.7 shows an example of fits to data taken at the lowest solenoid amplitude, which was achieved using the 20 dB attenuator. The effect of spin decoherence is the strongest at low amplitudes because the polarization has more time to decay before the spin is vertical again. The shape of the data is adequately reproduced by the model. The curve in α is similar to the

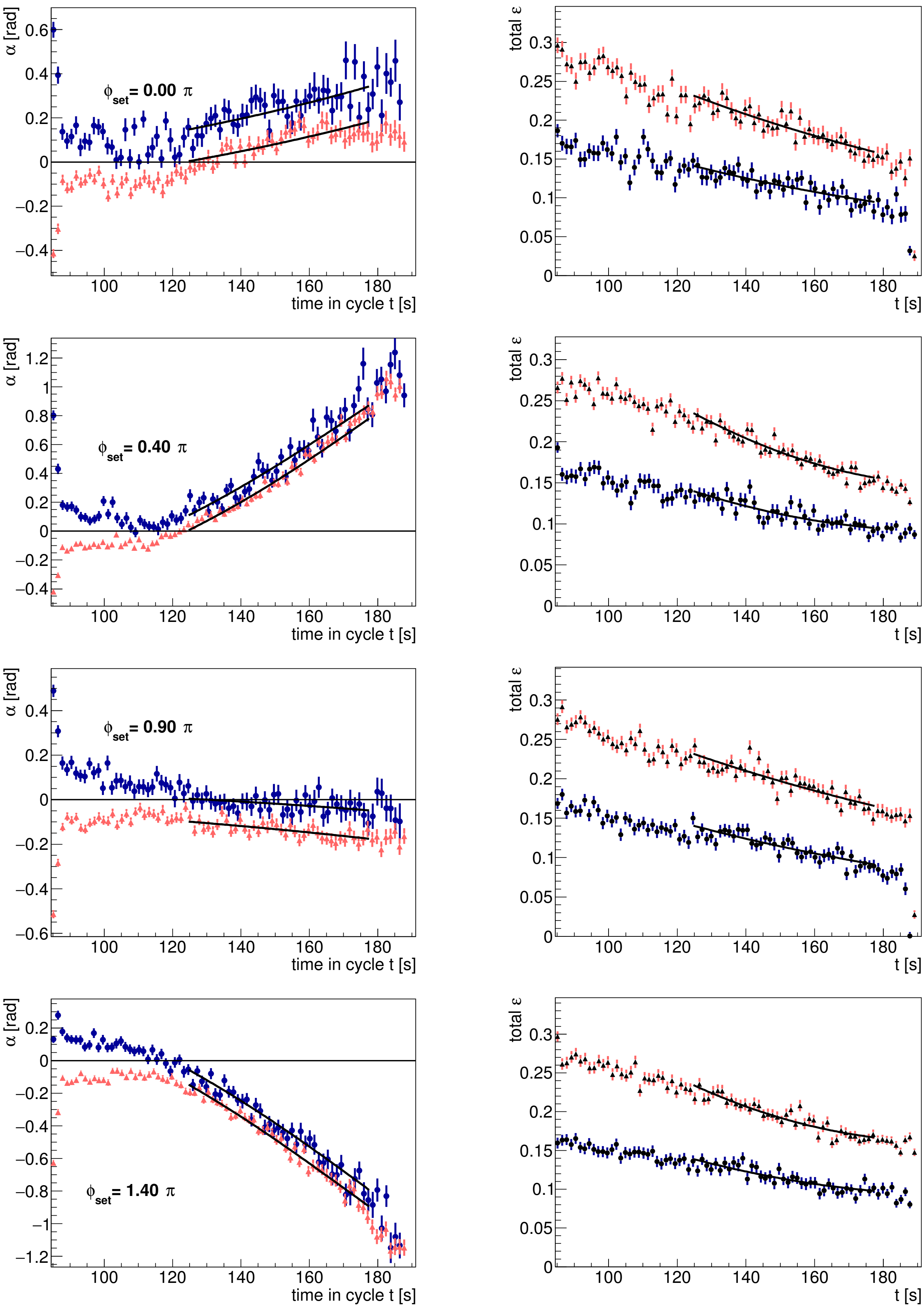

Figure 5.7.: Fit of equations (5.13) and (5.14) to data taken with the 20 dB attenuator

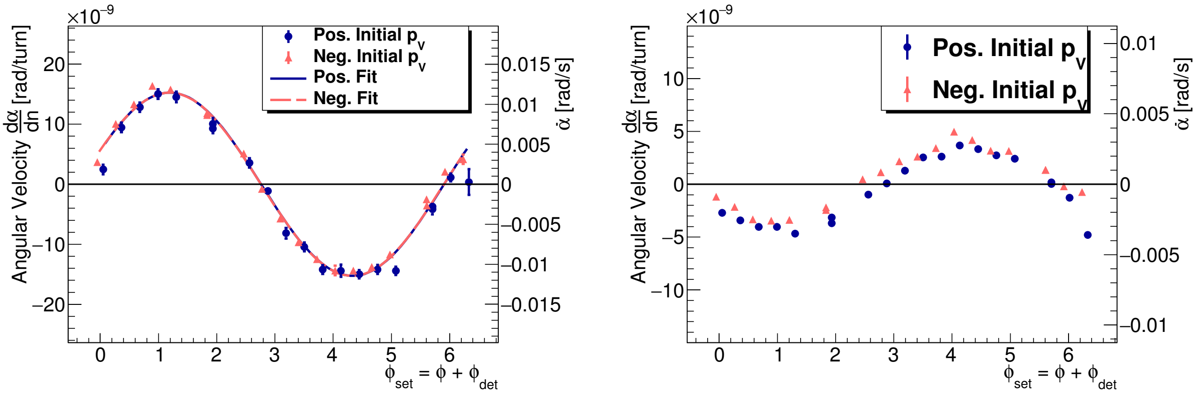

Figure 5.8.: Parameter A from the fit including spin decoherence (left) and difference to the simple fit (right)

linear model in the simple analysis, the decay of the in-plane polarization causes a small non-linearity.

Fig. 5.8 shows the solenoid-induced rotation $A \propto \sin\phi$ from the fit and the difference of the result to the simple linear model. The estimates for A including spin decoherence are smaller than the simple results by a factor in the order of 20%. This is because the simple analysis method also attributes the fake spin rotation from spin decoherence to the solenoid. The main qualitative conclusions of the simple analysis still hold for the model including spin decoherence, i.e. the feedback works as expected.

The smallest value of A found is about 15×10^{-9} rad per turn. Using the estimate of 1.6 rad per turn for $\eta = 10^{-4}$ in [1], this means that an EDM of about $5 \cdot 10^{-18}\, e\,\mathrm{cm}$ would be needed to cause the maximum rotation rate seen in fig. 5.8.

5.3. Driven Oscillations

5.3.1. Experimental Procedure

The experiments with driven spin oscillations differ from the spin build-up experiments insofar as the phase was allowed to change under the influence of the rf solenoid. As in the build-up experiments, the polarization vector is flipped into the horizontal plane using the solenoid and the feedback system is used to set the phase to a specific initial value. The solenoid is then switched on again. In contrast to the build-up experiments, the feedback system is deactivated while the solenoid is running, allowing the phase to change. This results in an oscillating motion of the polarization vector.

Spin oscillation induced by resonant rf devices have been used in experiments before and were also studied at COSY [58]. Even the initial flip into the horizontal plane can be considered a quarter period of a driven oscillation. However, the data in [58] are limited to measurements of the vertical polarization component and a single initial polarization direction.

The measurements presented here include the magnitude and phase of the in-plane polarization. By varying the initial phase, it was possible to systematically study different amplitudes of the spin oscillation, which was not possible prior to the feedback system.

5.3.2. Equation of Motion

This section and the next provide an analytical model for the spin motion in an on-resonance or off-resonance rf solenoid. A similar model for a Wien filter was independently derived in [59]. A numerical calculation based on rotation matrices is presented in [58].

The driven oscillation can be described using the coordinate system that was introduced for the build-up experiment (section 5.2.2). The angle between the polarization vector and the horizontal plane is α, the azimuth is ϕ. Unlike in section 5.2.2, ϕ is defined with respect to the longitudinal axis here, not as a relative phase. Fig. 5.9 illustrates the coordinate system and variable definitions. The z-axis points along the solenoid field, which is parallel to the beam direction, the y-axis points upward and the x-axis forms a right-handed coordinate system with the other two.

Fig. 5.9 also shows the effect of the solenoid on the phase of the beam rotation. The solenoid rotates the polarization vector about the z-axis, changing the angle α' by a constant amount each turn. If the polarization vector is not perpendicular to the beam, this also changes the value of ϕ. This way, the solenoid can advance or delay the spin precession.

The state of the polarization vector and the solenoid can be characterized by α, the spin precession phase ϕ^{spin} and the solenoid phase ϕ^{sol}. ϕ^{sol} increases every turn

$$\phi^{\text{sol}}_{n+1} = \phi^{\text{sol}}_n + 2\pi\nu^{\text{sol}}_s. \tag{5.15}$$

ν^{sol}_s is ideally equal to the spin tune in the unperturbed ring ν_s. In a real experiment, the solenoid is never perfectly on resonance, making a distinction between the phase advance per turn of the solenoid and the spin precession necessary. The difference from the perfect resonance condition is essential for describing the data, which will be shown in section 5.3.4.

The phase of the spin precession ϕ^{spin} also increases every turn, but there is an additional contribution from the solenoid.

$$\phi^{\text{spin}}_{n+1} = \phi^{\text{spin}}_n + 2\pi\nu_s + k\sin\phi^{\text{sol}}_n \frac{d\phi^{\text{spin}}}{d\alpha'} \tag{5.16}$$

k is the maximum angle by which the solenoid can rotate the polarization vector in one turn. In any given turn, the rotation is $k\sin\phi^{\text{sol}}_n$.

Finally, the evolution of α can be described by the equation

$$\alpha_{n+1} = \alpha_n + k\sin\phi^{\text{sol}}_n \frac{d\alpha}{d\alpha'}. \tag{5.17}$$

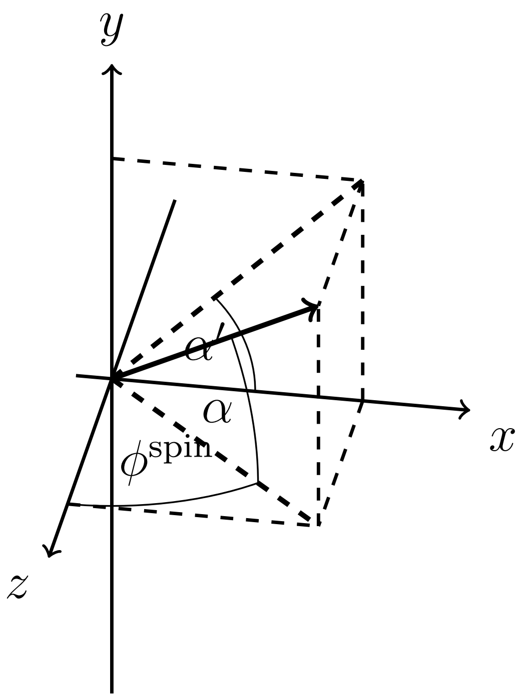

Figure 5.9.: Coordinate system describing the spin motion.

The geometrical derivatives are obtained from the definitions in fig. 5.9.

$$\begin{aligned} \frac{d\phi^{\text{spin}}}{d\alpha'} &= -\tan\alpha\cos\phi^{\text{spin}} \\ \frac{d\alpha}{d\alpha'} &= \sin\phi^{\text{spin}}. \end{aligned} \tag{5.18}$$

Equation (5.15) can be trivially integrated to $\phi_n^{\text{sol}} = 2\pi n\nu_s^{\text{sol}}$, neglecting the starting phase, which makes no substantial difference. Substituting this and (5.18) into equations (5.16) and (5.17) yields

$$\begin{aligned} \phi_{n+1}^{\text{spin}} &= \phi_n^{\text{spin}} + 2\pi\nu_s - k\sin(2\pi n\nu_s^{\text{sol}})\tan\alpha_n\cos\phi^{\text{spin}} \\ \alpha_{n+1} &= \alpha_n + k\sin(2\pi n\nu_s^{\text{sol}})\sin\phi^{\text{spin}}. \end{aligned} \tag{5.19}$$

The rapid precession of the spin is inconvenient as it happens on time scales far shorter than the polarization and spin tune measurements. All observable oscillations of the vertical polarization and the in-plane phase difference have slow frequencies in the order of kf_{COSY} while the fast oscillations are in the order of $\nu_s f_{\text{COSY}}$.

The spin oscillation has to be described using only slowly varying numbers. As ϕ^{spin} changes rapidly with time, it is substituted with the phase difference $\Delta\phi = \phi^{\text{spin}} - \phi^{\text{sol}} =$

$\phi^{\text{spin}} - 2\pi n \nu_s^{\text{sol}}$.

$$
\begin{aligned}
\Delta\phi_{n+1} &= \Delta\phi_n + 2\pi(\nu_s - \nu_s^{\text{sol}}) - k \sin(2\pi n \nu_s^{\text{sol}}) \tan\alpha_n \cos(\Delta\phi_n + 2\pi n \nu_s^{\text{sol}}) \\
\alpha_{n+1} &= \alpha_n + k \sin(2\pi n \nu_s^{\text{sol}}) \sin(\Delta\phi_n + 2\pi n \nu_s^{\text{sol}})
\end{aligned}
\tag{5.20}
$$

The trigonometric functions contain fast components, which can be replaced with their average over one period of spin precession. The time averages are

$$
\begin{aligned}
&\left\langle \sin(2\pi n \nu_s^{\text{sol}}) \cos(\Delta\phi_n + 2\pi n \nu_s^{\text{sol}}) \right\rangle \\
&= \left\langle \sin(2\pi n \nu_s^{\text{sol}}) \left(\cos\Delta\phi_n \cos(2\pi n \nu_s^{\text{sol}}) - \sin\Delta\phi_n \sin(2\pi n \nu_s^{\text{sol}}) \right) \right\rangle \\
&= \cos\Delta\phi_n \underbrace{\left\langle \cos(2\pi n \nu_s^{\text{sol}}) \sin(2\pi n \nu_s^{\text{sol}}) \right\rangle}_{=0} - \sin\Delta\phi_n \underbrace{\left\langle \sin^2(2\pi n \nu_s^{\text{sol}}) \right\rangle}_{=\frac{1}{2}} \\
&= -\frac{1}{2} \sin\Delta\phi_n
\end{aligned}
\tag{5.21}
$$

and

$$
\left\langle \sin(2\pi n \nu_s^{\text{sol}}) \sin(\Delta\phi_n + 2\pi n \nu_s^{\text{sol}}) \right\rangle = \frac{1}{2} \cos\Delta\phi_n. \tag{5.22}
$$

Inserting the time average and treating n as a continuous real number results in the equation of motion for a polarization vector in an off-resonance solenoid.

$$
\begin{aligned}
\frac{d\alpha}{dn} &= \frac{k}{2} \cos\Delta\phi \\
\frac{d\Delta\phi}{dn} &= \frac{k}{2} (\tan\alpha \sin\Delta\phi + q)
\end{aligned}
\tag{5.23}
$$

The dimensionless parameter q indicates how far the solenoid is from resonance:

$$
q = \frac{4\pi(\nu_s - \nu_s^{\text{sol}})}{k}. \tag{5.24}
$$

In the on-resonance case, q is zero.

Typical values for q are in the order of 1, positive ore negative, k was around 10^{-6} (see section 5.3.4).

Note that the phase difference $\Delta\phi$ is not equal to the ϕ used in section 5.2 and [56]. A $\Delta\phi$ of zero means that the solenoid field is zero when the polarization vector is pointing forward.

5.3.3. Solution and Properties

Equation (5.23) is a coupled system of non-linear ordinary differential equations.

The equations can be made linear using the coordinate transformation

$$\begin{aligned}
a &= \cos\alpha \cos\Delta\phi \\
b &= \frac{1}{\sqrt{1+q^2}} \left(\cos\alpha \sin\Delta\phi - q\sin\alpha\right) \\
c &= \frac{1}{\sqrt{1+q^2}} \left(q\cos\alpha \sin\Delta\phi + \sin\alpha\right).
\end{aligned} \tag{5.25}$$

This corresponds to a Cartesian coordinate system that rotates about the vertical axis with the same frequency as the solenoid. The c-axis is inclined by $\arctan q$ with respect to the vertical axis. Taking the derivatives and inserting equations (5.23) yields

$$\begin{aligned}
\frac{da}{dn} &= -\frac{k}{2}\sqrt{1+q^2}c \\
\frac{db}{dn} &= 0 \\
\frac{dc}{dn} &= \frac{k}{2}\sqrt{1+q^2}a.
\end{aligned} \tag{5.26}$$

This system has the trivial solution

$$\begin{aligned}
a &= C_1 \cos\left(\frac{kn}{2}\sqrt{1+q^2} + C_2\right) \\
b &= C_3 \\
c &= C_1 \sin\left(\frac{kn}{2}\sqrt{1+q^2} + C_2\right),
\end{aligned} \tag{5.27}$$

with arbitrary constants C_1, C_2, C_3.

The solution [60] to the equations is found by solving the above for α and $\Delta\phi$ and choosing the constants to match the given initial conditions α_0 and $\Delta\phi_0$.

$$\begin{aligned}
\sin\alpha(n) &= A_1 \sin\left(A_2 + nA_3\right) - A_4 \\
\cos\Delta\phi(n) &= \frac{A_1\sqrt{1+q^2}\cos\left(A_2 + nA_3\right)}{\sqrt{1-\left(A_1\sin\left(A_2+nA_3\right) - A_4\right)^2}} \\
\sin\Delta\phi(n) &= \frac{C + q\sin\alpha}{\cos\alpha},
\end{aligned} \tag{5.28}$$

with the parameters

$$
\begin{aligned}
A_1 &= \frac{\sqrt{1+q^2-C^2}}{1+q^2} \\
A_2 &= \begin{cases} \arcsin\left(\dfrac{\sin\alpha_0 + A_4}{A_1}\right) & |\Delta\phi_0| < \pi/2 \\[2ex] \pi - \arcsin\left(\dfrac{\sin\alpha_0 + A_4}{A_1}\right) & |\Delta\phi_0| > \pi/2 \end{cases} \\
A_3 &= \frac{k}{2}\sqrt{1+q^2} \\
A_4 &= \frac{Cq}{1+q^2}.
\end{aligned}
\tag{5.29}
$$

and

$$
C = \cos\alpha \sin\Delta\phi - q\sin\alpha, \tag{5.30}
$$

which is conserved. The values of C and $\sqrt{1+q^2}$ in (5.28) are not independent but functions of A_1 and A_4.

$$
\begin{aligned}
1+q^2 &= \frac{1+A_1^2-A_4^2}{2A_1^2} \pm \sqrt{\left(\frac{1+A_1^2-A_4^2}{2A_1^2}\right)^2 - \frac{1}{A_1^2}} \\
C &= \frac{1+q^2}{q} A_4
\end{aligned}
\tag{5.31}
$$

As α is by definition between $-\pi/2$ and $\pi/2$, it is equal to $\arcsin(\sin\alpha)$. $\Delta\phi$ can be computed using $\operatorname{arctan2}(\sin\Delta\phi, \cos\Delta\phi)$. The plus sign in equation (5.31) corresponds to unbound solutions, the minus sign to bound ones (defined below).

Fig. 5.10 shows the solution for the on-resonance case, in which q is zero, for a range of initial phases. α_0 is set to zero, matching the initial conditions in the experiment, where the polarization vector was initially horizontal. A nonzero α_0 leads to a similar result, at a larger amplitude and shifted along the x-axis. For both the on-resonance and the off-resonance case, the equations are symmetric under the transformation $\Delta\phi \to \Delta\phi + \pi$ and $\alpha \to -\alpha$. Only solutions for $|\Delta\phi_0| > \pi/2$ are plotted, the remaining ones, can be obtained by this transformation.

For an on-resonance solenoid, the amplitudes of the oscillation in α and $\Delta\phi$ are equal. α oscillates around zero, $\Delta\phi$ oscillates around $\pm\pi/2$. $\Delta\phi$ reaches its maximum and minimum when α is zero.

Fig. 5.11 shows the solution for an off-resonance solenoid. The polarization vector now oscillates around a stable position at $\alpha = \pm\arctan q$ and $\Delta\phi = \mp\pi/2$.

The most obvious difference from the on-resonance case is that there are now some solutions in which $\Delta\phi$ moves over the complete range from $-\pi$ to π. In the on-resonance

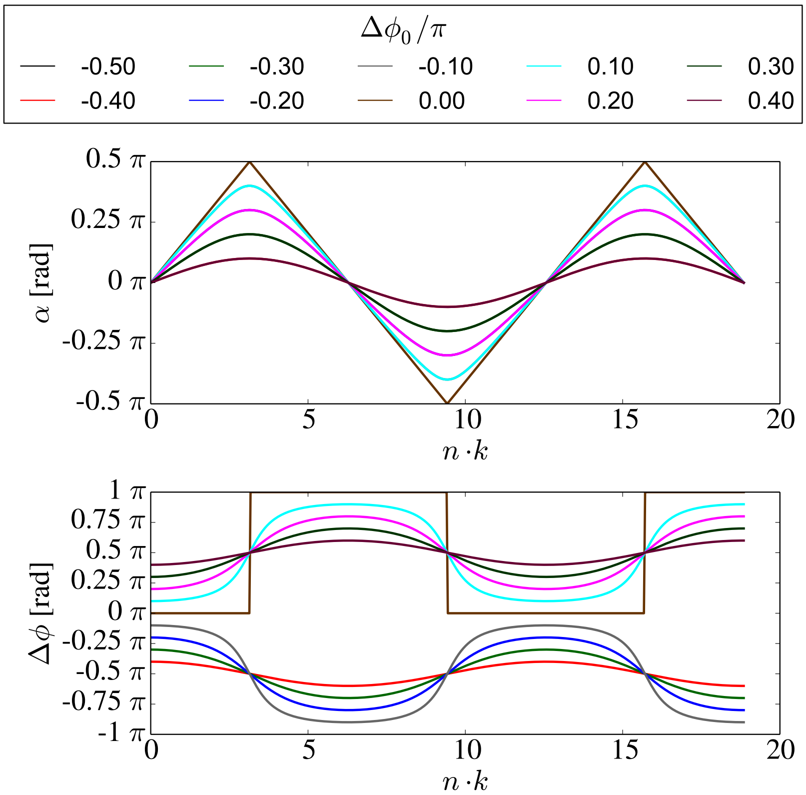

Figure 5.10.: Solution for α and $\Delta\phi$ on resonance, i.e. $q = 0$. In this special case, the sign of $\Delta\phi$ does not change α.

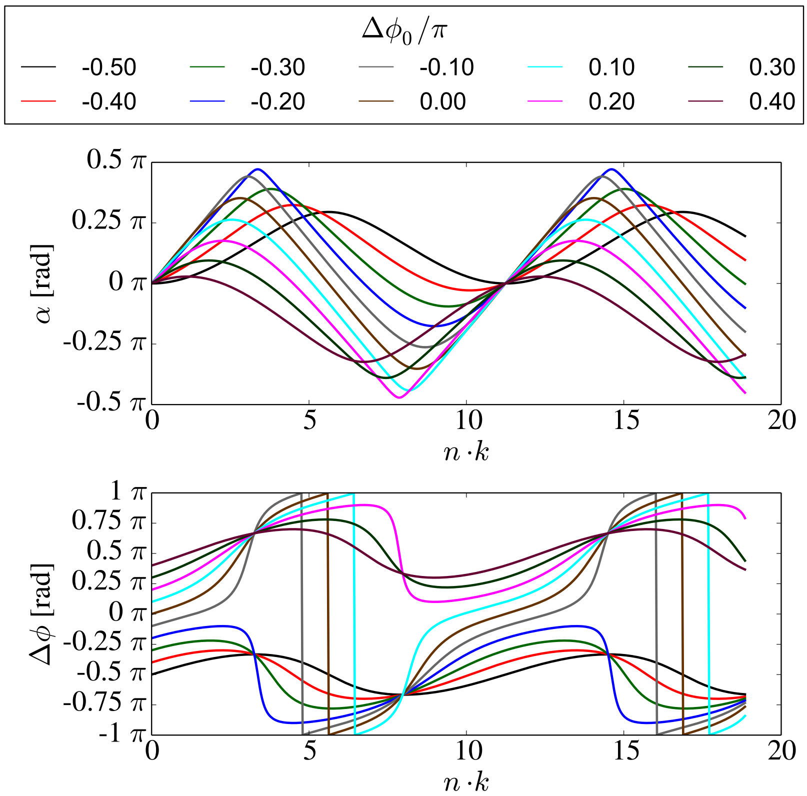

Figure 5.11.: Solution for the off-resonance case with $q = 0.5$

case, $\Delta\phi$ is always constrained to negative or positive values. It is easy to see that, if the frequency is sufficiently different from the resonance, $\Delta\phi$ must behave this way because there is no longer a fixed phase relation between the spin precession and the solenoid field. Solutions in which $\Delta\phi$ remains either positive or negative will henceforth be referred to as bound solutions, solutions in which $\Delta\phi$ varies over the entire angular range will be referred to as unbound.

The oscillation frequency for off-resonance solenoids is higher than in the on-resonance case.

The separatrix between bound and unbound solutions can be found by examining (5.23). In a bound solution, there must be extreme points in $\Delta\phi$, at which the derivative vanishes.

$$\begin{aligned} 0 &= \frac{k}{2}\left(\tan\alpha \sin\Delta\phi + q\right) \\ \iff \sin\Delta\phi &= \frac{-q}{\tan\alpha} \end{aligned} \tag{5.32}$$

Eliminating $\sin\Delta\phi$ using (5.30) yields

$$-q = C\sin\alpha. \tag{5.33}$$

The largest value for which this equation has solutions is $|C| = |q|$. For $|C| < |q|$, there can be no extreme points in $\Delta\phi$, so the solution must be unbound.

The effect of the solenoid on $\Delta\phi$ can also be interpreted as a modulation of the spin tune. An effective spin tune can be defined as

$$\begin{aligned} \nu_s^{\text{eff}} &= \frac{1}{2\pi\Delta n}\left(\phi_{n+\Delta n}^{\text{spin}} - \phi_n^{\text{spin}}\right) \\ &= \frac{1}{2\pi\Delta n}\left(\Delta\phi_{n+\Delta n} - \Delta\phi_n + 2\pi\nu_s\Delta n\right) \\ &\xrightarrow[\Delta n\to 0]{} \frac{1}{2\pi}\frac{d\Delta\phi}{dn} + \nu_s. \end{aligned} \tag{5.34}$$

In the determination of the spin tune as described in section 3.2.2, this effect is visible as an oscillation in the phase of the sine fit $\tilde{\phi}$, which is shown in fig. 5.12. $\tilde{\phi}$ is equal to $\Delta\phi$ plus an offset plus a linear term from the difference of the assumed spin tune ν_s^{fix} and the actual value ν_s.

An interesting special case of the solution is the initial spin flip from $\alpha = \pm\pi/2$ to zero, which is shown in fig. 5.13. The apparent discontinuity in $\Delta\phi$ is due to moving the spin through the pole of the unit sphere, the Cartesian components of the polarization vectors are continuous.

For the same reason, the initial phase is meaningless in this case. After the solenoid is switched on, $\Delta\phi$ will jump to zero.

The maximum possible flip angle depends on how well the frequencies are matched. For a negative initial polarization the maximum angle is

$$\alpha_{\max} = \frac{1-q^2}{1+q^2}. \tag{5.35}$$

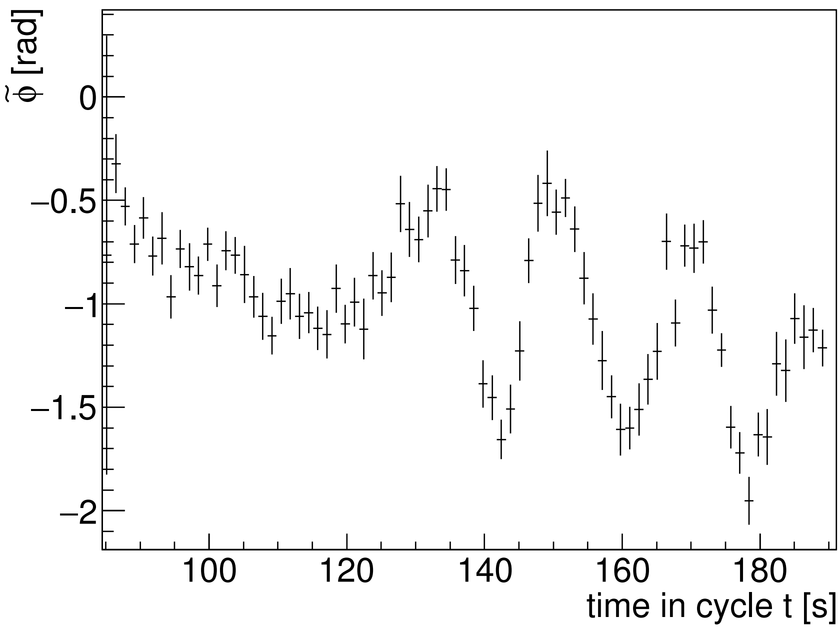

Figure 5.12.: Spin tune algorithm with active solenoid. Without a solenoid, the phase over time shows a low drift, compare [46, fig. 3].

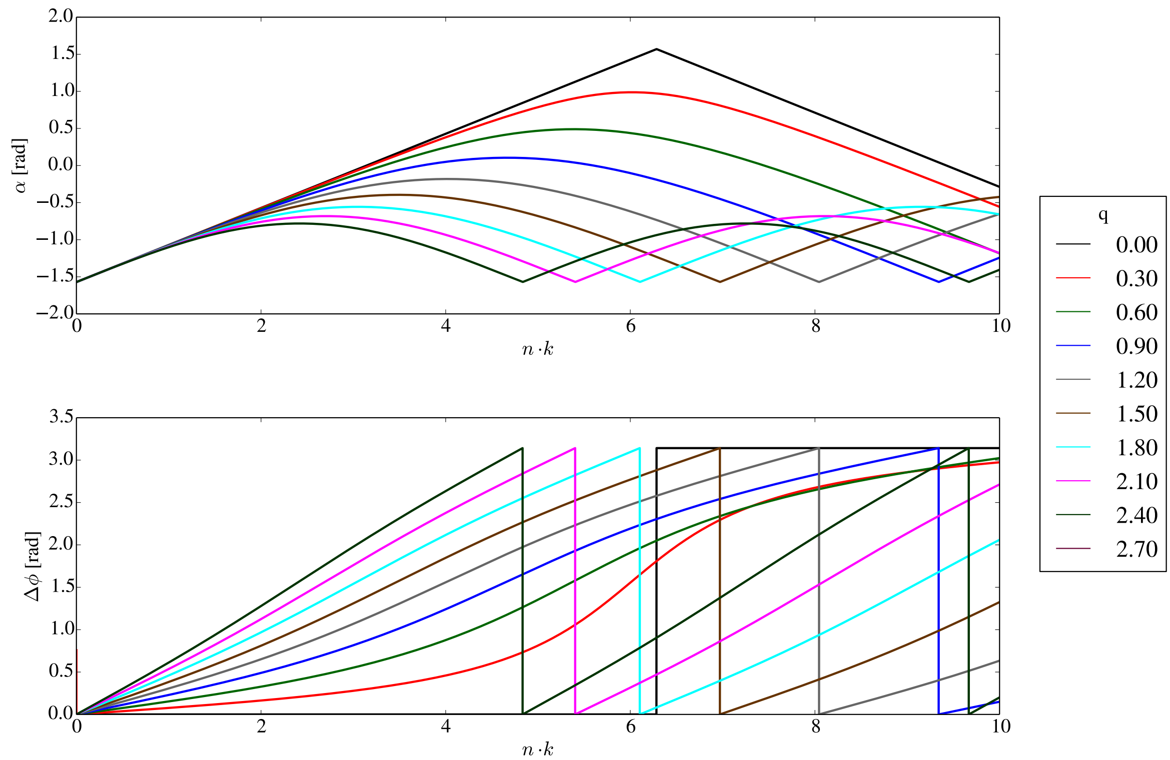

Figure 5.13.: Spin flip from vertical to horizontal

For positive initial polarization, the sign is reversed.

5.3.4. Fits

The model of the previous sections is fitted to the measurements using a combined χ^2-minimization of α and $\Delta\phi$ data. α can be directly calculated using its definition and the vertical and horizontal rate asymmetries.

The software used in the feedback system itself calculates $\Delta\phi$ by direct subtraction of the solenoid and the spin precession phase. The disadvantage of this method is that it assumes a certain spin tune that cancels in the final result, making the process more opaque. For the off-line analysis, a different algorithm is used, which works by examining the event rates in the polarimeter as a function of the solenoid phase.

The solenoid phase can be obtained in a way similar to the calculation of the turn number. The prescaled signal from the solenoid is measured using the same time marking system as the polarimeter data. For every event, the phase of the solenoid at that time can be calculated from the last registered solenoid time and the known solenoid frequency.

The events from each direction in the polarimeter are filled into separate two-dimensional histograms of the turn number and the solenoid phase (fig. 5.14). The rates in the top and bottom quadrants are modulated by the in-plane polarization.

Fig. 5.15 shows the bin-by-bin asymmetry between the top and the bottom detector, which is proportional to the radial polarization component. Within each turn number bin, the time scale is short enough to treat the spin tune and $\Delta\phi$ as constants. The histogram is sliced along the x-axis, producing a one-dimensional histogram of solenoid phases for each turn number bin. A sine with a variable starting phase and amplitude is fitted to the solenoid phase distribution of each slice. The starting phase of that sine is $\Delta\phi$. This result still has to be corrected offset of ϕ_{det}, which is known from the spin build-up experiments.

Equations (5.28) are then fitted to the resulting curves for α and $\Delta\phi$. The parameters for the fit are A_1 to A_4, which are more numerically stable than k, q, α_0 and $\Delta\phi_0$. The χ^2-value is added over both the α and $\Delta\phi$ data. For $\Delta\phi$, the difference between data and model is calculated as the shorter of the two possible ways to measure around the unit circle. For example, the difference between $-\pi$ and π is zero and not 2π. Probability distributions in angles can be treated more rigorously using directional statistics, but the approximation used here is adequate for uncertainties much smaller that 2π.

The model is in good agreement with the data. Unbound solutions were observed in addition to oscillations around both $+\pi/2$ and $-\pi/2$. As the amplitude increases, the extrema in α become sharper while the extrema in $\Delta\phi$ become flatter, matching the model expectation. Fig. 5.17 shows bound oscillations of α and $\Delta\phi$ at different amplitudes.

Fig. 5.18 shows unbound oscillations, which are also described well by the model. Fig. 5.19 shows a cycle during which there was a transition between bound and unbound behavior, probably because of some perturbation which is not included in the model.

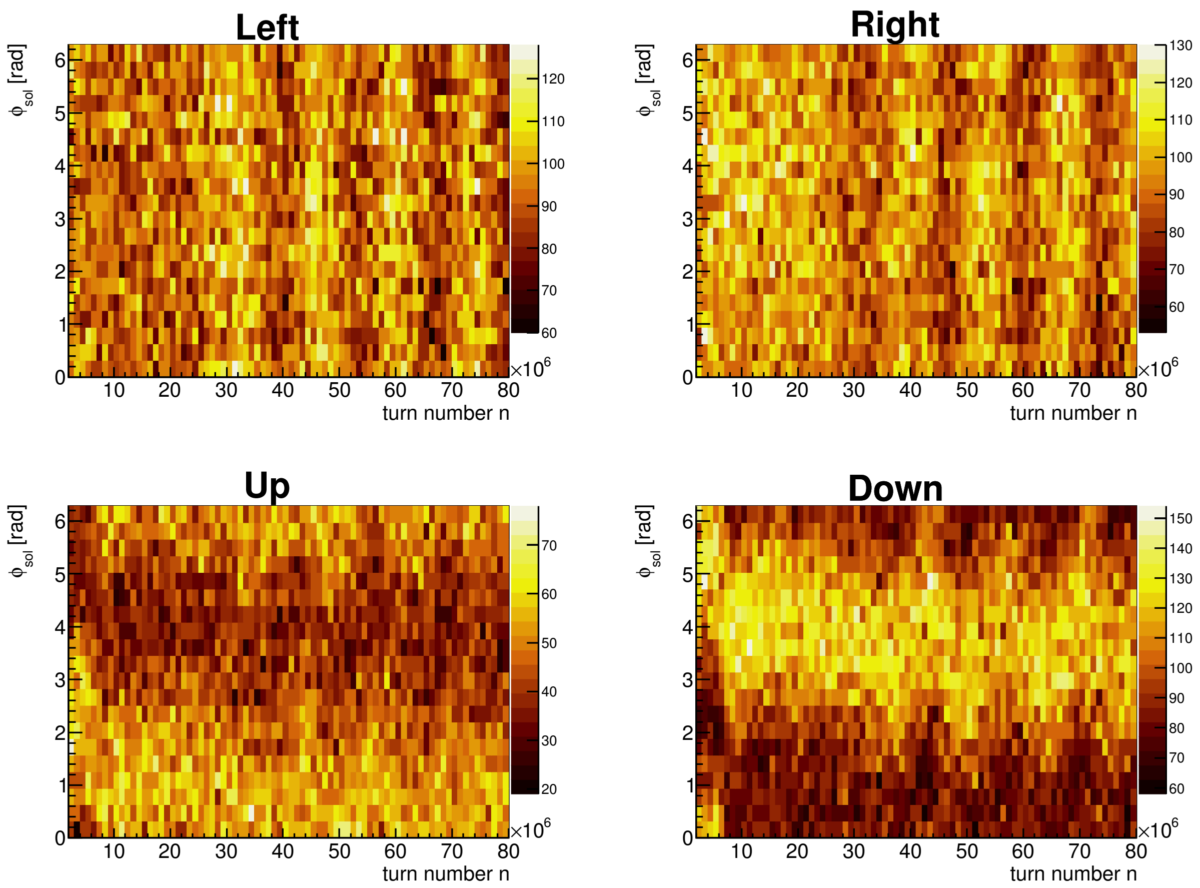

Figure 5.14.: Distribution of the turn number and solenoid phase for the four quadrants of the polarimeter

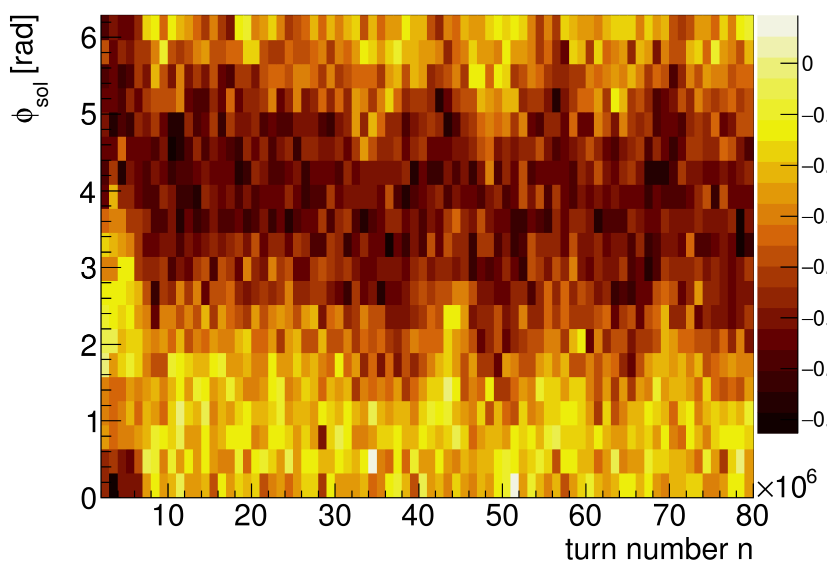

Figure 5.15.: Up-down asymmetry as a function of the turn number and the solenoid phase

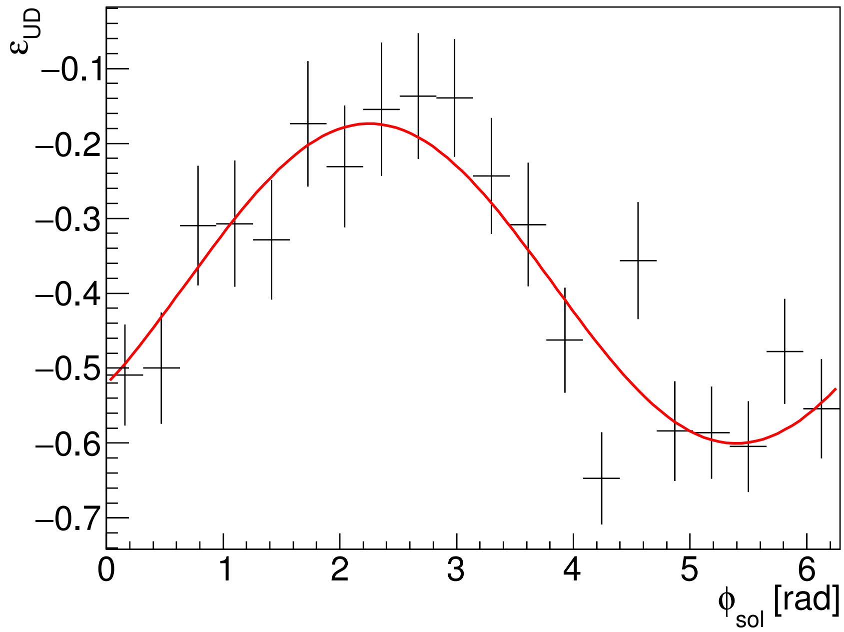

Figure 5.16.: Fit to the fifths bin in fig. 5.15

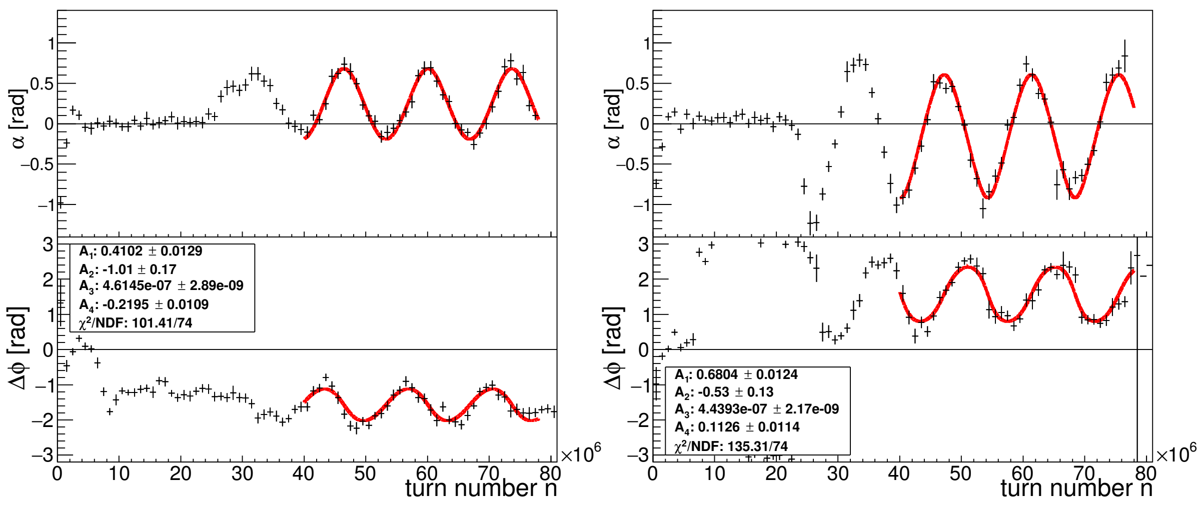

Figure 5.17.: Bound oscillations of α and $\Delta\phi$

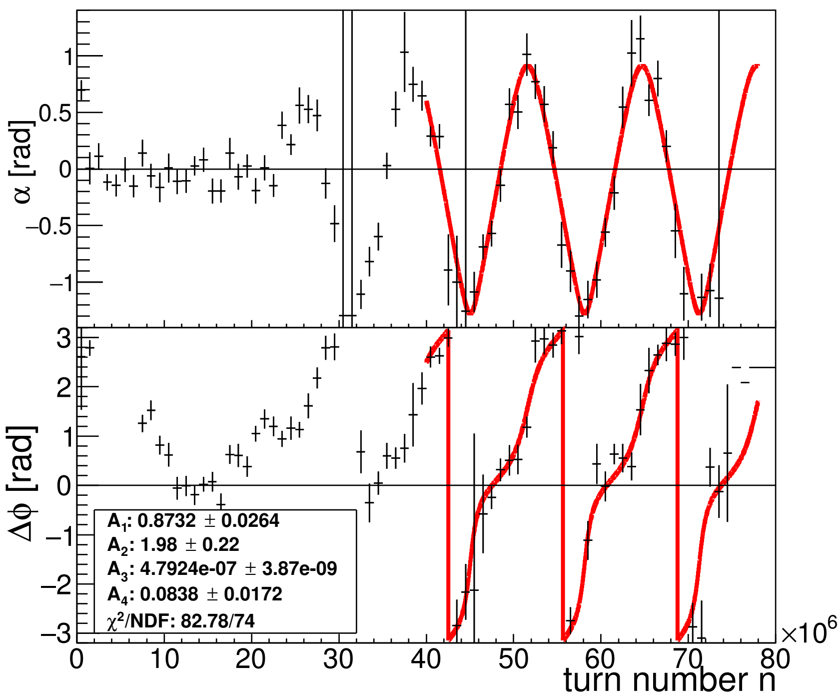

Figure 5.18.: Unbound oscillations

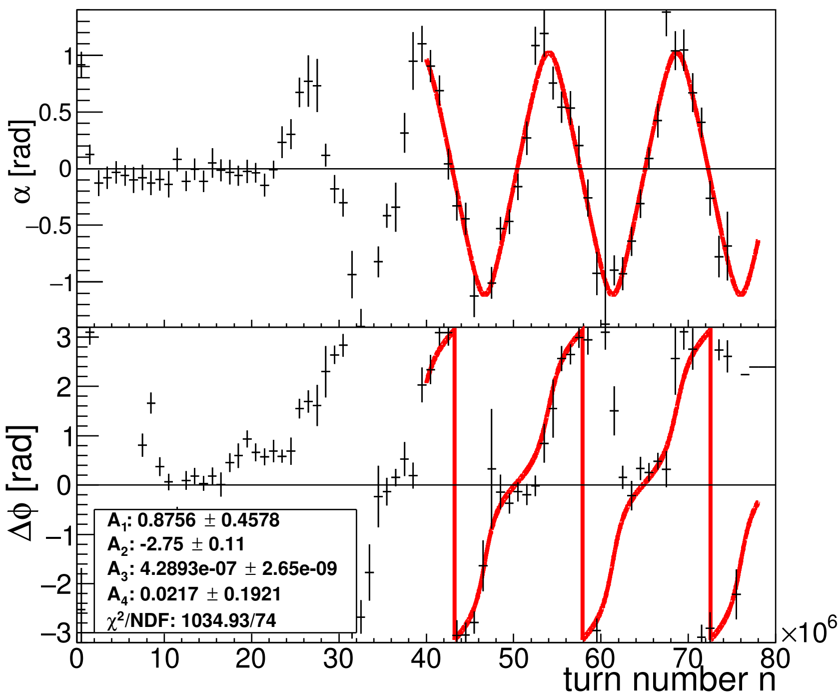

Figure 5.19.: Oscillation that goes from bound to unbound behavior during one cycle

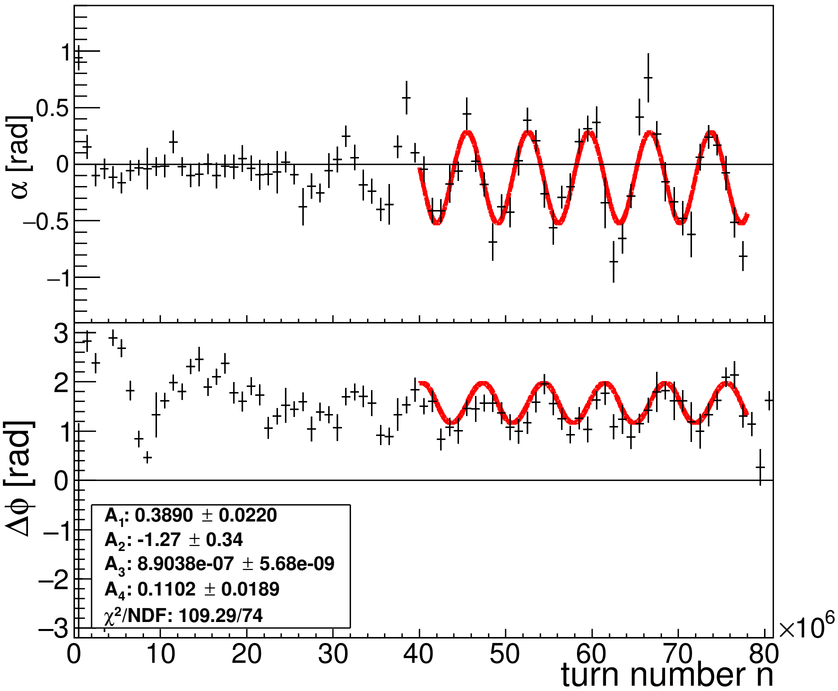

Figure 5.20.: Bound oscillations at a higher solenoid amplitude

Fig. 5.20 shows bound oscillations at a higher solenoid amplitude, which resulted in a increased frequency.

It is clear from the data that the spin tune mismatch q has to be included in the model to find an adequate description. Oscillations in α around nonzero values and unbound behavior could not be explained otherwise.

5.4. Outlook

The feedback system was demonstrated to work and will be available for future experiments. A Wien filter for COSY is under development [57] and will be used in combination with the feedback system to find a limit for the deuteron EDM in a precursor experiment at COSY.

The model for the influence of spin decoherence on the build-up of vertical polarization can be used for EDM measurements as well. In an EDM measurement, the length of one cycle will be in the order of 1000 s and the build-up rate will be small. The contribution of spin decoherence to the vertical polarization build-up could be estimated using the same method.

Oscillations of the vertical polarization can also be observed under the influence of an rf Wien filter with a radial magnetic field, which was demonstrated at COSY in 2014 [61]. In EDM measurements using the Wien filter method, the magnetic field will be vertical. However, the Wien filter that is being developed for tests at COSY can be rotated by 90° about the beam axis, allowing operation with a radial magnetic field [57].

The oscillation induced by a Wien filter is very similar to the oscillation from a solenoid. The main difference is that the solenoid rotates the polarization about the beam axis while the Wien filter rotates it about the radial axis. This is equivalent to a rotation of the coordinate system in fig. 5.9 about the vertical axis by 90°. The relevant equations are still the same.

In the experiments with the new Wien filter, measurements with a radial magnetic field will be used for fine tuning the apparatus [57]. The model of the spin precession could help to find the optimal settings, for example by estimating how far the Wien filter is from the resonance condition.

The model for the spin oscillations induced by a solenoid only uses a single particle with a fixed spin tune rather than an ensemble of particles. A more general model for an ensemble could describe effects of spin decoherence and maybe the transient state immediately after the solenoid is switched on.

As spin decoherence results from the different spin in the beam precessing at different rates, the induced oscillation could increase the coherence time. Without the solenoid, the phases of particles with a spin tune difference $\Delta\nu^s \propto \Delta q$ drift apart at a rate proportional to the difference. During oscillation, both spin phases oscillate around the solenoid phase at frequencies proportional to $\sqrt{1+q^2}$, which depends more weakly on the spin tune difference.

6. Conclusion

This thesis consists of two parts dealing with different studies in preparation for EDM measurements at a storage ring: the replacement of the Low Energy Polarimeter read-out electronics and the analysis of feedback system data.

The new read-out electronics for the Low Energy Polarimeter has been used successfully since the beam time in spring 2015. It is now the routine tool for setting up the polarized source and monitoring its performance during experiments with polarized beams. Measurements of both amplitude spectra and kinematic coincidences, which were already possible with the previous read-out system, were replicated using the new hardware. In addition to the old capabilities, the new read-out system is able to measure the time between an event and the last maximum of the cyclotron rf voltage, which is closely related to the time of flight of the particle.

Event rates for energy spectrum measurements could be increased from about 10 kHz to values from 30 kHz up to 150 kHz depending on the scattering angle, leading to a proportionately shorter measurement time. Unlike the old system, which only recorded event rates, the new read-out records the times and amplitudes of all pulses, showing shifts in the amplitude spectra and facilitating an offline data analysis.

The setup of polarization measurements could be simplified significantly compared to the previous read-out system. The new system is integrated into the COSY network and can be operated remotely via ssh.

The second part of the thesis, the development of the active feedback system for the precession of the in-plane polarization, is a major step towards an EDM precursor experiment at COSY. A measurement of the relative phase between the 120 kHz precession and the solenoid frequency shows that the phase can be kept constant within a standard deviation of 0.21 rad. This was also verified by measuring the build-up rate of vertical polarization under the influence of the rf solenoid, which is roughly proportional to the sine of the phase difference. The analysis also takes the effect of spin decoherence into account. The vertical polarization build-up is similar to the effect of an EDM, which also tilts the polarization vector out of the horizontal plane. Future EDM data could be analyzed using similar methods. In the EDM precursor experiments at COSY, a Wien filter will be used in combination with the feedback system.

A resonant oscillation of the vertical polarization component induced by the solenoid was also examined using the feedback system. For the first time, the phase and magnitude of the in-plane polarization were measured in addition to the vertical polarization. The resulting data could be described using an analytical model, which might be useful in later experiments using rf devices.

A. List of Runs for the Vertical Build-Up Experiment

Table A.1.: Build-up with RF amplitude 0.001, first series of measurements.

Run Nr.	Date	Start Time	End Time	ϕ_{set}/π
6637	2015-12-11	21:05	21:28	0.50
6640	2015-12-11	22:16	22:38	0.00
6641	2015-12-11	22:42	23:06	0.25
6644	2015-12-12	00:07	00:36	0.75
6645	2015-12-12	00:36	01:00	1.00
6646	2015-12-12	01:01	01:24	1.25
6648	2015-12-12	01:38	02:06	1.50
6649	2015-12-12	02:08	02:32	1.75
6651	2015-12-12	03:06	03:31	2.00

Table A.2.: Build-up with RF amplitude 0.001, second series of measurements.

Run Nr.	Date	Start Time	End Time	ϕ_{set}/π
6687	2015-12-12	23:47	00:10	0.00
6688	2015-12-13	00:12	00:35	0.20
6689	2015-12-13	00:37	01:00	0.40
6691	2015-12-13	01:11	01:36	0.60
6692	2015-12-13	01:38	02:01	1.80
6693	2015-12-13	02:03	02:27	1.00
6694	2015-12-13	02:29	02:51	1.40
6695	2015-12-13	02:53	03:16	0.80
6700	2015-12-13	03:50	04:13	1.60
6702	2015-12-13	04:33	04:55	1.20

Table A.3.: Build-up with a new RF amplifier and amplitude set to 0.01.

Run Nr.	Date	Start Time	End Time	ϕ_{set}/π
6782	2015-12-14	18:15	18:36	1.40
6784	2015-12-14	19:17	19:41	1.00
6785	2015-12-14	19:46	20:10	0.00
6786	2015-12-14	20:13	20:35	2.00
6787	2015-12-14	20:35	20:59	0.80
6788	2015-12-14	21:02	21:24	1.80
6789	2015-12-14	21:25	21:49	0.20
6790	2015-12-14	21:51	22:14	1.60
6793	2015-12-14	22:35	22:58	0.60
6794	2015-12-14	23:10	23:33	1.20

Table A.4.: Build-up with a new RF amplifier and amplitude set to 0.005.

Run Nr.	Date	Start Time	End Time	ϕ_{set}/π
6796	2015-12-14	00:13	00:45	1.60
6797	2015-12-15	00:59	01:24	1.80
6800	2015-12-15	01:46	02:03	2.00
6801	2015-12-15	02:09	02:31	2.00
6802	2015-12-15	02:35	03:01	1.40
6803	2015-12-15	03:03	03:24	1.20
6804	2015-12-15	03:27	03:50	1.00
6805	2015-12-15	03:51	04:15	0.80
6808	2015-12-15	04:35	04:56	0.60
6812	2015-12-15	05:02	05:26	0.40
6813	2015-12-15	05:27	06:01	0.20
6814	2015-12-15	06:03	06:27	0.00
6815	2015-12-15	06:28	06:52	1.60

Table A.5.: Build-up with 20 dB attenuator for the RF signal.

Run Nr.	Date	Start Time	End Time	ϕ_{set}/π
6837	2015-12-15	23:38	00:23	0.10
6838	2015-12-16	00:25	01:11	0.20
6840	2015-12-16	01:14	02:05	0.30
6843	2015-12-16	02:23	03:09	0.40
6846	2015-12-16	04:02	04:47	0.60
6852	2015-12-16	06:36	07:24	0.90
6855	2015-12-16	07:33	08:30	1.00
6856	2015-12-16	08:33	09:20	1.10
6858	2015-12-16	10:08	10:53	1.20
6861	2015-12-16	11:32	11:53	1.30
6863	2015-12-16	11:58	12:45	1.40
6864	2015-12-16	12:47	13:28	1.50
6865	2015-12-16	13:30	–	1.60
6870	2015-12-16	15:44	16:23	1.80
6871	2015-12-16	16:25	17:10	1.90
6882	2015-12-16	21:11	21:27	2.00
6885	2015-12-16	22:02	22:46	1.80
6894	2015-12-16	02:19	03:05	0.80
6895	2015-12-16	03:06	03:51	0.60
6899	2015-12-16	05:40	06:25	0.00

B. List of Runs for the Oscillation Experiment

Table B.1.: Build-up with RF amplitude 0.001, first series of measurements.

Run Nr.	Date	Start Time	End Time	ϕ_{set}/π	Amplpitude
6739	2015-12-13	21:27	–	1.00	0.03
6740	2015-12-13	21:47	–	1.00	0.05
6741	2015-12-13	21:59	–	1.87	0.05
6742	2015-12-13	22:14	–	1.87	0.10
6743	2015-12-13	22:34	–	0.86	0.01
6744	2015-12-13	23:13	23:36	0.00	0.05
6745	2015-12-13	23:45	00:07	0.20	0.05
6746	2015-12-14	00:12	00:36	0.40	0.05
6747	2015-12-14	00:45	01:08	0.60	0.05
6748	2015-12-14	01:14	01:37	0.80	0.05
6749	2015-12-14	01:40	02:03	1.00	0.05
6750	2015-12-14	02:05	02:27	1.20	0.05
6751	2015-12-14	02:27	02:52	1.40	0.05
6753	2015-12-14	04:36	04:58	1.60	0.05
6754	2015-12-14	05:00	05:24	1.80	0.05
6755	2015-12-14	05:25	05:47	2.00	0.05

Bibliography

[1] M. Rosenthal. "Experimental Benchmarking of Spin Tracking Algorithms for Electric Dipole Moment Searches at the Cooler Synchrotron COSY". PhD thesis. RWTH Aachen Univerits, 2016.

[2] Jörg Pretz. "Measurement of permanent electric dipole moments of charged hadrons in storage rings". In: *Hyperfine Interactions* 214.1 (2013), pp. 111–117. ISSN: 1572-9540. DOI: 10.1007/s10751-013-0799-4. URL: http://dx.doi.org/10.1007/s10751-013-0799-4.

[3] C. S. Wu et al. "Experimental Test of Parity Conservation in Beta Decay". In: *Phys. Rev.* 105 (4 1957), pp. 1413–1415. DOI: 10.1103/PhysRev.105.1413. URL: https://link.aps.org/doi/10.1103/PhysRev.105.1413.

[4] C. Patrignani et al. "Review of Particle Physics". In: *Chin. Phys.* C40.10 (2016), p. 100001. DOI: 10.1088/1674-1137/40/10/100001.

[5] Planck Collaboration et al. "Planck 2013 results. XVI. Cosmological parameters". In: *A&A* 571 (2014), A16. DOI: 10.1051/0004-6361/201321591. URL: https://doi.org/10.1051/0004-6361/201321591.

[6] A. D. Sakharov. "SPECIAL ISSUE: Violation of CP in variance, C asymmetry, and baryon asymmetry of the universe". In: *Soviet Physics Uspekhi* 34 (May 1991), pp. 392–393. DOI: 10.1070/PU1991v034n05ABEH002497.

[7] Patrick Huet and Eric Sather. "Electroweak baryogenesis and standard model CP violation". In: *Phys. Rev. D* 51 (2 1995), pp. 379–394. DOI: 10.1103/PhysRevD.51.379. URL: https://link.aps.org/doi/10.1103/PhysRevD.51.379.

[8] J. H. Christenson et al. "Evidence for the 2π Decay of the K_2^0 Meson". In: *Phys. Rev. Lett.* 13 (4 1964), pp. 138–140. DOI: 10.1103/PhysRevLett.13.138. URL: https://link.aps.org/doi/10.1103/PhysRevLett.13.138.

[9] "Theory and Phenomenology of CP Violation". In: *Nuclear Physics B - Proceedings Supplements* 167 (2007), pp. 170 –174. ISSN: 0920-5632. DOI: http://dx.doi.org/10.1016/j.nuclphysbps.2006.12.083. URL: http://www.sciencedirect.com/science/article/pii/S0920563206010711.

[10] Makoto Kobayashi and Toshihide Maskawa. "CP-Violation in the Renormalizable Theory of Weak Interaction". In: *Progress of Theoretical Physics* 49.2 (1973), p. 652. DOI: 10.1143/PTP.49.652. eprint: /oup/backfile/content_public/journal/ptp/49/2/10.1143/ptp.49.652/2/49-2-652.pdf. URL: +http://dx.doi.org/10.1143/PTP.49.652.

[11] W. Dekens et al. "Unraveling models of CP violation through electric dipole moments of light nuclei". In: *Journal of High Energy Physics* 2014.7 (2014), p. 69. ISSN: 1029-8479. DOI: 10.1007/JHEP07(2014)069. URL: http://dx.doi.org/10.1007/JHEP07(2014)069.

[12] R.J. Crewther et al. "Chiral estimate of the electric dipole moment of the neutron in quantum chromodynamics". In: *Physics Letters B* 88.1 (1979), pp. 123 –127. ISSN: 0370-2693. DOI: http://dx.doi.org/10.1016/0370-2693(79)90128-X. URL: http://www.sciencedirect.com/science/article/pii/037026937990128X.

[13] N. F. Ramsey and A. Weis. "Suche nach permanenten elektrischen Dipolmomenten: ein Test der Zeitumkehrinvarianz". In: *Physik Journal* 52.9 (1996), pp. 859–863. ISSN: 1521-3722. DOI: 10.1002/phbl.19960520906. URL: http://dx.doi.org/10.1002/phbl.19960520906.

[14] Wikipedia. *Neutron electric dipole moment — Wikipedia, The Free Encyclopedia*. [Online; accessed 5-May-2017]. 2017. URL: https://en.wikipedia.org/w/index.php?title=Neutron_electric_dipole_moment&oldid=778137321.

[15] J. Baron et al. "Order of Magnitude Smaller Limit on the Electric Dipole Moment of the Electron". In: *Science* 343.6168 (2014), pp. 269–272. ISSN: 0036-8075. DOI: 10.1126/science.1248213. eprint: http://science.sciencemag.org/content/343/6168/269.full.pdf. URL: http://science.sciencemag.org/content/343/6168/269.

[16] C. A. Baker et al. "Improved Experimental Limit on the Electric Dipole Moment of the Neutron". In: *Phys. Rev. Lett.* 97 (13 2006), p. 131801. DOI: 10.1103/PhysRevLett.97.131801. URL: https://link.aps.org/doi/10.1103/PhysRevLett.97.131801.

[17] V. A. Dzuba, V. V. Flambaum, and S. G. Porsev. "Calculation of (P, T)-odd electric dipole moments for the diamagnetic atoms ^{129}Xe, ^{171}Yb, ^{199}Hg, ^{211}Rn, and ^{225}Ra". In: *Phys. Rev. A* 80 (3 2009), p. 032120. DOI: 10.1103/PhysRevA.80.032120. URL: https://link.aps.org/doi/10.1103/PhysRevA.80.032120.

[18] J.M. Pendlebury and E.A. Hinds. "Particle electric dipole moments". In: *Nuclear Instruments and Methods in Physics Research Section A: Accelerators, Spectrometers, Detectors and Associated Equipment* 440.3 (2000), pp. 471 –478. ISSN: 0168-9002. DOI: https://doi.org/10.1016/S0168-9002(99)01023-2. URL: http://www.sciencedirect.com/science/article/pii/S0168900299010232.

[19] Takeshi Fukuyama. "Searching for New Physics Beyond the Standard Model in Electric Dipole Moment". In: *International Journal of Modern Physics A* 27.16 (2012), p. 1230015. DOI: 10.1142/S0217751X12300153. eprint: http://www.worldscientific.com/doi/pdf/10.1142/S0217751X12300153. URL: http://www.worldscientific.com/doi/abs/10.1142/S0217751X12300153.

[20] *Einführung in die Kernphysik mit polarisierten Teilchen*. Bibliographisches Institut Mannheim/Wien/Zürich, 1971.

[21] S. R. Mane, Yu. M. Shatunov, and K. Yokoya. “Spin-polarized charged particle beams in high-energy accelerators”. In: *Reports on Progress in Physics* 68.9 (2005), p. 1997. URL: http://stacks.iop.org/0034-4885/68/i=9/a=R01.

[22] W. Haeberli. “Sources of Polarized Ions”. In: *Annual Review of Nuclear and Particle Science* 17 (1967), pp. 373–426. DOI: 10.1146/annurev.ns.17.120167.002105.

[23] Gerald G. Ohlsen and P.W. Keaton. “Techniques for measurement of spin-12 and spin-1 polarization analyzing tensors”. In: *Nuclear Instruments and Methods* 109.1 (1973), pp. 41 –59. ISSN: 0029-554X. DOI: http://dx.doi.org/10.1016/0029-554X(73)90450-3. URL: http://www.sciencedirect.com/science/article/pii/0029554X73904503.

[24] N. P. M. Brantjes et al. “Correcting systematic errors in high-sensitivity deuteron polarization measurements”. In: *Nucl. Instrum. Meth.* A664 (2012), pp. 49–64. DOI: 10.1016/j.nima.2011.09.055.

[25] F. Seiler et al. “Extreme values of the spin polarization analyzing power in nuclear reactions”. In: *Nuclear Physics A* 296 (Feb. 1978), pp. 205–227. DOI: 10.1016/0375-9474(78)90069-6.

[26] Syohei Kato et al. “Analyzing power measurements for d-12C elastic scattering between 35–70 MeV”. In: *Nuclear Instruments and Methods in Physics Research Section A: Accelerators, Spectrometers, Detectors and Associated Equipment* 238.2 (1985), pp. 453 –462. ISSN: 0168-9002. DOI: http://dx.doi.org/10.1016/0168-9002(85)90484-X. URL: http://www.sciencedirect.com/science/article/pii/016890028590484X.

[27] D. Chiladze et al. “Determination of deuteron beam polarizations at COSY”. In: *Physical Review Special Topics - Accelerators and Beams* 9 (2006), p. 050101. DOI: 10.1103/PhysRevSTAB.9.050101. URL: http://hal.in2p3.fr/in2p3-00025163.

[28] Edward Stephenson. personal communication. Indiana University Center for Spacetime Symmetries, 2017.

[29] W. Glöckle et al. “The three-nucleon continuum: achievements, challenges and applications”. In: *Physics Reports* 274.3 (1996), pp. 107 –285. ISSN: 0370-1573. DOI: http://dx.doi.org/10.1016/0370-1573(95)00085-2. URL: http://www.sciencedirect.com/science/article/pii/0370157395000852.

[30] V. Bargmann, Louis Michel, and V. L. Telegdi. “Precession of the Polarization of Particles Moving in a Homogeneous Electromagnetic Field”. In: *Phys. Rev. Lett.* 2 (10 1959), pp. 435–436. DOI: 10.1103/PhysRevLett.2.435. URL: https://link.aps.org/doi/10.1103/PhysRevLett.2.435.

[31] James P Miller, Eduardo de Rafael, and B Lee Roberts. “Muon (g - 2): experiment and theory”. In: *Reports on Progress in Physics* 70.5 (2007), p. 795. URL: http://stacks.iop.org/0034-4885/70/i=5/a=R03.

[32] G. W. Bennett et al. “Improved limit on the muon electric dipole moment”. In: *Phys. Rev. D* 80 (5 2009), p. 052008. DOI: 10.1103/PhysRevD.80.052008. URL: https://link.aps.org/doi/10.1103/PhysRevD.80.052008.

[33] V. Anastassopoulos et al. “A storage ring experiment to detect a proton electric dipole moment”. In: *Review of Scientific Instruments* 87.11 (2016), p. 115116. DOI: 10.1063/1.4967465. eprint: http://aip.scitation.org/doi/pdf/10.1063/1.4967465. URL: http://aip.scitation.org/doi/abs/10.1063/1.4967465.

[34] Andreas Lehrach et al. “Precursor Experiments to Search for Permanent Electric Dipole Moments (EDMs) of Protons and Deuterons at COSY”. In: (2012). arXiv: 1201.5773 [hep-ex].

[35] William M. Morse, Yuri F. Orlov, and Yannis K. Semertzidis. “rf Wien filter in an electric dipole moment storage ring: The “partially frozen spin” effect”. In: *Phys. Rev. ST Accel. Beams* 16 (11 2013), p. 114001. DOI: 10.1103/PhysRevSTAB.16.114001. URL: https://link.aps.org/doi/10.1103/PhysRevSTAB.16.114001.

[36] R. Maier. “Cooler synchrotron COSY—Performance and perspectives”. In: *Nuclear Instruments and Methods in Physics Research Section A: Accelerators, Spectrometers, Detectors and Associated Equipment* 390.1-2 (1997), pp. 1–8.

[37] D. Prasuhn et al. “Electron and stochastic cooling at {COSY}”. In: *Nuclear Instruments and Methods in Physics Research Section A: Accelerators, Spectrometers, Detectors and Associated Equipment* 441.1 (2000), pp. 167 –174. ISSN: 0168-9002. DOI: https://doi.org/10.1016/S0168-9002(99)01128-6. URL: http://www.sciencedirect.com/science/article/pii/S0168900299011286.

[38] H. H. Adam et al. “Proposal for the wide angle shower apparatus (WASA) at COSY-Julich: WASA at COSY”. In: (2004). arXiv: nucl-ex/0411038 [nucl-ex].

[39] M. Eggert. “Entwicklung eines gepulsten Casium-Ionenstrahls fur die Quelle polarisierter Ionen an COSY/Jülich”. PhD thesis. Universtät zu Köln, 1998.

[40] R. Reckenfelderbäumer. “Entwicklung des Cäsiumstrahlteils einer Quelle polarisierter Ionen nach dem Colliding-Beams-Prinzip”. PhD thesis. Universtät zu Köln, 1995.

[41] Z. Bagdasarian et al. “Measuring the polarization of a rapidly precessing deuteron beam”. In: *Phys. Rev. ST Accel. Beams* 17 (5 2014), p. 052803. DOI: 10.1103/PhysRevSTAB.17.052803. URL: https://link.aps.org/doi/10.1103/PhysRevSTAB.17.052803.

[42] “A precision measurement of pp elastic scattering cross-sections at intermediate energies”. In: *The European Physical Journal A - Hadrons and Nuclei* 22.1 (2004), pp. 125–148. ISSN: 1434-601X. DOI: 10.1140/epja/i2004-10011-3. URL: http://dx.doi.org/10.1140/epja/i2004-10011-3.

[43] G. Guidoboni et al. “How to Reach a Thousand-Second in-Plane Polarization Lifetime with $0.97-\mathrm{GeV}/c$ Deuterons in a Storage Ring”. In: *Phys. Rev. Lett.* 117 (5 2016), p. 054801. DOI: 10.1103/PhysRevLett.117.054801. URL: https://link.aps.org/doi/10.1103/PhysRevLett.117.054801.

[44] V Anastassopoulos et al. *A Proposal to Measure the Proton Electric Dipole Moment with $10^{-29}\,e\,cm$ Sensitivity.* 2011. URL: https://www.bnl.gov/edm/Proposal.asp.

[45] Yoshihiko Shoji. “Dependence of average path length betatron motion in a storage ring”. In: *Phys. Rev. ST Accel. Beams* 8 (9 2005), p. 094001. DOI: 10.1103/PhysRevSTAB.8.094001. URL: https://link.aps.org/doi/10.1103/PhysRevSTAB.8.094001.

[46] D. Eversmann et al. “New method for a continuous determination of the spin tune in storage rings and implications for precision experiments”. In: *Phys. Rev. Lett.* 115.9 (2015), p. 094801. DOI: 10.1103/PhysRevLett.115.094801. arXiv: 1504.00635 [physics.acc-ph].

[47] D. Eversmann. “High Precision Spin Tune Determination at the Cooler Synchrotron in Jülich”. PhD thesis. RWTH Aachen Univerits, 2017, To be published.

[48] N. Hempelmann. “FPGA-Based Upgrade of the Read-Out Electronics for the Low Energy Polarimeter at COSY/Jülich”. In: *Proceedings of the XVIth International Workshop in Polarized Sources, Targets, and Polarimetry (PSTP2015). 14-18 September 2015. Ruhr-University Bochum, Germany. Online at http://pos. sissa. it/cgi-bin/reader/conf. cgi? confid= 243, id. 25.* 2015.

[49] Stefan Bartknecht et al. “Development and performance verification of the GANDALF high-resolution transient recorder system”. In: *IEEE Transactions on Nuclear Science* 58.4 (2011), pp. 1456–1459.

[50] Philipp Jörg. “Untersuchung von Algorithmen zur Charakterisierung von Photomultiplierpulsen in Echtzeit”. MA thesis. Albert-Ludwigs-Universität Freiburg, 2013.

[51] G. van Rossum and F.L. Drake. *Python Reference Manual.* URL: http://www.python.org.

[52] Rene Brun and Fons Rademakers. “ROOT - An Object Oriented Data Analysis Framework”. In: *Proceedings AIHENP’96 Workshop, Lausanne, Nucl. Inst. & Meth. in Phys. Res. A 389 (1997) 81-86. See also http://root.cern.ch/.* 1996.

[53] Rene Brun, Fons Rademakers, et al. *ROOT User’s Guide.* https://root.cern.ch/guides/users-guide.

[54] Kyle S. Cranmer. “Kernel estimation in high-energy physics”. In: *Comput. Phys. Commun.* 136 (2001), pp. 198–207. DOI: 10.1016/S0010-4655(00)00243-5. arXiv: hep-ex/0011057 [hep-ex].

[55] Emanuel Parzen. “On Estimation of a Probability Density Function and Mode”. In: *Ann. Math. Statist.* 33.3 (Sept. 1962), pp. 1065–1076. DOI: 10.1214/aoms/1177704472. URL: http://dx.doi.org/10.1214/aoms/1177704472.

[56] N. Hempelmann et al. “Phase Locking the Spin Precession in a Storage Ring”. In: *Phys. Rev. Lett.* 119 (1 2017), p. 014801. DOI: 10.1103/PhysRevLett.119.014801. URL: https://link.aps.org/doi/10.1103/PhysRevLett.119.014801.

[57] J. Slim et al. “Electromagnetic Simulation and Design of a Novel Waveguide {RF} Wien Filter for Electric Dipole Moment Measurements of Protons and Deuterons”. In: *Nuclear Instruments and Methods in Physics Research Section A: Accelerators, Spectrometers, Detectors and Associated Equipment* 828 (2016), pp. 116 –124. ISSN: 0168-9002. DOI: https://doi.org/10.1016/j.nima.2016.05.012. URL: http://www.sciencedirect.com/science/article/pii/S0168900216303710.

[58] P. Benati et al. “Synchrotron oscillation effects on an rf-solenoid spin resonance”. In: *Physical review / Special topics / Accelerators and beams* 15.12 (2012), p. 124202. ISSN: 1098-4402. DOI: 10.1103/PhysRevSTAB.15.124202. URL: http://juser.fz-juelich.de/record/132053.

[59] A. Saleev et al. “Spin tune mapping as a novel tool to probe the spin dynamics in storage rings”. In: (2017). arXiv: 1703.01295 [physics.acc-ph].

[60] Helmut Soltner. Personal Communication. Institut für Kernphysik, Forschungszentrum Jülich, 2017.

[61] S. Mey and R. Gebel. “Spin Manipulation with an RF Wien-Filter at COSY”. In: *Proceedings of the XVIth International Workshop in Polarized Sources, Targets, and Polarimetry (PSTP2015). 14-18 September 2015. Ruhr-University Bochum, Germany. Online at http://pos. sissa. it/cgi-bin/reader/conf. cgi? confid= 243, id. 29.* 2015.

List of Figures

Acknowledgements

I would like to thank my supervisors, Prof. Dr. Jörg Pretz and Dr. Ralf Gebel for their advice and the opportunity to write my thesis at Forschungszentrum Jülich and RWTH Aachen.

Additionally, I thank my colleagues from the JEDI collaboration for the stimulating working environment and interesting discussions. For the help with the polarimetry part of my thesis, I especially thank Dr. Irakli Keshelashvili and Dr. Edward Stephenson. For the analysis part, I thank Dr. Volker Hejny and Dr. Helmut Soltner.

A special thanks goes to the hardware group in Freiburg, especially Prof. Dr. Horst Fischer, Dr. Philipp Jörg and Paul Kremser, for the instructive two-week stay at their institute and the support in all my FPGA problems.

Finally, I would like to thank my fellow PhD candidates for their valuable input and fun company: Dr. Stanislav Chekmenev, Dennis Eversmann, Jan Hetzel, Fabian Hinder, Paul Maanen, Sebastian Mey, Fabian Müller, Dr. Marcel Rosenthal, Vera Schmidt and Fabian Trinkel.